Title
A Near-Infrared Look at Bulgeless and Dwarf Galaxies: An Investigation of Obscured AGN and Their Outflows

Author
Bohn, Thomas

Publication Date
2022

UNIVERSITY OF CALIFORNIA
RIVERSIDE

A Near-Infrared Look at Bulgeless and Dwarf Galaxies: An Investigation of Obscured AGN and Their Outflows

A Dissertation submitted in partial satisfaction
of the requirements for the degree of

Doctor of Philosophy

in

Physics

by

Thomas Bohn

March 2022

Dissertation Committee:

Professor Gabriela Canalizo, Chairperson
Professor Laura Sales
Professor Frederick Hamann

The Dissertation of Thomas Bohn is approved:

Committee Chairperson

University of California, Riverside

Acknowledgments

First, to my family, who have always been there for me and have supported me from the beginning. To Dad, who has has consistently given me stability and kept me on course. To Okasaan, whom I could always come to for guidance or share my problems with. To my brother, who made me the person I am today. And to the rest of my family, who have encouraged throughout my journey. Arigatoo gozaimasu!

To my friends, both those who shared my journey through graduate school and those outside the department. I couldn't have made this journey without you. Thank you.

I also thank Dr. Percy Gomez, Dr. Sherry Yeh, Dr. Gregg Doppmann, and Dr. Josh Walawender for supporting our Keck observations.

And lastly, to my advisor Gabriela Canalizo, for her patience, guidance, and never-ending support. I have reached this point because of her and I am extremely fortunate to have her as my mentor.

I acknowledge financial support from the National Science Foundation, under grant No. AST 1817233. I also acknowledge Dr. Randy Campbell and the support provided by the Keck Visiting Scholars Program.

The text of this dissertation, in part, is a reprint of the published articles titled "The Discovery of a Hidden Broad-line AGN in a Bulgeless Galaxy: Keck NIR Spectroscopic Observations of SDSS J085153.64+392611.76" and "Near-Infrared Coronal Line Observations of Dwarf Galaxies hosting AGN-driven Outflows" as they appear in *The Astrophysical Journal*, Volume 899, Number 1, 14 August 2020 and Volume 911, Number 1, 16 April 2021,

respectively. The co-authors, Gabriela Canalizo, Shobita Satyapal, Sylvain Veilleux, Ryan W. Pfeifle, and Weizhe Liu, supervised or provided comments to assist in the publication of the article as it appears in this dissertation.

ABSTRACT OF THE DISSERTATION

A Near-Infrared Look at Bulgeless and Dwarf Galaxies: An Investigation of Obscured AGN and Their Outflows

by

Thomas Bohn

Doctor of Philosophy, Graduate Program in Physics
University of California, Riverside, March 2022
Professor Gabriela Canalizo, Chairperson

It is now widely accepted that supermassive black holes (SMBHs) lie at the center of most massive galaxies. While SMBHs in these hosts have been well documented and studied, those in lower mass hosts, such as dwarf and spiral galaxies without a central bulge component (i.e. bulgeless galaxies), have remained quite elusive and insufficiently studied. Identifying and examining exactly how active galactic nuclei (AGN) co-evolve and influence bulgeless and dwarf host galaxies is the foundation of my dissertation research. These galaxies can be used as local analogs of the infant Universe (gas rich, low metallicity, rapidly growing) and their BH number density and occupation fraction can provide important constraints on the BH seed population. However, these AGN are difficult to study since they are energetically weak or heavily obscured. The IR provides a unique and compelling avenue to study these AGN since it is not as severely affected by dust obscuration as optical observations. As such, my research utilizes IR selection techniques and observations to identify a new population of obscured AGN that have been overlooked by large optical surveys. Much of my work has focused on coronal lines (CLs), outflows, and analyzing the impacts

of AGN on their hosts. In my publications, we confirm AGN activity in a sample of dwarf and bulgeless galaxies through the presence of CL and hidden broad-line emission. In many of these, we find fast, kpc outflows that are likely driven by the AGN. We also find that the outflowing gas have sufficient escape velocities to allow the gas to escape their host dark matter halo. As a result, these outflows have the potential to suppress star formation and could play a key role in dwarf and bulgeless galaxy evolution. Additionally, these observations can help deliver key constraints to improve the theoretical feedback models of dwarf and bulgeless galaxies.

Contents

List of Figures

List of Tables

Chapter 1

Introduction

The relations between galaxies and their central supermassive BHs have become a vital part of understanding galaxy evolution. Strong correlations between BH and galactic bulge mass indicate the two grow through mergers and episodes of violent disk instability (eg., McConnell & Ma, 2013; Sexton et al., 2019). Some galaxies, however, remain disk dominated and their BHs have grown through processes largely independent of major interactions. Studying these galaxies, which are predominately bulgeless and dwarf galaxies, can provide important clues to alternative and secular BH growth mechanisms. Additionally, dwarf galaxies can be used as local analogs of the infant Universe (gas rich, low metallicity, rapidly growing) and their BH number density and occupation fraction can provide important constraints on the BH seed population.

While significant effort has been made to analyze the link between AGN and their hosts in the large mass regime, our understanding of the impacts of AGN in the lower mass galaxies is more uncertain. Only recently have studies revealed signatures of AGN activity in bulgeless and dwarf galaxies on a large statistical basis (Reines et al., 2013; Satyapal et al., 2014). While BH mass estimates are starting to emerge in these systems (Simmons et al., 2017; Bohn et al., 2020), the impact of these BHs on the evolution of their hosts is still not well understood.

An important aspect of BH-galaxy co-evolution is BH feedback on its host. In the large mass regime, AGN feedback has been recognized as critical in suppressing cooling flows, thereby modifying their hosts luminosities, colors, and stellar masses. The general consensus regarding feedback in dwarf galaxies is that stellar processes, such as starbursts and supernovae (SNe), provide the main source of quenching. However, evidence of AGN-driven feedback in dwarf galaxies is already starting to emerge. Isolated, gas-depleted dwarfs with AGN line ratios have been reported while others show kinematically disturbed gas near central regions (Penny et al., 2018; Bradford et al., 2018). More recently, fast kiloparsec outflows that have sufficient energy to expel gas into the circumgalacitc medium have been observed in dwarf galaxies hosting AGN (Manzano-King et al., 2019; Liu et al., 2020). As such, these discoveries necessitate the re-evaluation of the role of AGN feedback in dwarf galaxy evolution.

Studying BHs in bulgeless and dwarf galaxies can therefore serve a dual purpose. First, identifying and measuring BH masses in these galaxies will aid us in constraining the seed population and secular growth mechanism. Secondly, by studying BHs that are actively accreting, we can better quantify the impact of AGN feedback in the low mass regime. Furthermore, this research of BH-galaxy co-evolution and feedback processes directly addresses key scientific objectives presented in the 2020 Decadal Survey.

Examining exactly how AGN co-evolve and influence bulgeless and dwarf galaxies is the foundation of my dissertation research. However, these AGN are difficult to study since they are energetically weak or heavily obscured. Indeed, my sample is predominately Type 2, which limits the utility of optical observations in obtaining important measurements such as BH mass. The infrared provides a unique avenue to study these AGN since it is not as severely affected by dust obscuration. As such, my research utilizes IR selection techniques and observations to identify a new population of obscured AGN that have been overlooked by large optical surveys.

The various calculations presented this paper requires careful reduction of the data in order to allow precise measurements of emission lines and other spectral features. To this end, I have developed a specialized data processing algorithm, suitable for any NIR spectroscopic data, that fully reduces spectroscopic data. The algorithm uses techniques described in Kelson (2003) and Becker et al. (2009) to provide robust background subtraction. It also provides flexibility in aperture selection to allow extraction for spatially extended sources.

This Dissertation paper is split into 3 main chapters. Chapters 2 and 4 examine a sample of of bulgeless galaxies, where Chapter 2 examines a unique and compelling bulgeless galaxy while Chapter 4 discusses the full bulgeless sample. Chapter 3 analyzes a sample of dwarf galaxies with evidence of fast, kpc outflows driven by the AGN.

Much of my work has focused on the emission lines found in the near-infrared (NIR) to identify the presence of AGN activity. Of particular note are coronal lines (CLs), which are highly ionized forbidden transitions and are a robust indicator of AGN activity. In Chapters 2 and 4, I will use CLs to confirm the presence of AGN in a sample of bulgeless galaxies. A similar investigation was done for a sample of dwarf galaxies, as presented in Chapter 3. A notable trait of CLs is that they are often blueshifted relative to the systemic velocity of their host (Rodríguez-Ardila et al., 2006; Müller-Sánchez et al., 2011). As such, they are often associated with outflows and provide a unique look into AGN feedback in these systems. In Chapters 3 and 4, we confirm outflows in both dwarf and bulgeless galaxies and find a strong correlation between outflows and CLs.

Lastly, another key goal of my research has been to obtain BH mass measurements. BH masses of bulgeless and dwarf galaxies can help us identify the correct BH seeding models (Greene et al., 2020). Virial mass estimates using gas emission from the broad-line region is a robust method but its usefulness is limited for Sy2 galaxies. However, due to its insensitivity to dust obscuration, the NIR allows an alternative way of observing the 'hidden' broad-line gas of Type 2 targets. In Chapter 4, we report two hidden broad-lines in our bulgeless sample. These BH masses are some of the highest seen for bulgeless galaxies, and it is certainly intriguing how these BHs grew to supermassive sizes through secular processes.

Chapter 2

The Discovery of a Hidden Broad-line AGN in a Bulgeless Galaxy: Keck NIR Spectroscopic Observations of SDSS J085153.64+392611.76

2.1 Introduction

The advent of the discovery that supermassive black holes (SMBHs) lie at the center of virtually all massive galaxies has promoted the idea that these black holes (BHs) play a fundamental role in galaxy formation and evolution (for a review, see Kormendy & Ho, 2013). Well-known relations such as BH mass ($M_{\rm BH}$) correlating with stellar velocity dispersion, $M_{\rm BH}$–σ, (eg., Ferrarese & Merritt, 2000; Gebhardt et al., 2000; McConnell & Ma, 2013), and stellar bulge mass, $M_{\rm BH}$–$M_{\rm bulge}$, (eg., Marconi & Hunt, 2003; Häring & Rix, 2004), provide a picture that BH growth accompanies central bulge growth. An often-suggested scenario of this interaction involves major mergers that not only fuel BH growth but can also trigger the buildup of the bulge component (eg., Kauffmann et al., 2003; Di Matteo et al., 2005; Ellison et al., 2011). Subsequent feedback from the accreting BH (active galactic nucleus [AGN]) can help quench star formation by either expelling gas out of the galaxy (eg., Kauffmann & Haehnelt, 2000) or by heating the gas in the halo and preventing it from feeding the disk (eg., Bower et al., 2006; Croton et al., 2006). As a result, the galaxy evolves toward the well-defined red sequence. Therefore, galaxy growth has long been thought to be hierarchical, with major mergers providing the necessary conditions for BHs and their host galaxies to reach their observed masses (eg., Sanders et al., 1988; Kauffmann et al., 1993). In addition to major mergers affecting BH growth, stochastic fueling from dense gas clouds reaching the nucleus can also trigger AGN at the low/mid-luminosity regime (Hopkins et al., 2014).

This scenario of BH growth accompanying bulge development through mergers highlights the importance of studying the secular evolution of BHs in galaxies that have had a quiescent merger history. Unlike bulge-dominated galaxies whose BHs have had accelerated accretion, BHs in likely merger-free galaxies (such as bulgeless galaxies) have grown largely independent of major interactions. Therefore, the mass distribution and occupation fraction of these BHs can provide important clues to the original seed population and secular triggering mechanisms. Additionally, current BH scaling relations lack significant contributions from bulgeless galaxies that can misrepresent the AGN population as a whole.

Studying these quiescently grown BHs is thus critical to our understanding of BH growth and their contribution to their host galaxy evolution.

Discoveries of disk-dominated (low bulge-to-total light ratio, B/T) and bulgeless galaxies hosting low- to intermediate-luminosity AGN have been limited, but recent estimates of their BH masses (eg., Filippenko & Ho, 2003; Satyapal et al., 2007; McAlpine et al., 2011; Secrest et al., 2012; Reines et al., 2013; Simmons et al., 2013, 2017) indicate that they can be up to 10^8 $M_\odot$. These findings are starting to show that a central bulge is not a requirement to have a SMBH and that $M_{\rm BH}$ in disk-dominated galaxies are likely correlated to the total stellar mass of the galaxy ($M_{\rm stellar}$) rather than to the mass of the bulge, $M_{\rm bulge}$ (Simmons et al., 2017; Martin et al., 2018). In addition, coevolution of BHs and galaxies through merger-free processes, such as disk instabilities and secular growth, has been previously suggested (eg., Kormendy & Kennicutt, 2004; Greene et al., 2010; Schawinski et al., 2011b), and these processes may be able to grow the central BHs to their typical observed masses (Simmons et al., 2013; Martin et al., 2018). This suggests that AGN feedback or perhaps some broader, galaxy-wide process regulates the amount of matter that the BH is allowed to accrete.

However, the number of *purely* bulgeless galaxies with $M_{\rm BH}$ estimates in the literature represents a very small fraction of the total bulgeless population, and it is very likely that optical catalogs misidentify or exclude deeply buried AGN in dusty, late-type galaxies. Additional problems arise in verifying the true morphology of the central region, and it is often difficult to rule out the presence of small bulges. This is particularly problematic for Seyfert 1 (Sy1) galaxies, where the bright AGN is in our direct line of sight, compromising the reliability of bulge–disk decompositions employed to measure the total bulge component. While the visible broad-line region (BLR) in these galaxies allows us to obtain estimates of $M_{\rm BH}$ through the virial method, the light from the AGN can preclude us from detecting a small bulge component. Sy2 galaxies, on the other hand, allow for much more stringent constraints on the presence of bulges, since their AGN is hidden from our line of sight. However, for the same reason, $M_{\rm BH}$ estimates are more difficult to come by. Several methods have been used in an attempt to detect the 'hidden' BLR in Sy2 galaxies, including spectropolarimetry (Antonucci & Miller, 1985) and high S/N near-infrared (NIR) observations where extinction is less severe (Veilleux et al., 1997; Lamperti et al., 2017). These studies have revealed that only 10-20% of Sy2 galaxies show a BLR in the NIR, likely due to strong obscuration.

In this article, we present the discovery of a hidden, NIR BLR found in J085153.64+392611.76, hereafter J0851+3926, a spiral galaxy at redshift 0.1296 that shows no signs of a bulge component and is part of a larger study of bulgeless galaxies (see Chapter 4, Fig. 2.1). J0851+3926 is listed as 'starforming' under the *Subclass* keyword by the Sloan Digital Sky Survey (SDSS), and the SDSS spectrum, although showing composite narrow-line ratios, does not show clear broad Balmer lines. Since there is no AGN contribution at the center, we can put strong constraints on the presence of a bulge using optical photometry. This allows for the rare chance of obtaining a robust BH mass estimate from the NIR broad line while also putting strong constraints on any possible bulge component. In Section 2.2, we describe the construction of our sample, observations, and reduction procedure. Section 2.3 presents the results of surface brightness decompositions, the BH mass, intrinsic extinction, and observed gas dynamics. Section 2.4 compares J0851+3926 to other bulgeless galaxies and $M_{\rm BH}$–galaxy relations. Additionally, we discuss possible triggering mechanisms of the AGN. We adopt a standard ΛCDM cosmology with $H_0 = 70$ km s^{-1} Mpc^{-1}, $\Omega_M = 0.3$, and $\Omega_\Lambda = 0.7$.

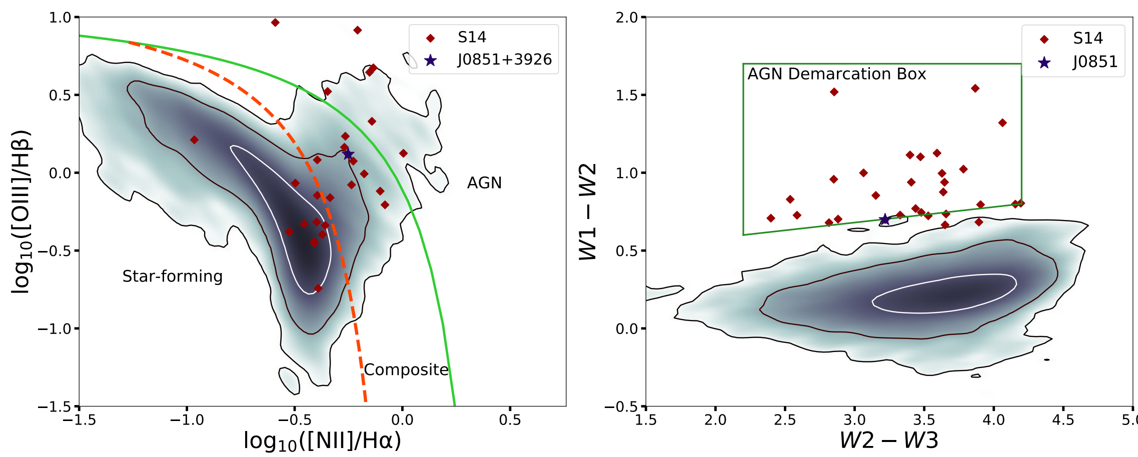

Figure 2.1: BPT (left) and WISE color (right) plots of the bulgeless sample. Red diamonds and the blue star represent the sample selected by S14 and J0851+3926, respectively. The inclusion contours are drawn at σ intervals (68%, 95%, and 99.5%). The lines separating the AGN (Kewley et al., 2001) and composite (Kauffmann et al., 2003) regions from the starforming in the BPT diagram are shown as solid and dashed lines, respectively. The AGN demarcation region is shown as defined in Jarrett et al. (2011). Note that J0851+3926 falls in the composite region and is on the border of the AGN demarcation box.

2.2 Data and Observations

2.2.1 Data Selection

Since large optical surveys can miss deeply buried AGN, our selection process focuses on infrared (IR) selection techniques. Satyapal et al. (2014), hereafter S14, selected galaxies believed to host obscured AGN using mid-infrared colors and the AGN selection criteria presented in Jarrett et al. (2011). S14 suggested that IR indicators could be used to identify optically obscured AGN based on their strong IR colors that separate them from stellar processes. Motivated by these findings, our selection process followed closely to that of S14. To summarize, we formed an initial sample of bulgeless galaxies by drawing from Simard et al. (2011), who performed bulge-disk decompositions using GIM2D (Simard et al., 2002) of 1.12 million galaxies from SDSS DR7. The surface brightness, point-spread function (PSF) convolved bulge–disk decompositions were done in both SDSS r and g bands. Three different galaxy fitting models were utilized: a bulge ($n_b = 4$) + disk model, a free-floating Sérsic index "bulge" ($n_b =$ free) + disk model, and a pure Sérsic model. We used the model with a free-floating bulge index in order to select galaxies with a B/T equal to 0.00. Of the 632,952 galaxies within a redshift of $z < 0.2$, only 19,136 have B/T = 0.00 in both r and g bands. Using fluxes taken from the Portsmouth spectroscopic reanalysis *emissionLinesPort* table (Thomas et al., 2013) in SDSS, we constructed a Baldwin, Phillips, & Terlevich (BPT) diagram (Baldwin et al., 1981) using [O III]λ5007/Hβ and [N II]λ6585/Hα line ratios (see Figure 2.1, left panel). The Portsmouth analysis accounted for stellar absorption features by using the Gas AND Absorption Line Fitting (GANDALF[1]; Sarzi et al. (2006)) and the penalized Pixel Fitting (pPXF[2]; Cappellari & Emsellem, 2004) routines. By fitting for the stellar absorption features, the fluxes of the hydrogen lines, specifically Hα and Hβ, increase, causing galaxies to generally shift toward the lower left (i.e., the starforming region) of the BPT diagram. We excluded the 648 galaxies with no registered Portsmouth fluxes, which left only 18,488 bulgeless galaxies in our sample. Following the AGN classification scheme presented in Kewley et al. (2001), only 143 (0.77%) galaxies are identified as AGN. However,

[1] https://gandalfcode.github.io
[2] https://www-astro.physics.ox.ac.uk/~mxc/software/

many spectra can contain contributions from both the AGN and star-forming H II regions. As a result, galaxies hosting relatively weak AGN can fall below this line. Kauffmann et al. (2003) defined a composite region between the AGN and star-forming portions of the diagram, where 950 (5.14%) galaxies of our sample fall. Galaxies in the composite region are generally believed to have a mixture of AGN and star-forming emission. However, merger-driven shocks can reproduce AGN-H II emission-line ratios (Rich et al., 2014), so galaxies that fall in this region cannot be definitively classified as AGN without other lines of evidence.

AGN at low redshift should be considerably redder than inactive galaxies (Stern et al., 2012; Assef et al., 2013). Utilizing the Wide-field Infrared Survey Explorer (WISE) All-Sky Data Release (Wright et al., 2010), we obtained WISE band magnitudes $W1$(3.4 μm), $W2$(4.6 μm), and $W3$(12 μm) matched within $1''$ for our SDSS bulgeless sample. Of the 18,488 SDSS bulgeless galaxies, 18,146 (98.15%) have registered WISE magnitudes in the required bands. In Figure 2.1 (right panel), we employed the WISE color diagnostic presented in Jarrett et al. (2011). Here, they define a demarcation zone separating AGNs using $W1$ - $W2$ and $W2$ - $W3$ color cuts. Only 27 members (0.15%) of our sample fall in the AGN demarcation zone. Using the aforementioned three-band color cut, S14 selected 30 AGN candidates with $W1$ - $W2 > 0.7$ that are most likely to host dominant AGN. These 30 galaxies form our base sample, and one of them, J0851+3926, is the focus of this paper. The full sample will be investigated in a follow-up paper.

2.2.2 NIR Observations and Reductions

NIR spectroscopy of J0851+3926 was obtained on two separate dates: on 2018 March 5 using Keck II NIRSPEC (McLean et al., 1998), and on 2019 March 25 with Keck II NIRES (Wilson et al., 2004). NIRSPEC is a NIR echelle spectrograph with a wavelength coverage from 0.9 to 5.5 μm. The NIRSPEC-7 filter was used in low-resolution mode with a cross-dispersion angle of 35.38°. This resulted in a wavelength coverage of ~1.8 — 2.4 μm. The $42'' \times 0.76''$ slit was used, and a spectral resolution of ~120 km s^{-1} at the observed wavelength of Paα was measured with a seeing of ~$0.75''$. Observations throughout the night were done under variable and heavy cloud cover. While telluric and flux standards were observed before and after the science object, the amount of extinction was highly variable, and thus the flux calibration for these data is uncertain. Note that these observations were done before the NIRSPEC upgrade. NIRES is a NIR echelette spectrograph and it has a fixed configuration. The single slit is $18'' \times 0.55''$ and the wavelength coverage is set from 0.94 to 2.45 μm across five orders. There is a small gap in coverage between 1.85 and 1.88 μm, but this is a region of low atmospheric transmission. The spectral resolution at Paα was ~85 km s^{-1} and the seeing was typically ~$0.5''$ throughout the night. Observations were done under mostly clear conditions, and so the majority of the analysis was done with the NIRES data. Individual exposures for both sets of observations were 4 minutes each and were done using the standard ABBA nodding. An A0 telluric standard star (with measured magnitudes in K, H, and J bands) was observed either directly before or after the target galaxy to correct for the atmospheric absorption features. The total exposure times for NIRSPEC and NIRES were 32 and 20 minutes, respectively. A summary of the NIR observations is shown in Table 2.1.

Table 2.1: Observation Log for J0853926

Instrument	Date (YYYY-mm-dd)	Seeing (arcsec)	Exp. Time (s)	PA (deg)	Extraction Aperture (arcsec)	Air Mass	Telluric
NIRSPEC	2018 March 5	~ 0.75	1920^a	46	1.34	1.06	HD 63610
NIRES	2019 Mar 25	~ 0.5	1200^b	94	1.33	1.07	HD 63610

[a] 8×240 s exposures (two ABBA sets) were taken, [b] 5×240 s exposures were taken

The data were reduced using two modified pipelines. The first provided flat-fielding and a robust background subtraction by using techniques described in Kelson (2003) and Becker et al. (2009). In short, this routine maps the 2D science frame and models the sky background before rectification, thus reducing the possibility of artifacts appearing due to the binning of sharp features. The sky subtraction attained with this procedure is excellent, despite the strong OH lines present in the NIR; the procedure is also quite insensitive to cosmic rays and hot pixels and is reliable regardless of skyline intensity.

Rectification, telluric correction, wavelength calibration, and extraction were all done with a slightly modified version of REDSPEC.[3] The sizes of the extracted aperture are listed in Table 2.1. The 1D spectrum were then median combined. Flux calibration was done using the telluric star and the Spitzer Science Center unit converter[4] to convert the magnitude of the star to the associated flux in that band. A small corrective factor ($< 5\%$) was introduced owing to the differences between the center of NIR bands and that of the wavelength coverage.

[3] https://www2.keck.hawaii.edu/inst/nirspec/redspec.html

[4] http://ssc.spitzer.caltech.edu/warmmission/propkit/pet/magtojy/

2.2.3 X-Ray Observations and Reductions

J0851+3926 was observed for 19.8 ks with the ACIS-S instrument on board the *Chandra* X-ray Observatory on 2020 January 19, with the target centered at the aim point of the ACIS-S3 chip. The data were reduced and analyzed using the Chandra Interactive Analysis of Observations (CIAO) software package (Fruscione et al., 2006) version 4.11 along with version 4.8.2 of the Calibration Database (CALDB). A circular aperture of 1.5″ in radius was centered on the coordinates of the galaxy nucleus, from which source counts were extracted. The background counts were extracted using a circular aperture of radius 25″ and was placed in a nearby area free of other sources. Full (0.3 – 8 keV), soft (0.3 – 2 keV), and hard (2 – 8 keV) counts were extracted from energy-filtered event files using the DMEXTRACT package in CIAO and error bounds were calculated using Gehrels statistics (Gehrels, 1986).

2.3 Analysis

2.3.1 GALFIT Fitting

J0851+3926 is a Sy2 galaxy with no visible AGN to saturate or blend with a possible bulge. In order to place stringent constraints on the presence of a small bulge, we performed two-dimensional decompositions using GALFIT[5] (Peng et al., 2002, 2010) and ran fits using various combinations of PSF and Sérsic profiles. The PSF was constructed from the *psField* file provided by SDSS and had a full-width half-maximum (FWHM) of 0.717″ (1.65 kpc at the redshift of J0851+3926). Due to the lack of a resolved core component,

[5] https://users.obs.carnegiescience.edu/peng/work/galfit/galfit.html

GALFIT could never converge on a reasonable solution when a PSF or two Sérsic profiles were used. As expected for a bulgeless galaxy, GALFIT could only properly converge on a solution containing a single Sérsic profile. As a check, we used various initial index values reflecting a de Vaucouleur bulge ($n = 4$), a pseudobulge ($n \sim 2$), and an exponential disk ($n = 1$). Regardless of the initial values used, GALFIT consistently converged on an index of $n = 0.55$.

The fit to the data is presented in Figure 2.2a, where the best-fit model includes a small background component. The best-fit model matches the data reasonably well out to about $8''$, where the galaxy ends and the background noise starts to dominate. However, there are some small oscillations in the residuals that are due to spiral arms in the disk of the galaxy, as seen in the 2D residual image. These spiral arms could alter the results of the fitting, particularly in the central region. To factor these out, we tried fitting them using a combination of a power function and Fourier modes, but the resolution and surface brightness of the arms were too low for GALFIT to converge on any solution. We subsequently created a mask using the residuals from the fit and left the central region unmasked. Fitting the galaxy with the mask greatly reduced the residuals at the center and gave a Sérsic index of $n = 0.89$ (see Figure 2.2b). The central unmasked region within roughly $1.5''$ is almost perfectly described as a disk with no bulge component.

Although the fits in Figure 2.2 match the data quite well, the possibility of an unresolved bulge or pseudobulge component cannot be dismissed. We obtained an upper limit to the bulge mass by estimating the magnitude of a PSF (i.e., an unresolved component) that can account for the residuals closest to the core in Figure 2.2a (i.e., the fit without

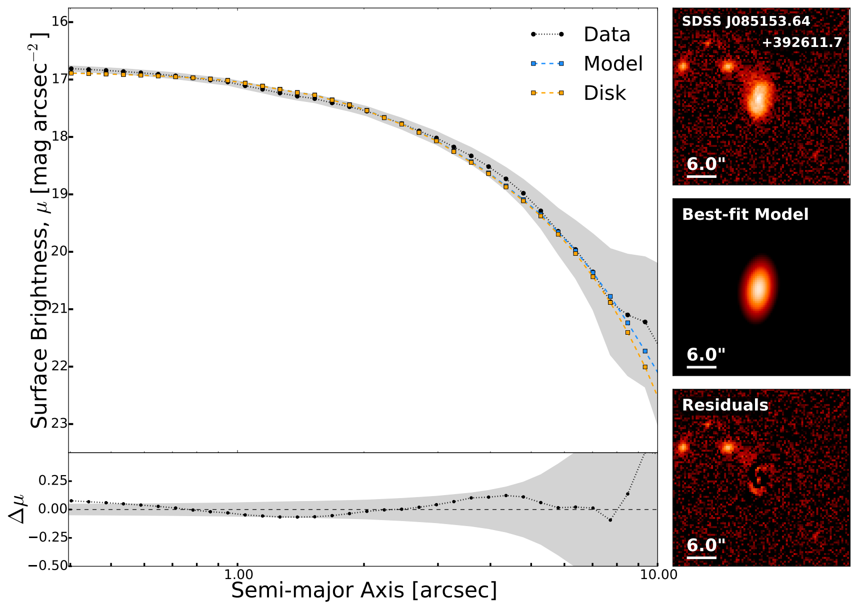

(a)

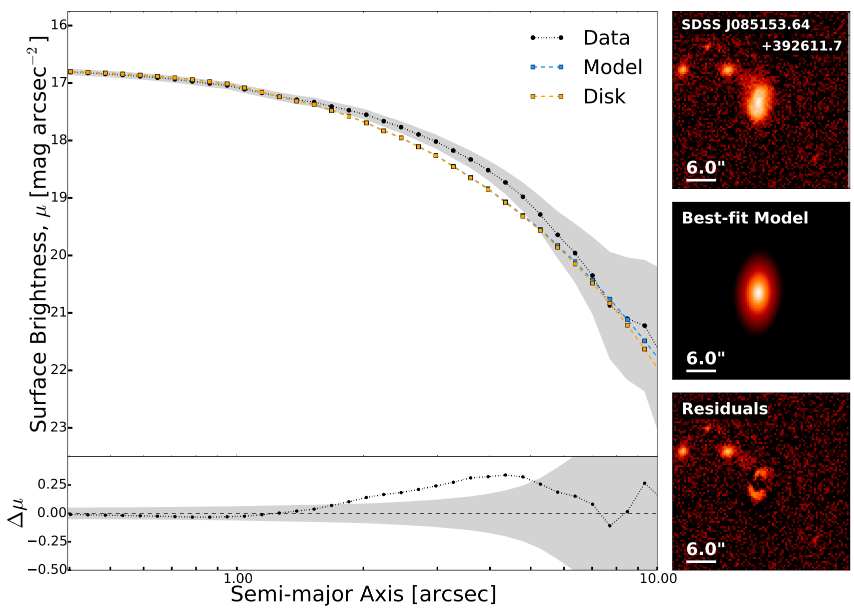

(b)

Figure 2.2: GALFIT decomposition fits to the SDSS image of J0851+3926. Panel (a) is without the outer spirals masked and uses a free Sérsic index, while panel (b) has the spirals masked and the Sérsic is fixed at n = 1. In each figure, the fits of the model and disk to the data (black dotted line) are shown in the top left panel as blue and yellow lines, respectively. The model includes both the disk and sky background component. The bottom left panel shows the residuals to the model fit. The shaded gray areas represent the 1-σ error. The three right panels show postage stamps of the raw SDSS image, best-fit model, and residuals.

masking the spiral arms). Forcing a PSF that is about 6.5 fainter in magnitude than the total galaxy removed all traces of the central residuals of the original fit. Any PSF brighter than this results in an oversubtraction. Thus, we take this PSF to be a strong upper limit to the light contribution by an unresolved bulge. This results in a B/T ≤ 0.003, consistent with the value found by Simard et al. (2011).

To convert this upper limit to a mass, we assumed that the mass-to-light ratio (M/L) is constant throughout the entire galaxy. This is a reasonable assumption since the stellar populations in the disk and bulge components do not differ significantly for disk-dominated galaxies (Graham, 2001). We obtained $M_{\rm stellar}$ from Chang et al. (2015), who provide a catalog of stellar masses using SDSS and WISE photometry. Here, SED fitting was performed using both optical and IR imaging to obtain stellar masses. For J0851+3926, a total stellar mass of $\log(M_{\rm stellar}/M_{\odot}) = 10.61 \pm 0.1$ was calculated, which results in an upper limit to the bulge or pseudobulge mass of $\log(M_{\rm bulge}/M_{\odot}) \leq 8.01$.

2.3.2 BH Mass of J0851+3926

Both the NIRES and NIRSPEC spectra of J0851+3926 clearly show a broad and a narrow component of Paα (see Figs. 2.3 and 6.1). While broad Paα is certainly indicative of AGN activity, Baldassare et al. (2016) and other follow-up studies of AGN candidates with broad emission have shown that supernovae (SNe) and other stellar activity can produce similar broad features. Type II SNe (Pritchard et al., 2012) and luminous blue variables (Smith et al., 2011) are known to produce broad recombination lines up to thousands of kilometers per second. If the broad Paα observed in J0851+3926 were powered by a SN, the broad emission would have persisted for more than 380 days based on the observation dates of our two sets of spectra (see Table 2.1), and this in turn would indicate that the SN would likely be a Type II-P. Using this time scale, we would expect to see other NIR SN features such as O I, Mg I, and Ca I (e.g., Rho et al., 2018). However, we do not see any of these features in either of our NIR observations. Additionally, we would expect the line profile to change significantly over this time (Rho et al., 2018) but our two measurements of the broad Paα width are consistent with each other, 1489 (NIRSPEC) and 1363 (NIRES) km s^{-1} (see Table 2.2).

Another potential origin of a broad line could be powerful outflows powered by star formation. Broad, symmetric components to emission lines are observed in some starburst galaxies, such as NGC 1569 (Martin, 1998; Westmoquette et al., 2008; Manzano-King et al., 2019). However, these galaxies show broad emission in other lines, particularly in [O III]λ5007. To test whether the broad Paα in J0851+3926 is powered by an outflow, we fit the optical lines in the SDSS spectrum by using Bayesian AGN Decomposition Analysis for SDSS Spectra (BADASS[6]; R. Sexton et al. 2020, in preparation), a spectral analysis tool where we included fits to the stellar and Fe II features, as well as multiple components to emission lines. The code allows the user to test for the presence of outflows by setting various constraints on parameters such as amplitude, width, and velocity offset. All reasonable criteria came back negative for outflows, so we forced a blueshifted, outflow component to the [O III]λ5007 fit. We compared the residuals of this forced fit to those fit without outflows and found the residuals to be comparable. This indicates that an outflow component is not needed and that a single gaussian representing narrow-line emission can provide a proper fit to the emission-line profile. Thus, it is likely that outflows that could be affecting the broad

[6] https://github.com/remingtonsexton/BADASS2

line are not present. We conclude that the most likely origin of the observed broad Paα is the BLR of an AGN. As such, we can use this broad line to estimate BH mass using the virial method.

To obtain a BH mass, a common and reliable method is through the virial relation, defined as

$$M_{\mathrm{BH}} = f\frac{V^2 R}{G} \tag{2.1}$$

where f is the virial coefficient; V is the velocity of the broad-line gas that is responding to the continuum variations; R is the distance from the broad emission gas to the central continuum source and is equal to $c\tau$ where τ is the time delay and c is the speed of light; and G is the gravitational constant. The FWHM of the broad emission line, typically seen in Hα or Hβ in the optical, can be used for the value of V. Here, the width of the broad line stems from the Doppler effect of the gas in the accretion disk revolving around the BH. The value of R is estimated empirically using the optical luminosity of the AGN as a proxy (Kaspi et al., 2005; Bentz et al., 2013).

The spectra were fit using EMCEE, an affine-invariant Markov Chain Monte Carlo (MCMC) ensemble sampler (Foreman-Mackey et al., 2013). A broad component and a narrow component, along with a second-order polynomial for the continuum, were fit simultaneously (see Figure 2.3). Both the narrow and broad components were treated as Gaussians with amplitude, FWHM, and offset from rest-frame wavelength as free variables. The BH mass was obtained following the estimators presented by Kim et al. (2018), where they adopted the virial factor log $f = 0.05 \pm 0.12$ derived by Woo et al. (2015). From Kim et al. (2018), their Equation 10,

$$\frac{M}{M_\odot} = 10^{7.07\pm0.04} \left(\frac{L_{\mathrm{Pa}\alpha}}{10^{42}\ \mathrm{erg\ s^{-1}}} \right)^{0.49\pm0.06} \left(\frac{\mathrm{FWHM}_{\mathrm{Pa}\alpha}}{10^{3}\ \mathrm{km\ s^{-1}}} \right)^{2} \tag{2.2}$$

where the FWHM of broad Paα is the analog to the velocity in the virial mass estimator and $L_{\mathrm{Pa}\alpha}$ of the broad component is the analog to the distance to the BLR.

Our NIRSPEC observations were done under heavy cloud cover, making it difficult to accurately estimate the degree of extinction. Thus, the flux and BH values are unreliable, but we leave them listed in Table 2.2 for completeness and show the fit to the spectrum in Appendix 6.1. For the remainder of the article, we will only use our NIRES data for analysis. From Equation (2.2), our NIRES measurements give a BH mass of $(4.47^{+1.87}_{-1.34}) \times 10^{6}\ M_\odot$ (see Table 2.2 for relevant values), where the calculated uncertainties come from the random error estimates. Accounting for systematic uncertainties, virial BH mass estimates typically have errors of 0.4 - 0.5 dex (eg., Shen, 2013; Reines & Volonteri, 2015). We adopt a conservative error estimate of 0.5 dex. For a detailed description on virial mass uncertainties, see Sexton et al. (2019).

Table 2.2: Paα Measurements

Instrument	$\mathrm{Flux_{Broad}}$	$\mathrm{Flux_{Broad}}$ (Ext.)[a]	$\mathrm{FWHM_{Broad}}$	M_{BH}	M_{BH} (Ext.)[a]
	(10^{-15} erg cm^{-2}s^{-1-1})		(km s^{-1})	(10^{6} $M_\odot$)	
NIRSPEC[b]	$0.306^{+0.082}_{-0.073}$	$0.559^{+0.15}_{-1.33}$	1489 ± 184	$2.90^{+2.91}_{-1.56}$	$3.89^{+3.64}_{-2.03}$
NIRES	$1.08^{+0.051}_{-0.050}$	$1.98^{+0.100}_{0.098}$	1363 ± 31	$4.47^{+1.87}_{-1.34}$	$6.05^{+2.23}_{-1.67}$

NOTE: Listed errors are from random errors in the fitting process.
[a] Extinction-corrected values, [b] NIRSPEC measurements are ignored owing to the high extinction caused by heavy cloud cover

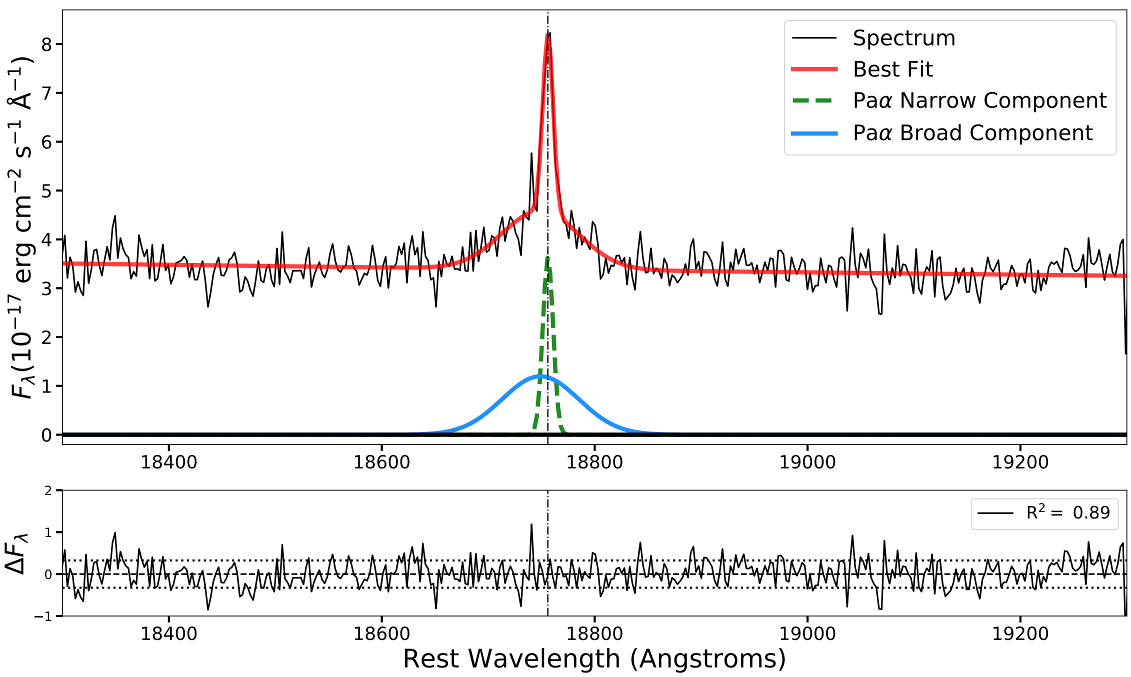

Figure 2.3: The MCMC fit to the NIRES spectrum. In the top panel, Paα is centered with the best fit plotted over the spectrum. Below the spectrum are the narrow (dotted) and broad (solid) components. The bottom panel plots the residuals, the 1σ noise level (horizontal dotted lines), and the R^2 value.

2.3.3 Extinction

The presence of broad Paα and the lack of strong broad lines in the optical imply that there is heavy obscuration present. In order to quantify the extinction toward the BLR, we measured broad hydrogen emission-line ratios and assumed a Cardelli reddening law (Cardelli et al., 1989) with an extinction factor $R_V = 3.1$. While the observed Paβ wavelength fell in a region of strong atmospheric absorption, Paγ emission is observable in the J band, which allowed us to obtain an upper limit to the broad Paγ flux. We also fit the optical SDSS spectrum using BADASS, where fits to the stellar and Fe II features were included (see R. Sexton et al. 2020, in preparation for further details). Two different models were used to fit the data: one excluding broad components (i.e., only narrow components) and the other including broad components (see Fig. 6.2 in Appendix 6.2). No broad Hβ could be properly fit, but the code did converge on a solution to broad Hα. We compared the fits to Hα using the F-test: $F = (\sigma_{single})^2/(\sigma_{double})^2$, where σ is the standard deviation of the residuals using either single or double gaussian components, for which we obtain $F = 1.41$. Based on this, we cannot say for certain whether adding a broad component is justifiable. A value closer to 2 or 3 would provide convincing evidence that a broad component should be fit. Although the fits do suggest that some broad emission is present, deeper observations will be needed to clear the ambiguity of the broad Hα emission.

The observed line ratios from the fits are Paα/Pa$\gamma \geq 6.35$ and Paα/H$\alpha \geq 1.44$. Intrinsic line ratios, Paα/Pa$\gamma = 3.22$ and Paα/H$\alpha = 0.10$, were obtained from Dopita & Sutherland (2003), where we assumed an electron density of $n_e = 10^8$ cm^{-3} and temperature $T_e = 15{,}000$ K. Using the Cardelli reddening law, we estimated an extinction of $E_{\mathrm{Pa}\gamma}(B -$

$V) \geq 1.13$ and $E_{\mathrm{H}\alpha}(B-V) \geq 1.40$. Applying $E_{\mathrm{H}\alpha}(B-V) \geq 1.40$, the extinction-corrected BH mass is $6.05^{+2.23}_{-1.67} \times 10^{6}\ M_{\odot}$, which we will use for the remainder of the article (see Table 2.2 for extinction-corrected values).

This high degree of extinction could explain the lack of other AGN indicators, such as [Si VI]1.963μm and other coronal lines. To quantify whether extinction could explain their absence, we estimate an expected value for the flux of [Si VI] emission based on the observed WISE $W2$(4.6 μm) flux. The objects presented by Müller-Sánchez et al. (2018a) appear to follow a relation between [Si VI] and $W2$ fluxes as log([Si VI]) = 0.74 × log($W2$) - 6.6045 (J. Cann, private communication). After adjusting for extinction, the expected [Si VI] flux is 1.05×10^{-16} erg cm^{-2}s^{-1}. In order to determine whether if this could be detected, we estimate the flux of a gaussian with an amplitude of 1σ of the noise level and a width of the resolution element of the telescope. This resulted in a flux of 1.12×10^{-16} erg cm^{-2}s^{-1}. Thus, any [Si VI] emission will be at most comparable to the noise level. Since [Si VI] is one of the most prominent coronal lines in the NIR, we also do not expect to see other coronal line features.

2.3.4 X-Ray Observations

The absorbing hydrogen column density (N_{H}) of Sy2 galaxies is expected to be high, on the order of $\sim 10^{23}$ cm^{-2} (Jaffarian & Gaskell, 2020). This is consistent with the unified model, where the active nuclei in Sy2 galaxies are believed to be heavily obscured due to orientation effects. Coupled with the high-extinction estimates calculated in Section 2.3.3, it is not surprising that we did not detect any statistically significant X-ray emission in the *Chandra* observations. We calculated a 3σ upper limit on the counts, $\sim$ 6, and assuming a power-law index of 1.8, the upper limit to the hard X-ray 2 – 10 keV luminosity, $L_{2-10\ \mathrm{keV}}$ was estimated to be 1.21×10^{41} erg s^{-1}. Using Equation (1) from R. W. Pfeifle et al. (2020, in preparation), a column density can be estimated from $L_{2-10\ \mathrm{keV}}$ and the WISE 12μm luminosity ($L_{12\mu\mathrm{m}}$). We found a lower limit line-of-sight column density of $\log(\mathrm{N_H}/\mathrm{cm}^{-2}) \geq 24.43$, which suggests that the obscuring region is Compton thick. This estimate of N_H along with the results presented in Jaffarian & Gaskell (2020) implies an $E(B-V) > 1.0$, which is consistent with the extinction values calculated in Section 2.3.3. This heavy obscuration supports the lack of any significant broad emission seen in the optical spectra.

2.3.5 Rotation Curve

Visible in both the NIRSPEC and NIRES 2D spectra is extended narrow Paα emission that traces the gas in the disk out to about 8 kpc. The spatially resolved narrow emission allows us to construct a rotation curve. Plotted in Figure 2.4 are two rotation curves based on different slit orientations, one along the semi-major axis (top) and the other oriented almost perpendicular to that (bottom). For each curve, velocities were measured in either ∼0.25 or ∼0.5 kpc increments out to the edge of the disk and are color-coded to represent approaching (blue) and receding (red) gas. The fits to the extended emission were done using the same EMCEE routine as was used in Section 2.3.2. The inclination angle is taken from the output of GALFIT (see Figure 2.2). Plotted in gray is the expected velocity curve using a Navarro-Frenk-White (NFW) dark matter density profile (Navarro

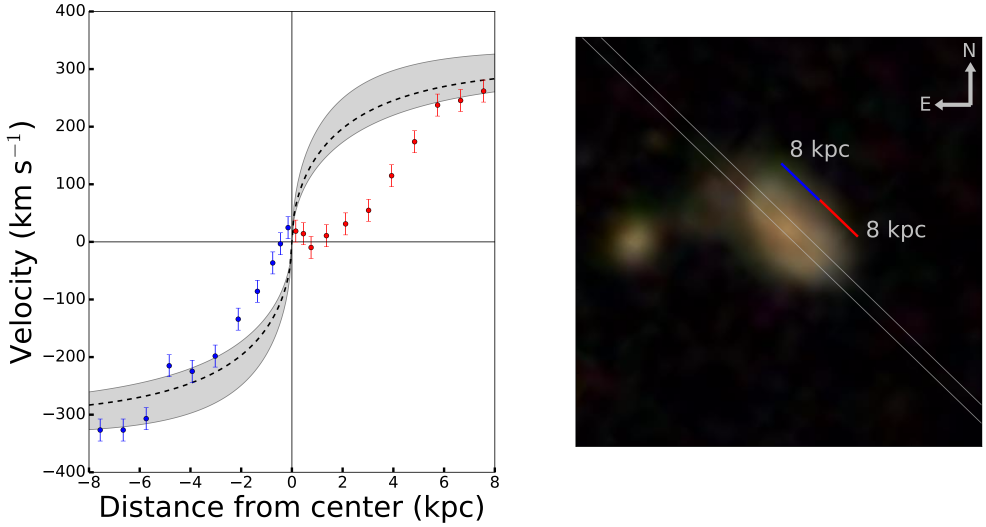

(a)

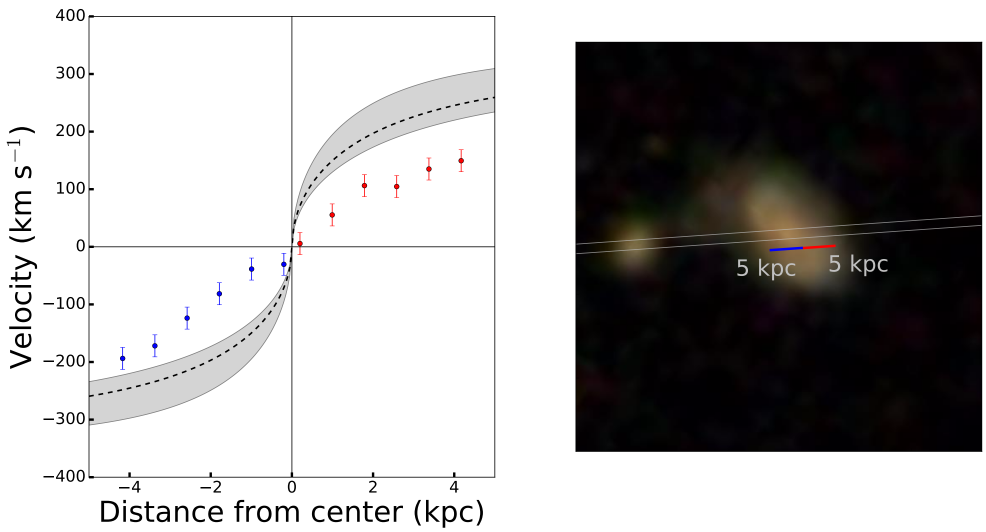

(b)

Figure 2.4: Rotation curves of J0851+3926. A NFW profile is plotted for reference in the left panels. The shaded gray region represents the concentration parameter varying from 8 to 15, with 10 represented as the dotted line. The extended narrow-line velocities of Paα, blue for approaching and red for receding gas, are plotted against their distance from the center in kpc. On the right, the orientation of the slit is shown as a white strip, while the colored lines correspond to the direction of the gas and the distance to which the extended emission is detectable.

et al., 1996). The width of the curve arises by varying the concentration parameter from 8 to 15, with the dotted line representing a value of 10.

As shown in the top panel of Figure 2.4, there appears to be counterrotating gas within the central kpc. This counterrotation is not apparent when the slit is oriented $+60°$ (bottom panel). The limited extension of the counter-rotation and the orientation of the slit along the central component of the spiral could suggest that a bar is causing the velocity disruption. Another scenario that could explain this counterrotation is a fly-by of a possible companion galaxy. We discuss these scenarios further in Section 2.4.3.

2.4 Discussion

The virial method offers one of the most reliable methods of estimating BH masses, and J0851+3928 is one of only a handful of known bulgeless galaxies for which BH mass can be estimated by this method. In the following sections, we first compare the $M_{\rm BH}$ of J0851+3928 to those of other bulgeless galaxies, followed by a comparison to a much broader sample that includes all morphological types. We compare $M_{\rm BH}$ to both the galactic bulge mass ($M_{\rm bulge}$) and total stellar mass of the galaxy ($M_{\rm stellar}$). Note that the estimates for $M_{\rm BH}$ used here come from methods using the gravitational potential of the SMBH (viral mass estimators) or those using the AGN as the flux source (X-ray estimates). We refrain from using BH masses derived from relations based on galaxy properties, including $M_{\rm BH}$-σ and $M_{\rm BH}$-ϕ (spiral arm pitch angle).

2.4.1 Comparisons with Other Bulgeless Galaxies

One of the first examples of an AGN in a bulgeless galaxy in the literature is NGC 4395, a nearby Sy1 galaxy hosting an intermediate-mass BH (IMBH; Filippenko & Sargent, 1989; Filippenko & Ho, 2003). Ultraviolet reverberation mapping has estimated the BH mass to be $(3.6 \pm 1.1) \times 10^6$ $M_\odot$ (Peterson et al., 2005) and this has been verified by subsequent direct dynamical mass measurements (den Brok et al., 2015). Jiang et al. (2011) report seven broad-line AGN (only 5% of their sample) where a pure exponential disk provided the best fit, indicating the lack of a bulge component. BH masses in this sample range from $10^{4.8}$ to $10^{6.2}$ $M_\odot$. As noted by the authors, four of these have bar structures and the bright AGN at the center could hide a small bulge. Simmons et al. (2017) provide a large sample (101 galaxies) of type 1 AGN in disk-dominated galaxies with BH masses ranging from 2×10^6 to 9×10^8 $M_\odot$. However, the mean B/T of this sample is 0.5, possibly caused by the light contribution from the AGN.

Unsurprisingly, only a handful of bulgeless Sy2 galaxies have estimates for $M_{\rm BH}$. Most of these observations are confined to IR and X-rays measurements due to the obscuration present in Sy2 galaxies. One such example is NGC 3621, which was first discovered to have AGN activity through IR detections of [Ne V] at 14 and 24 μm (Satyapal et al., 2007). Subsequent observations of X-ray emission (Gliozzi et al., 2009) and stellar-dynamical modeling of the nuclear star cluster (Barth et al., 2009) have placed $M_{\rm BH}$ between 4×10^3 and 3×10^6 $M_\odot$. [Ne V] detection at 14 μm was also detected in NGC 4178 (Satyapal et al., 2009). Follow-up X-ray observations (Secrest et al., 2012) indicate a $M_{\rm BH}$ between 10^4 and 10^5 $M_\odot$. Shields et al. (2008) discovered a low-luminosity IMBH in NGC 1042 with an upper limit to $M_{\rm BH}$ calculated at 3×10^6 $M_\odot$ based on the mass of the nuclear star cluster. McAlpine et al. (2011) present two bulgeless galaxies, NGC 3367 (recently identified as a narrow-line Seyfert 1) and NGC 4536. X-ray and [Ne V] detections give estimates of $M_{\rm BH}$ in the range of 10^5 — 10^7 $M_\odot$ and 10^4 — 10^6 $M_\odot$ for NGC 3367 and NGC 4536, respectively. Other bulgeless Sy2 galaxies have only X-ray observations. These include NGC 4561, which has a calculated lower mass limit of 2×10^4 $M_\odot$ (Araya Salvo et al., 2012), and NGC 3319, a barred galaxy hosting an IMBH with an estimated upper limit of 3×10^5 $M_\odot$ (Jiang et al., 2018). With $M_{\rm BH} \approx 10^{6.78}$, J0851+3928 is more massive (in some cases over an order of magnitude) than the other Sy2 bulgeless galaxies listed here.

In Figure 2.5, we plot $M_{\rm BH}$ vs. $M_{\rm stellar}$ for the bulgeless sample described above. Three additional bulgeless galaxies from Bentz & Katz (2015) and Davis et al. (2017) are included (see Tables 6.2 and 6.4 in Appendix 6.3 for mass measurements). In addition, Rakshit et al. (2017) obtained Hα line measurements of the NLS1 galaxy NGC 3367, from which we calculated $M_{\rm BH}$ using the updated virial mass estimator from Woo et al. (2015) that incorporates the new value of log $f = 0.05 \pm 0.12$ ($f = 1.12$),

$$\frac{M}{M_\odot} = 10^{5.594 \pm 0.12} \left(\frac{L_{\rm H\alpha}}{10^{42}\ {\rm erg\ s^{-1}}} \right)^{0.46} \left(\frac{\rm FWHM_{H\alpha}}{10^3\ {\rm km\ s^{-1}}} \right)^{2.06} \tag{2.3}$$

References for stellar masses and all values are summarized in Appendix 6.3 and Table 6.1. If uncertainties are not given, then they are assumed to be 0.3 dex.

The line of best fit and confidence intervals were calculated using a Bayesian approach with linear regression done by EMCEE (note that J0851+3928 was not included in this fit). A component of intrinsic scatter was not included due to the significant overlap of

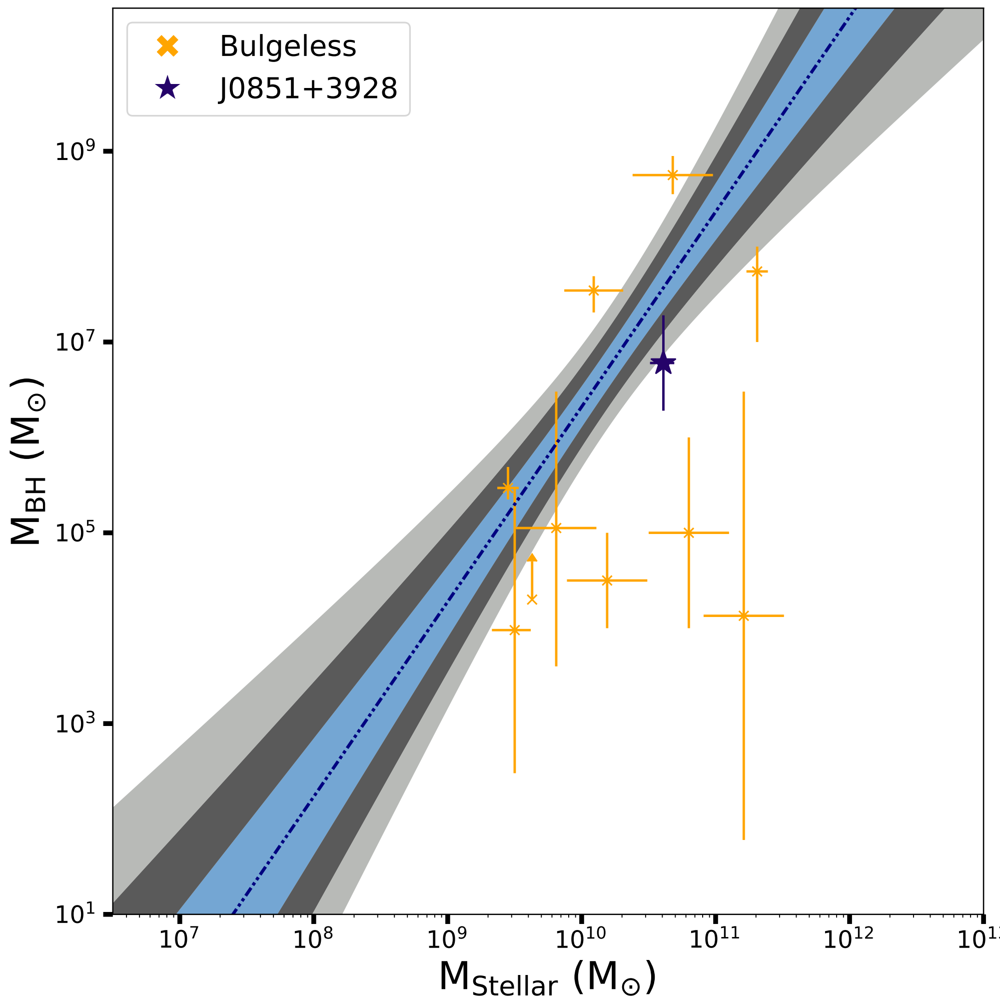

Figure 2.5: $M_{\rm BH}$ plotted versus $M_{\rm stellar}$ for purely bulgeless galaxies. J0851+3928 is represented as a blue star, and its error bars for stellar mass are comparable to the size of the star symbol. The shaded contours are set at 1σ confidence intervals, and the dashed-dotted line represents the line of best fit (excluding J0851+3928).

the large error bars. The best-fit line is weighed more heavily toward the higher-mass BHs with dynamical mass estimates due to their smaller uncertainties. Fitting only the X-ray observations increased the uncertainty of the slope by almost a factor of 5. Because of the small sample size and large uncertainties, a reliable fit is difficult to make. The virial estimate of $M_{\rm BH}$ for J0851+3928 puts it 0.77 dex below the relation but within the scatter of the other $M_{\rm BH}$ with virial and dynamical mass estimates. This indicates that the bulgeless BH masses calculated from X-rays are likely lower limits. This is not surprising since many of these galaxies are Sy2, where their high levels of extinction and large column densities can heavily obscure X-ray measurements.

2.4.2 $M_{\rm BH}$ Relations

Simmons et al. (2013, 2017) have suggested that SMBHs in disk-dominated galaxies are overmassive in the $M_{\rm BH}$–$M_{\rm bulge}$ relation and seem to outgrow their bulge through secular processes unrelated to major mergers. In addition, they found that these SMBHs follow the $M_{\rm BH}$–$M_{\rm stellar}$ relation more closely. In order to compare J0851+3928 to these results, we formed an extensive sample that incorporates a range of morphological types with both Sy1 and Sy2 galaxies, including those with pseudobulges. The primary purpose here is to show how J0851+3928 compares to a large sample of galaxies. The following sections describe the sample and papers used, and all measurements are compiled in Appendix 6.3. The full data set is also available for download.

2.4.2.1 BH, Bulge, and Total Stellar Masses

The AGN BH Mass Database [7] (Bentz & Katz, 2015) provides a compilation of BH masses from reverberation mapping studies. The basic method of reverberation mapping is to monitor variations in the continuum flux and broad emission lines and measure the light-travel time delay between the two. $M_{\rm BH}$ are derived from these measurements using the virial relation given by Equation (2.1). To properly compare the $M_{\rm BH}$ of J0851+3926 calculated using Equation (2.2), we need to adopt a consistent value of f. Because the reverberation masses in the database are σ based, we use $\log f = 0.65 \pm 0.12$ ($f = 4.47$) as calibrated in Woo et al. (2015). $M_{\rm BH}$ of 37 galaxies with reliable bulge and stellar masses are listed in Table 6.2 (see Appendix 6.3). The quoted errors include uncertainties from both the database and from f, where most of the uncertainty arises.

Graham & Scott (2015) compiled data from several different studies and selected the low-mass AGN whose $M_{\rm BH}$ are undermassive relative to the $M_{\rm BH}$–$M_{\rm Bulge}$ relation. These BH masses were calculated using single-epoch virial mass estimators that require the use of the virial coefficient. We use the updated value of f ($f = 1.12$) (Woo et al., 2015), as was done in Sections 2.3.2 and 2.4.1. Due to the need to recalculate all single-epoch mass measurements, we only select AGN from Graham & Scott (2015) that have quoted emission-line measurements. The majority of the BH masses were calculated using Equation (2.3); however, for Pox 52, where λL_{5100} and $\mathrm{FWHM}_{\mathrm{H}\beta}$ are reported, we followed the relation derived in Sexton et al. (2019),

[7] http://www.astro.gsu.edu/AGNmass/

$$\frac{M}{M_\odot} = 10^{6.867^{+0.155}_{-0.153}} \left(\frac{\lambda\, L_{5100}}{10^{44}\ \mathrm{erg\ s^{-1}}}\right)^{0.533^{+0.035}_{-0.033}} \times \left(\frac{\mathrm{FWHM_{H\beta}}}{10^3\ \mathrm{km\ s^{-1}}}\right)^2 \tag{2.4}$$

which also incorporates the updated f value. Values for M_{BH} and the references of the measurements are listed in Table 6.3 (see Appendix 6.3). The errors reported for M_{BH} include the quoted uncertainties in $L_{\mathrm{H}\alpha}$, λL_{5100}, $\mathrm{FWHM_{H\alpha}}$, $\mathrm{FWHM_{H\beta}}$, and f.

The rest of the BH masses in our sample were derived using dynamical mass measurements, including stellar dynamics, gas dynamics, stellar orbit motions, and stimulated water maser emission. We compile M_{BH} from the following papers: all 44 late-type galaxies in Davis et al. (2017), 39 early-type galaxies from Sahu et al. (2019), 37 galaxies from Savorgnan et al. (2016), and 3 galaxies from Hu (2009). Masses and uncertainties are quoted from each paper and can be found in Table 6.4 (see Appendix 6.3).

We also quote M_{bulge} and M_{stellar} values from the literature. These values are listed in Tables 6.2–6.4 and are predominately calculated from color-dependent stellar M/L ratios. The general procedure is to perform 2D bulge/disk decompositions while simultaneously fitting for any structural features such as spiral arms, rings, and bars. Based on the surface brightness profiles, one can obtain apparent and absolute magnitudes from which luminosities can be estimated. With the appropriate M/L ratio, a mass for each component can be calculated. A summary of the methods used to calculate bulge and total stellar mass in each referenced source is presented in Appendix 6.3. If uncertainties are not specified, then they are assumed to be 0.3 dex.

Lastly, some quoted M_{bulge} are greater than their host stellar masses. Although this could naturally come from the use of different methods of fitting or different M/L ratios used, the mass discrepancy could also arise as a result of color differences of the components. For example, in the case of late types in Bentz & Manne-Nicholas (2018), the bulge will tend to be redder and have a higher $V-H$ than the disk. A single $V-H$ that represents the entire galaxy will be bluer, which results in a $M_{\rm stellar}$ that is less than $M_{\rm bulge}$. The differences, however, are typically within the quoted uncertainties.

2.4.2.2 $M_{\rm BH}$-$M_{\rm bulge}$ Relations

We first fit $M_{\rm BH}$ and $M_{\rm bulge}$ data described above using EMCEE in a similar fashion to what was done in Section 2.4.1; however, a component of intrinsic scatter was included in the fit. This was done since there is not a significant amount of overlap in the error bars. We fit each morphological type individually before fitting the entire sample (note that J0851+3926 was not included). The results of the latter are shown in the left panel of Figure 2.6. Included in the figure are shaded σ-confidence intervals of the fit, and we find the best-fit relationship to be

$$\log\left(\frac{\rm M_{BH}}{\rm M_{\odot}}\right) = (1.14 \pm 0.05)\log\left(\frac{\rm M_{bulge}}{10^{10}\ \rm M_{\odot}}\right) + (7.47 \pm 0.06) \qquad (2.5)$$

with an intrinsic scatter of 0.56 dex.

To investigate any potential systematic differences in the various mass calculations used, we also fit each subsample individually. The resulting fits all fall within 1 dex of each other, with only a couple diverging further at the low- and high-mass ends where there is a lack of data to constrain the fit. The majority of the fits, however, are consistent with the best-fit line for the entire sample, with only slight offsets in the y-intercept. We also investigated the morphological dependence of the sample and found that early-type galaxies have a steeper slope (1.13 ± 0.07) than late-type galaxies (0.81 ± 0.11). Davis et al. (2019) found that late-type galaxies had a steeper slope; however, our sample includes low-mass early-type galaxies that cause our slope to increase. Interestingly, we investigated the scatter and find that it does not increase significantly (<10%) when sampling lower B/T ratios. This may indicate that even if the mechanism for growing small bulges or pseudobulges is different from that of larger bulges, the resulting bulges/pseudobulges scale with their BHs in a similar manner.

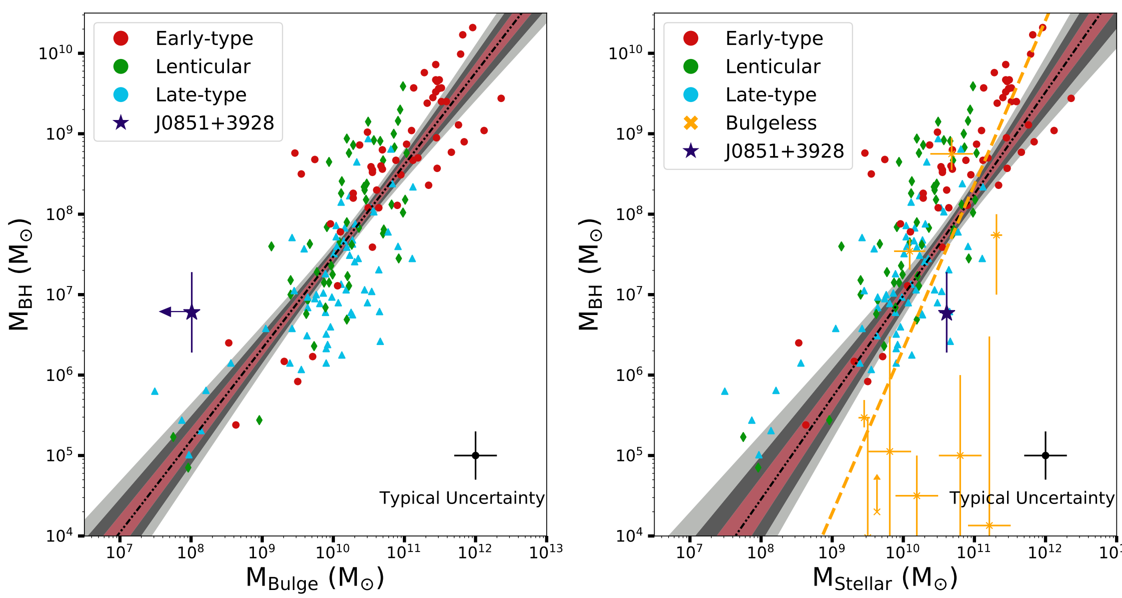

Figure 2.6: $M_{\rm BH}$ plotted versus $M_{\rm bulge}$ (left) and $M_{\rm stellar}$ (right). J0851+3928 is represented as a blue star, and the upper limit to $M_{\rm bulge}$ is used here. Error bars for the stellar mass are comparable to the size of the star symbol. The shaded contours are set at 1σ confidence intervals, and the black dashed-dotted line represents the line of best fit (excluding J0851+3928 and the bulgeless targets with only X-ray observations). The orange dashed line in the right panel represents the best-fit line to the bulgeless galaxies as is shown in Figure 2.5. The full list of individual values and uncertainties are found in Tables 6.2, 6.3 and 6.4 (see Appendix 6.3).

In Section 2.3.1 we obtained an upper limit to the bulge mass of J0851+3928 by forcing the fit of an unresolved component to the central region of the galaxy. The result indicated that if indeed an unresolved bulge is present in J0851+3928, it is at least 400 times fainter than the disk. Taken at face value, the upper limit of $M_{\rm bulge} \leq 10^{8.01}$ $M_\odot$ would indicate that J0851+3928 hosts an overmassive BH compared to what the $M_{\rm BH}$ - $M_{\rm bulge}$ relation would predict: J0851+3928 is 1.59 dex above the best-fit relation (Fig. 2.6, left panel), a factor of 2.84 above the scatter. Fitting only late types, we find J0851+3928 to be 1.25 dex above the fit, a factor of 2.40 above the scatter. For galaxies with similar $M_{\rm BH}$ (within $10^{6.0}$–$10^{7.0}$ $M_\odot$), the bulge mass of J0851+3928 is at least 3.50σ below the median.

2.4.2.3 $M_{\rm BH}$-$M_{\rm stellar}$ Relation

We used the same linear regression method to fit the $M_{\rm BH}$ and $M_{\rm stellar}$ data as was done for $M_{\rm BH}$–$M_{\rm bulge}$. The results of the fit to the entire data set are shown in the right panel of Figure 2.6 and the best-fit line is

$$\log\left(\frac{\rm M_{BH}}{\rm M_\odot}\right) = (1.26 \pm 0.09)\log\left(\frac{\rm M_{stellar}}{10^{10}\ \rm M_\odot}\right) + (6.99 \pm 0.10) \tag{2.6}$$

with an intrinsic scatter of 0.76, 0.20 dex higher than $M_{\rm BH}$ - $M_{\rm bulge}$.

Like the $M_{\rm bulge}$ relations, the various $M_{\rm stellar}$ relations of each subsample do not diverge beyond 1 dex of each other within the low- and high-mass ends. The slope of the early types is steeper than late types, 1.24 ± 0.10 vs. 1.02 ± 0.15. We also find the slope of the $M_{\rm BH}$–$M_{\rm stellar}$ relation (1.26 ± 0.10) to be steeper than the $M_{\rm BH}$–$M_{\rm bulge}$ relation (1.15 ± 0.06), which is in agreement with Davis et al. (2018) and Bentz & Manne-Nicholas (2018).

The fact that $M_{\rm BH}$ - $M_{\rm stellar}$ is steeper is not surprising since the most massive galaxies hosting the most massive BHs typically have higher B/T flux ratios (Davis et al., 2018). This causes galaxies with higher $M_{\rm bulge}$ to be shifted toward the right in the $M_{\rm BH}$–$M_{\rm bulge}$ relation, thus lowering the steepness of the slope.

Similar to the results found by Simmons et al. (2013, 2017), J0851+3928 does fall closer to the $M_{\rm BH}$ - $M_{\rm stellar}$, differing by 0.97 dex, which is a factor of 1.28 below the relation. Also, it is well within the distribution of the late-type galaxies, the most morphologically similar subsample, and only differs by 0.37 dex of the late-type best fit (not shown).

Also plotted in Figure 2.6 is the $M_{\rm BH}$ - $M_{\rm stellar}$ relation for bulgeless galaxies from Figure 2.5. The bulgeless X-ray galaxies were not included in the full sample that produced Equation (2.6). We see a decrease in the slope of the full sample, which is likely driven by the handful of galaxies at the low-mass end that have higher $M_{\rm BH}$ estimates than the X-ray sources. In addition, the offset of the X-ray sources from the full sample further indicates that these are lower limits to the BH mass. The other bulgeless galaxies with virial estimates for $M_{\rm BH}$, including J0851+3928, fall closer to the relation, and J0851+3928 falls well within the scatter of the other late type galaxies. The fact that all four of the bulgeless galaxies with robust estimates fall amongst both early and late-types suggests that perhaps the major BH growth mechanisms in bulgeless galaxies are not all that different. Although the sample size is still too small to make any firm conclusions, it is certainly intriguing how these BHs in bulgeless galaxies grew to supermassive size without going through major merger events.

2.4.3 Triggering of the AGN

The existence of a BH on the order of $10^{6.8}$ $M_{\odot}$ in a galaxy with no obvious signatures of a major merger raises the important question of how it has grown to supermassive size. To trigger accretion, an inflow of gas needs to be supplied to the central region. A natural mechanism of this is a galaxy merger in which large quantities of gas can be sent toward the BH. The buildup of the bulge component is thought to accompany major mergers, so a different triggering mechanism likely triggered the AGN activity observed in J0851+3928. In this section, we discuss two possible scenarios of how the current accretion onto the BH may have started: fly-by of a companion galaxy and a galactic bar that can remove angular momentum from the gas.

The SDSS postage stamp (top right panel of Figure 2.2) shows a small galaxy about $9''$ away with some low surface brightness emission potentially connecting it to J0851+3928. If this galaxy is indeed a companion rather than a close projection, a tidal interaction with J0851+3928 could have disrupted the gas in the disk. If, in addition, this companion were gas-rich, some of the gas could have been accreted by the larger galaxy, possibly explaining the counterrotation observed in Section 2.3.5. In either case, the tidal interaction could have provided the means to remove angular momentum from the gas, thus funneling it onto the central engine.

To investigate whether the small galaxy is a tidal companion, we obtained NIRES spectra to measure its redshift (see Figure 2.4b for slit orientation). Unfortunately, the spectrum did not show any obvious emission or absorption features in any of the NIRES bands. Thus, the only redshift value available is the photometric redshift (PhotoZ) from

SDSS. SDSS reports a PhotoZ = 0.257 ± 0.0630, compared to PhotoZ = 0.088 ± 0.0234 and spectroscopic redshift (SpecZ) = 0.129584 (± 1.2×10^{-5}) for J0851+3928. If this redshift is accurate, then the small object is a background galaxy rather than a close companion. This is consistent with the fact that we find no asymmetries in the residuals of the GALFIT decompositions (see Figure 2.2), suggesting that the inner disk is largely intact and substantial interaction is unlikely.

Many studies have shown that galactic bars are quite common in nearby spiral galaxies and may play a pivotal role in the secular evolution of AGN (eg., Eskridge et al., 2000; Jogee et al., 2005). Due to the nonaxisymmetric distributions of mass, galactic bars may help drive gas toward the center through gravitational torques that reduce the angular momentum of the gas, thus driving it inward toward parsec scales (eg., Piner et al., 1995; Sheth et al., 2002; Wang et al., 2012). Bar formation could have arisen from disk instabilities induced by a close fly-by or cold gas accretion from dark matter filaments (Combes, 2008). Through intersecting filaments, Algorry et al. (2014) have shown that a galactic bar can arise due to an inner counterrotating disk or bar. This can occur if accretion along the filaments occurs in different episodes, where the inner bar forms first, followed by the outer disk at a later time. Close inspection of J0851+3928 reveals the possibility of a bar-like structure. Figure 2.7 shows a contour, set at an arbitrary level, that emphasizes the spiral arms and possible bar structure. In contrast, no clear bar-like feature is seen in the GALFIT decompositions (see Figure 2.2). In order to better characterize the central region, higher-resolution data are needed to resolve the central kpc.

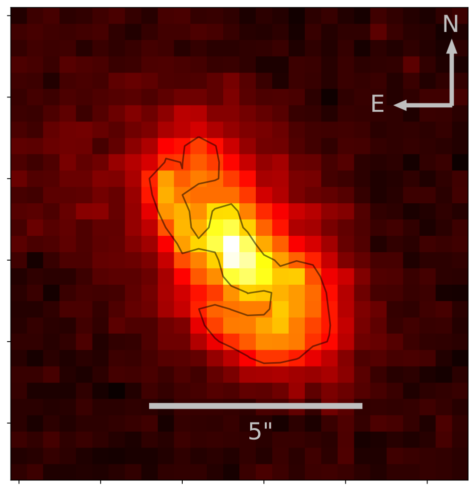

Figure 2.7: Flux plot of J0851+3926. The contour level is arbitrarily set to bring out the spiral arm structure.

2.5 Conclusion

We have obtained NIRSPEC and NIRES NIR spectra and *Chandra* X-ray observations of SDSS J085153.64+392611.76, a bulgeless, Sy2 galaxy with broad Paα emission. This offers us the special opportunity to obtain a virial BH mass estimate while also allowing us to put strong constraints on any potential galactic bulge. Using virial mass estimators, we calculated an extinction-corrected BH mass of $\log(M_{\rm BH}/M_{\odot}) = 6.78 \pm 0.50$. There is some ambiguity to the presence of AGN activity in the SDSS spectrum that showcases that NIR selection techniques could be better suited in selecting and studying AGN that are deeply buried in dust. Our lack of X-ray detection is consistent with this scenario of a heavily obscured AGN and highlights the need for IR spectroscopic observations to uncover hidden BHs in this demographic. Additionally, the lack of a bulge component in J0851+3926 indicates that it is unlikely to have undergone a major merger event and that the central

BH has grown to a supermassive size quiescently. Clearly, some secular mechanism, likely independent from mergers, can fuel AGN and grow SMBHs.

We compiled a substantial sample of AGN, including those found in bulgeless galaxies, and find that J0851+3926 falls within the scatter of the $M_{\rm BH}$–$M_{\rm stellar}$ relation. In addition, the virial mass estimate of the BH mass provides one of the most secure mass estimates of a bulgeless Sy2 galaxy. Since it does not have a bulge component, we find that the $M_{\rm BH}$–$M_{\rm stellar}$ relation is more reliable for bulgeless galaxies or those with pseudobulges than the $M_{\rm BH}$–$M_{\rm bulge}$ relation. Obtaining total stellar mass of the galaxy is more straightforward than deconvolving the galaxy into individual components, particularly when the structures are not well resolved.

We also report counterrotation of gas within the central kpc of J0851+3926. Possible causes of this include a potential faint bar that is changing the angular momentum of the gas or a close fly-by of a companion galaxy that disrupted the gas in the disk. Higher-resolution observations will be needed to search for further evidence of a bar and/or traces of tidal interactions.

Chapter 3

Near-Infrared Coronal Line Observations of Dwarf Galaxies hosting AGN-driven Outflows

3.1 Introduction

It is now well accepted that supermassive black holes (BHs) lie at the center of most massive galaxies. Strong correlations have supported the idea that they evolve with their host galaxies and feedback from the active galactic nuclei (AGN) has been shown to regulate star formation (for a review, see Kormendy & Ho, 2013). Powerful, AGN-driven outflows are believed to suppress star formation (Rupke et al., 2017; U et al., 2019) in high-mass galaxies, leading their hosts to the well-defined red sequence.

The general consensus regarding feedback in dwarf galaxies ($M_\star < 10^{10}\ M_\odot$) is that stellar processes, such as starbursts and supernovae (SNe), provide the main source of quenching (eg., Veilleux et al., 2005, 2020; Heckman & Thompson, 2017). However, the growing rate of AGN detections in dwarf galaxies (Reines et al., 2013; Moran et al., 2014; Sartori et al., 2015) necessitates a closer look at AGN feedback in the low-mass regime. Evidence of AGN-driven feedback in dwarf galaxies is already starting to emerge. Penny et al. (2018) presented a sample of dwarf galaxies with AGN line ratios and kinematically disturbed gas at their centers possibly due to AGN feedback. In addition, Bradford et al. (2018) found a sample of isolated ($>$ 1Mpc), gas-depleted dwarfs with optical line ratios indicative of AGN activity, which suggests that AGN may play a role in clearing gas from dwarf galaxies.

The shallower gravitational potential wells of dwarf galaxies allow feedback mechanisms to have a more profound effect on the global interstellar medium. Although this means dwarf galaxies are more susceptible to external environmental effects, strong outflows may be capable of driving gas beyond the dark matter halo. To investigate this possibility, Manzano-King et al. (2019), hereafter MK19, observed a sample of 29 isolated dwarf galaxies with optical and IR signatures suggestive of AGN activity. Nine of these show fast outflows with a median speed of $\sim$645 km s^{-1}, higher than the median host escape velocities of $\sim$300 km s^{-1}. If the outflows are of AGN origin, this would suggest that AGN feedback could eject material beyond the dark matter halo and have a substantial impact on the star formation rate. Furthermore, follow-up integral field spectroscopy done by Liu et al. (2020, hereafter L20) of this sample showed spatially extended outflows up to 3 kpc in a number of these targets. In addition, they detected outflow velocities greater than 500 km s^{-1} in six of these galaxies. Indeed, a small but non-negligible fraction (up to 6%) of the ionized outflowing gas has the necessary speeds to escape their galaxy.

However, line ratios from star-forming processes can sometimes mimic those of AGN and some contamination exists between the AGN and star-forming regions of the Baldwin, Phillips & Terlevich (hereafter BPT; Baldwin et al., 1981) diagram (eg., Allen et al., 2008; Rich et al., 2011). Moreover, L20 found core-collapse SNe to be energetic enough to drive the mass outflow rates (3×10^{-3} — 0.3 $M_{\odot}$ yr^{-1}) seen in their sample, and thus the contribution of stellar processes in driving the outflows cannot be formally ruled out.

To further characterize the kinematics of outflows, coronal lines (CLs) have been used as an additional tracer of outflows. CLs are forbidden transitions from highly ionized (>100 eV) species with widths suggesting the CL region lies between the broad and narrow-line regions (De Robertis & Osterbrock, 1984, 1986; Penston et al., 1984; Erkens et al., 1997; Rodríguez-Ardila et al., 2002, 2006). Due to the high energies needed for their ionization, CLs are excellent indicators of AGN activity. They are often observed blueshifted relative to the systemic velocity of the host galaxy and thus are believed to be linked with outflows. Müller-Sánchez et al. (2011) have measured outflow speeds upwards of 1500 km s^{-1} through CL emission, and the velocity fields suggest the outflows are of biconical shape with collimation likely due to the torus (see Standard Model, Antonucci, 1993).

In this article, we present follow-up near-infrared (NIR) spectroscopy of the nine dwarf galaxies from MK19 and L20 that show optical AGN line ratios and fast outflows.

Through NIR diagnostics, we aim to confirm the presence of AGN activity and characterize the outflows through NIR emission lines. Details of the sample selection, observations, and data reduction are summarized in Section 3.2. Analysis of the data, including spectra fitting and AGN diagnostics, are covered in Section 3.3. In Section 3.4, we discuss the NIR emission lines and outflow characteristics. Throughout this article, we adopt a standard Λ cold dark matter cosmology with $H_0 = 70$ km s^{-1} Mpc^{-1}, $\Omega_M = 0.3$, and $\Omega_\Lambda = 0.7$.

3.2 Data and Observations

3.2.1 Sample Selection

Our sample of nine dwarf galaxies is from the AGN sample of MK19. Briefly, Reines et al. (2013), Moran et al. (2014), and Sartori et al. (2015) have identified hundreds of dwarf galaxies with optical and IR signatures indicative of AGN activity. MK19 created a subsample of candidate AGN whose optical line ratios place them above the star-forming region of the BPT and Veilleux & Osterbrock 1987 (hereafter VO87; Veilleux & Osterbrock, 1987) line ratio diagrams or that have He II λ4686 emission (see Shirazi & Brinchmann, 2012). They obtained Keck Low Resolution Imaging Spectrometer (LRIS; eg., Oke et al., 1995; Rockosi et al., 2010) spectroscopy of 29 of these galaxies, nine of which showed blue asymmetries in their [O III] λ5007 profile. This blue wing is often regarded as an indicator of outflowing gas, where the asymmetry arises due to the redshifted gas being blocked from our line of sight. These nine dwarf galaxies with spatially extended outflows form our sample for this article. Their stellar masses range from $8.77 < \log(M_*/M_\odot) < 9.97$ (median of 9.34), and all have a redshift of $z < 0.05$.

3.2.2 Observations and Reductions

NIR spectroscopy was obtained on three separate dates: on 2017 October 29 using Keck II NIRSPEC (McLean et al., 1998) and on 2018 October 25 and 2019 January 25 with Keck II Near-Infrared Echellette Spectrometer (NIRES; Wilson et al., 2004). NIRSPEC is a NIR echelle spectrograph with a wavelength coverage ranging from 0.9 — 5.5 μm. The NIRSPEC-7 filter was used in low-resolution mode with a cross-dispersion angle of 35.31°. This resulted in a wavelength coverage of ∼1.97 — 2.39 μm. The $42'' \times 0.76''$ slit was used, and a spectral resolution of 196 km s^{-1} ($R \approx 1500$) at 2.20 μm was measured with a seeing of ∼0.50″. Observations throughout the night were done under mostly clear conditions. Note that these observations were done before the NIRSPEC upgrade. NIRES is an NIR echelette spectrograph with the slit being $18'' \times 0.55''$, and the wavelength coverage set from 0.94 — 2.45 μm across 5 orders. There is a small gap in coverage between 1.85 and 1.88 μm, but this is a region of low atmospheric transmission. The average spectral resolution of the 5 orders range between 84 and 89 km s^{-1} ($R \approx 3400$) and these differ less than 5% for each galaxy. Observations on 2018 October 25 were taken under variable and heavy cloud cover, however, the majority of our sample was observed on 2019 January 25, where cloud cover was light. Individual exposures for all sets of observations were 4 minutes each and were done using the standard ABBA nodding. A telluric standard star, typically of A0 spectral class with measured magnitudes in J, H, and K bands, was observed either directly before or after the target galaxy to correct for the atmospheric absorption features. Typical airmass differences with the target were below 0.10. A summary of the NIR observations is shown in Table 3.1.

Table 3.1: Observation Log

Galaxy	Date (YYYY mm dd)	Redshift	Exp. Time[a]	Slit PA (degrees)	Ext. Ap. (arcsec)	S/N[b]	Airmass	Telluric
SDSS J010005.93-011058.89[c]	2017 10 28	0.05151	8 x 240s	51	1.89	25	1.12	HD18571
SDSS J081145.29+232825.72	2019 01 24	0.01573	12 x 240s	45	1.63	13	1.58	BD-001836
SDSS J084025.54+181858.99	2019 01 24	0.01498	8 x 240s	101	1.63	17	1.34	HD74721
SDSS J084234.50+031930.68[d]	2019 01 24	0.02882	8 x 240s	277	1.63	18	1.28	HD74721
SDSS J090613.76+561015.22[d]	2019 01 24	0.04664	12 x 240s	239	1.51	20	1.31	HD92573
SDDS J095418.15+471725.11[d]	2019 01 24	0.03266	10 x 240s	144	1.63	18	1.18	HD92573
SDSS J100551.18+125740.65[d]	2018 10 24	0.00949	6 x 240s	65	1.90	23	1.60	HD77332
SDSS J100935.66+265648.99[d]	2019 01 24	0.01436	8 x 240s	226	1.63	18	1.03	HD86986
SDSS J144252.78+205451.67	2019 01 24	0.04262	9 x 240s	101	1.52	14	1.24	HD124773

[a] Exposures were typically done in ABBA nodding, [b] Average continuum signal-to-noise ratio (S/N) across all orders, [c] SDSS J0100-0110 was observed with NIRSPEC. All other targets were observed with NIRES, [d] Indicates galaxies with CL detections. See Section 3.3.3

In addition to the Keck NIRES and LRIS observations, follow-up optical integral field unit (IFU) observations with Keck Cosmic Web Imager (KCWI; Morrissey et al., 2018) and Gemini Multi-Object Spectrographs (GMOS; Allington-Smith et al., 2002; Gimeno et al., 2016) were done to obtain high spatial resolution of the outflows. The details of this analysis are discussed in L20.

Four of our targets (J0811+2328, J0906+5610, J0954+4717, and J1005+1257) were observed with the Chandra X-ray Observatory. Baldassare et al. (2017a) report hard X-ray emission that is likely originating from the AGN in J0906+5610 and J0954+4717. Additionally, Wang et al. (2016) provide fluxes, corrected for galactic absorption, for J0811+2328 and J1005+1257, from which we calculated a luminosity using the cosmology listed above. We discuss these results in Section 3.4.1.

The data were reduced using two modified pipelines. The first provided flat fielding and a robust background subtraction by using the techniques described in Kelson (2003) and Becker et al. (2009). In short, this routine maps the 2D science frame and models the sky background before rectification thus reducing the possibility of artifacts appearing due to the binning of sharp features. The sky subtraction attained with this procedure is excellent despite the strong OH lines present in the NIR; the procedure is also quite insensitive to cosmic rays and hot pixels and is reliable regardless of skyline intensity.

Rectification, telluric correction, wavelength calibration, and extraction were all done with a slightly modified version of REDSPEC.[1] Telluric correction was done by dividing by the spectrum of the telluric standard star and multiplying by a blackbody curve of the same temperature. Strong OH skylines were used for wavelength calibration, and the

[1] https://www2.keck.hawaii.edu/inst/nirspec/redspec.html

1D spectra were then median combined. Flux calibration of individual exposures was done using the telluric star and the Spitzer Science Center unit converter[2] to convert the magnitude of the star to the associated flux in that band. A small corrective factor (<5%) was introduced due to the differences between the center NIR bands and that of the wavelength coverage.

3.3 Analysis

3.3.1 Spectral Fitting

3.3.1.1 NIR Fitting

We fit all NIR spectra using EMCEE, an affine invariant Markov Chain Monte Carlo (MCMC) ensemble sampler (Foreman-Mackey et al., 2013). A narrow Gaussian component, along with a second order polynomial for the continuum, were fit simultaneously for each emission line. We determined whether a second Gaussian component was needed to fit the emission lines using the following F-test: $F = (\sigma_{single})^2/(\sigma_{double})^2$, where σ is the standard deviation of the residuals using either single or double Gaussian components. If $F > 2.0$, then adding an extra component is justifiable, and we added a component that is constrained to be broader and lower in amplitude than the first component to avoid degeneracies (see Appendix 6.4 for example figures). Both the narrow and broad components were treated as Gaussians with the amplitude, FWHM, and velocity offset from the rest-frame wavelength as free variables. We list all detected emission line fluxes and widths in Appendix 6.4. Note

[2] http://ssc.spitzer.caltech.edu/warmmission/propkit/pet/magtojy/

that we only report 2σ detections and those with an FWHM greater than the resolution element.

As discussed in Section 3.4.1, we also use NIR absorption features in our analysis. These were also fit with MCMC in a similar fashion, the main difference being the amplitude was restricted to be negative. The fitting was done simultaneously with that of emission lines in order to keep the continuum level consistent across all measurements. Although we ran the F-test as defined above, only one gaussian was needed for all the absorption fits. The widths and depth of the absorption features used in our analysis are also listed in Appendix 6.4.

3.3.1.2 Sloan Digital Sky Survey (SDSS) Fitting

SDSS spectra are available for our entire sample, and these provide full wavelength coverage from 4000-9000 Å, which includes the [O II] $\lambda\lambda$7320, 7330 doublet that is outside the LRIS coverage. The SDSS spectra were fit using Bayesian AGN Decomposition Analysis for SDSS Spectra (BADASS; Sexton et al., 2020)[3] a spectral analysis tool that fits the stellar and Fe II features. Absorption features were fit using the penalized Pixel Fitting (pPXF[4]; Cappellari & Emsellem, 2004) method, and Fe II emission was fit using Fe II templates. All of these components were fit simultaneously, allowing for a detailed and robust analysis of the spectrum.

The code allows the user to test for the presence of outflows by setting various constraints on parameters such as minimum amplitude, minimum width, and velocity offset. The profile of [O III] λ5007 is often used as a tracer of outflows since it is isolated and in

[3] https://github.com/remingtonsexton/BADASS2

[4] https://www-astro.physics.ox.ac.uk/~mxc/software/

a region free of significant absorption. Through [O III] λ5007, we detected strong outflows in the SDSS spectra of six galaxies: J0100-0110, J0811+2328, J0842+0319, J0906+5610, J0954+4717, and J1005+1257 at a $> 95\%$ confidence based on the F-test model comparison included in the code. J1009+2656 is a little more uncertain with a 89% confidence. We do not detect outflows (confidence $< 55\%$) for J0840+1818 and J1442+2054 likely due to the lower resolution of SDSS. These results are consistent with the KCWI results from L20 who found outflows in all targets but J0840+1818 (note that J1442+2054 was not observed with KCWI).

3.3.2 Extinction

We note that L20 reports extinction values calculated from the Hγ/Hβ Balmer decrement. However, for J0100-0110 and J0811+2328, they used Hα/Hβ measurements from SDSS due to weak Hγ emission in their spectra. In addition, they did not observe J1442+2054. We thus opted to use the Hα/Hβ Balmer decrement measured from SDSS for our entire sample.

To quantify the extinction, we used the intrinsic line ratio of Hα/H$\beta = 3.1$, typically used for AGN (eg., Veilleux & Osterbrock, 1987; Osterbrock et al., 1992), and a Cardelli reddening law (Cardelli et al., 1989) with an extinction factor of $R_V = 3.1$. We used the narrow-line flux measurements from the SDSS data (see Section 3.3.1.2), where we have decomposed the Hα and Hβ emission into narrow and broad (outflow) components. For the two galaxies, J0840+1818 and J1442+2054, where no outflow component was detected, we used the full emission line to obtain a flux. These values of the Balmer decrement and $E(B-V)$ for each galaxy are listed in Table 3.2 and all flux values in Appendix 6.4

reflect extinction-corrected fluxes. Note that three galaxies, J0840+1818, J0842+0319, and J0906+5610, have Balmer decrements slightly below the intrinsic ratio so we did not apply any extinction correction to them.

Table 3.2: Measured Extinction Values of the Sample

Galaxy	Hα/Hβ Balmer Decrement	$E(B-V)$
J0100–0110	3.47±0.27	0.115
J0811+2328	3.71±0.34	0.182
J0840+1818	3.06±0.17	0.000
J0842+0319	3.03±0.14	0.000
J0906+5610	2.94±0.18	0.000
J0954+4717	3.25±0.08	0.049
J1005+1257	5.75±0.27	0.624
J1009+2656	3.65±0.10	0.166
J1442+2054	3.69±0.15	0.176

NOTE: An intrinsic ratio of Hα/Hβ = 3.1 and a Cardelli reddening law were used.

Our results are slightly different but generally agree with those calculated by L20. The discrepancies are likely caused by the different line ratios (Hγ/Hβ versus Hα/Hβ) and line profiles used, where we only used the narrow profile while L20 used the full (narrow + broad) profile. When comparing the effect of these two methods, the difference in flux measurements amounts to $< 5\%$ for the majority of our sample. For the rest of this article, we use these extinction-corrected flux values unless otherwise specified.

3.3.3 CL Detections

55% (5/9) of our sample have NIR CL emission within the spectral window of 0.94 — 2.45 μm (see Table 3.1). For a similar spectral window and galaxy type, Sy1 and Sy2, this rate is consistent with others found in the literature: 66% (36 out of 54, Rodríguez-Ardila et al., 2011), 25% (5 out of 20, Mason et al., 2015), and 43% (44 out of 102, Lamperti et al., 2017). Our detections predominately come from sulfur and silicon species: [S VIII] 0.9913 μm, [S IX] 1.2523 μm, [Si X] 1.4305 μm, and [Si VI] 1.9630 μm. We also detect [Ca VIII]

2.3214 μm but it falls within the CO(3-1) absorption band at 2.3226 μm, making their measurements more uncertain. All of the detected NIR CLs are shown in Figure 3.1, where we include our MCMC fits to the emission line profiles. We do not detect other common NIR CLs such as [Fe XIII] 1.0747 μm, [S XI] 1.9196 μm, and [Al IX] 2.0450 μm. The most prominent CL is [Si VI] and is detected in four of the five galaxies with CL detections. This is not surprising since it has a lower ionization potential (IP) level than other CLs and is not near any absorption features. In three of these four galaxies, we find broad [Si VI] emission and thus use a two-component fit to the profile in accordance with the F-test mentioned in Section 3.3.1.1. Details of the multicomponent fits to [Si VI] and plots of the entire spectra are presented in Appendix 6.4.

No NIR CL emission is detected in the other four galaxies. To investigate this, we plotted total [Si VI] flux versus Wide-field Infrared Survey Explorer (WISE) W2 (4.6 μm) flux in Figure 3.2. Note that one galaxy, J0842+0319, has a CL detection, [Ca VIII], but does not show any [Si VI] emission. Upper limit fluxes to the non-[Si VI] detections were calculated by integrating over a Gaussian with a width equaling the resolution element and amplitude equaling the 1σ noise level where [Si VI] should appear. This value was multiplied by three to obtain the 3σ upper limit that is plotted in Figure 3.2. We also plot the AGN sample (black dots) from Müller-Sánchez et al. (2018a), from which we derive the plotted line of best fit. This relation (J. Cann 2021, private communication) provides an expected value for [Si VI] based on W2 flux. Our non-detections lie below most of our [Si VI] measurements, suggesting that deeper observations may be required to detect any CL emission. Further discussion of our non-detections is covered in Section 3.4.1.

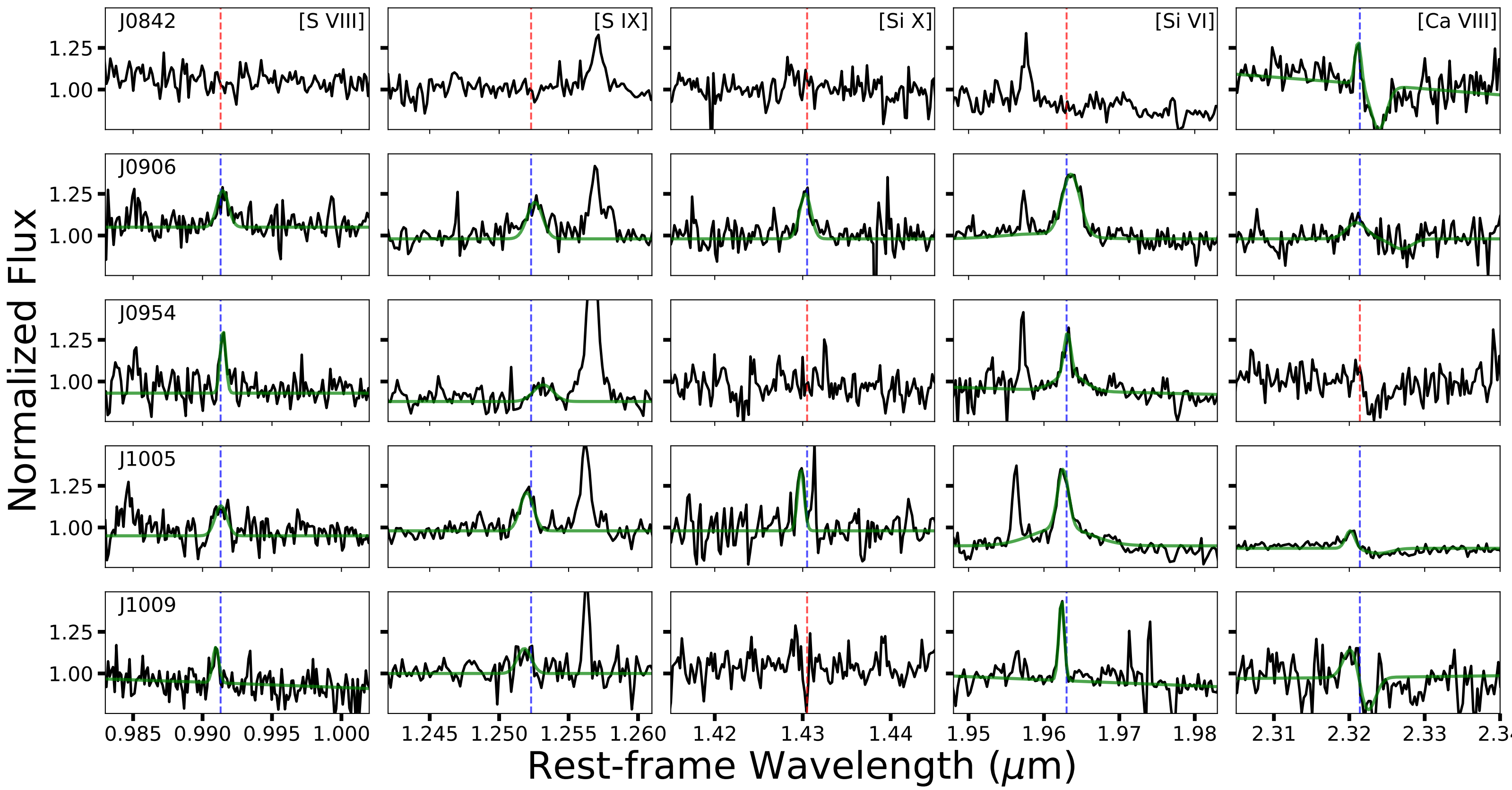

Figure 3.1: Zoom-in plots of the spectral regions around the most prominent NIR CLs, where the flux has been normalized to unity and the systemic redshift was used to shift the spectra to rest-frame wavelength. Dotted blue (detections) and red (non-detections) indicate the rest-frame wavelength of CLs. MCMC fits to the emission and absorption line profiles are shown as solid green lines.

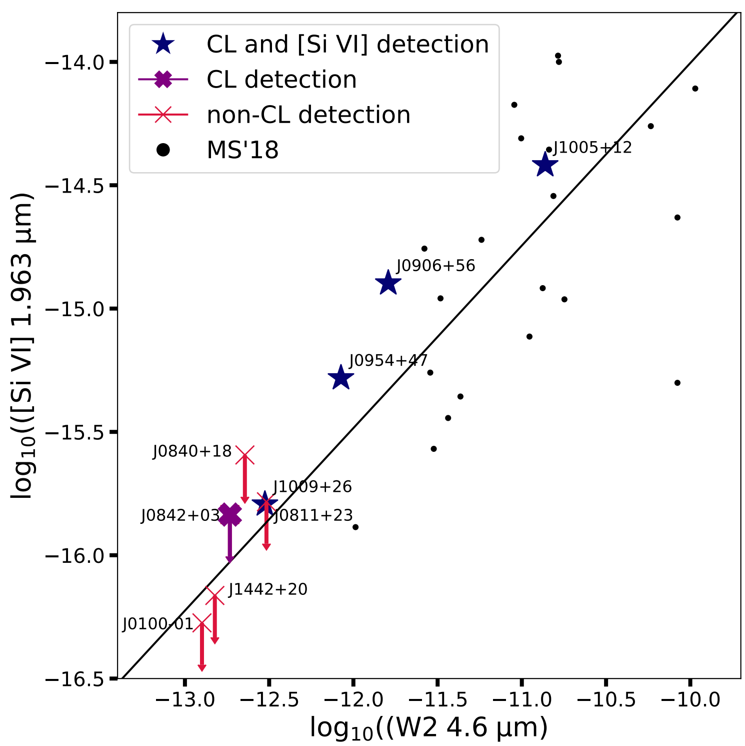

Figure 3.2: [Si VI] flux vs W2 (4.6 μm) flux. Galaxies in our sample with detected [Si VI] emission are shown as blue stars. J0842+0319, the one object with a CL detection but no [Si VI] emission, is shown as a purple cross. Objects without any CL detections are shown as red crosses. For these latter two, the crosses represent 3σ upper limit fluxes to [Si VI]. The solid line is the best-fit line to the data found in Müller-Sánchez et al. (2018a).

The optical data also reveal a number of CLs, particularly in those with NIR CL detections. 55% (5/9) of our sample have strong optical CL emission. The most common detections in our sample include [Ne V] λ3426, [Fe VII] λ6087, and [Fe X] λ6374. Less common lines include [Ne V] λ3346 and [Fe VII] λ5721. Most galaxies that have NIR CL emission also have optical CL emission, and the only exceptions are J0840+1818 and J0842+0319, where the latter only shows NIR CL emission. For J0840+1818, MK19 reported the detection of [Ne V] λ3426 but we do not find any NIR CLs. No other significant detections are seen in the rest of the sample. Additional details for each galaxy are covered in Appendix 6.4. For the remainder of this article, we label galaxies as either having NIR CL emission or not.

3.3.4 AGN Diagnostic Plots

Although there is evidence for AGN activity in our dwarf galaxy sample, including optical BPT/VO87 AGN line ratios, the addition of NIR lines allows us to run additional AGN diagnostics. With the inclusion of [S III] λ9531, we can test our sample with the AGN diagnostics presented in Osterbrock et al. (1992). Specifically, we use the [S III] $\lambda\lambda$9069+9531/Hα versus [S II] $\lambda\lambda$6718+6732/Hα, [S III] $\lambda\lambda$9069+9531/Hα versus [O II] $\lambda\lambda$7320+7330/Hα, and [S II] $\lambda\lambda$6718+6732/Hα versus [O II] $\lambda\lambda$7320+7330/Hα (their Figures 4, 5, and 7). All three of these relations are plotted in Figure 3.3, where we include the AGN and star-forming samples from Osterbrock et al. (1992). We overplot narrow-line fluxes of our sample as stars and exclude the galaxies with no measurable [O II] $\lambda\lambda$7320, 7330. J0100-0110 is also omitted since its [S III] λ9531 is outside the wavelength coverage

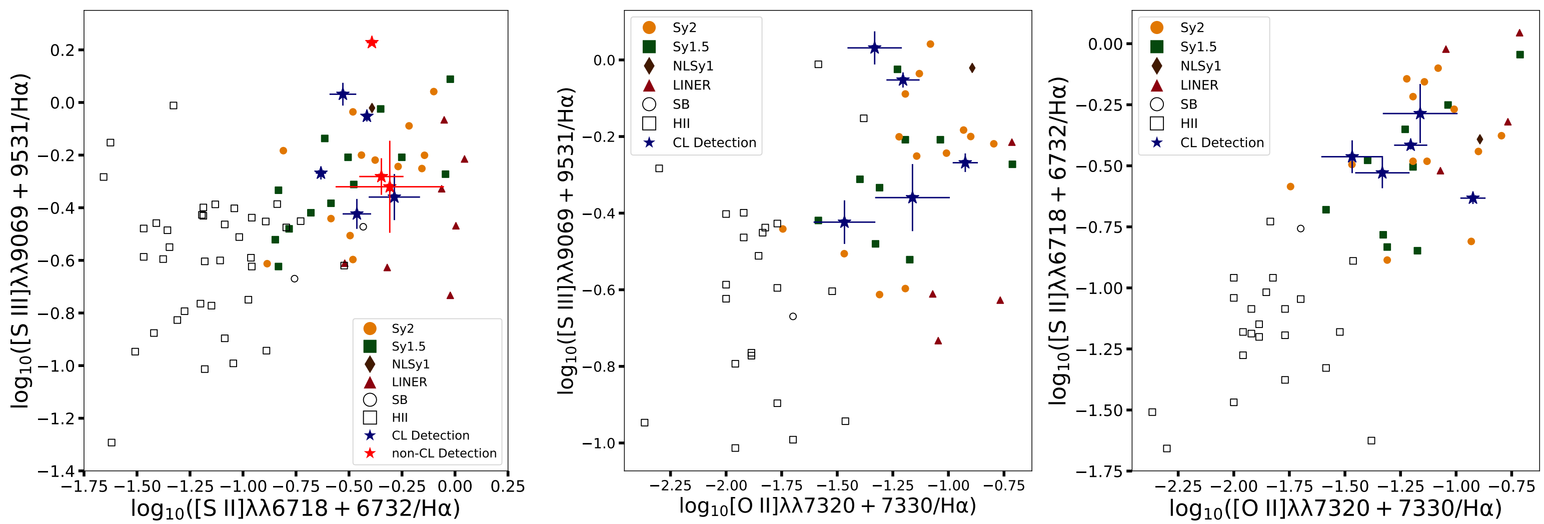

Figure 3.3: AGN diagnostic plots derived by Osterbrock et al. (1992). We plot our sample as blue (CL detection) and red (non-CL detection) stars. Our sample falls within the scatter of other galaxies hosting AGN, further confirming the presence of AGN.

of NIRSPEC. Since [S III] λ9069 is outside the wavelength coverage of NIRES, we use the intrinsic flux ratio of [S III] $\lambda 9531/\lambda 9069 = 2.6$ to obtain flux values for [S III] λ9069.

In all three relations, our dwarf sample falls within the scatter of the AGN sample in Osterbrock et al. (1992). As discussed in Section 3.3.3, not every galaxy in our sample show CLs. To check if this has any effect, we separate our sample into two groups: those with CL emission and those without. We find that they all lie in similar regions and we see no clear distinction between them in all three relations. While no single line ratio can confidently separate AGN activity from star formation, our dwarf sample shows optical and NIR line ratios that, when considered collectively, strongly suggest the presence of AGN.

3.4 Discussion

3.4.1 Detection Rate of CLs

Although CLs are excellent tracers of AGN activity, they do not always appear in AGN spectra and a number of reasons have been proposed to explain this. In general, CL detections decrease with increasing IP and our results agree with this; we do not detect any of the high-IP CLs, [Fe XIII] 1.0747 μm (330.8 eV) and [S XI] 1.9196 μm (447.1 eV). Stellar absorption features can also affect detection rates by attenuating the CL emission profile. Such is the case with [Ca VIII] which falls within the CO (3-1) absorption feature. In addition, Ca and Al species can be affected by metallicity and depletion onto dust. Moreover, telluric absorption from the atmosphere always has to be contended within ground-based observations.

In nearby low-luminosity AGN, circumnuclear stellar populations can dominate the NIR continuum and thus drown out any CL emission. Bright AGN, particularly at high redshift, can also hamper CL emission due to their strong continuum. These effects can be seen in the results of Rodríguez-Ardila et al. (2011) who found that many galaxies with stars contributing ~90% of the continuum do not show CL emission. They also found their CL detection rate decreased by 17% when selecting galaxies with a redshift > 0.05.

Our coverage of J, H, and K bands allows us to estimate the contribution of circumnuclear stellar populations. The CO(6-3) absorption at 1.62 μm can provide an estimate to the flux contribution of red giants to the H-band continuum (Martins et al., 2010), where the continuum level arises due to stellar and AGN contribution. For a population of GKM giants, the typical observed depth of the absorption is ~20% of the continuum (Schinnerer et al., 1998). Our sample ranges from 7% - 14% (median of 11%), suggesting a large contribution to the H-band continuum from red giants, up to 70%. The weighted average of the depth of galaxies with no CL detections is 28% deeper than those with CL emission. One possibility is that a larger population of red giants near the center could be the cause of the deeper absorption and are thus directly increasing the continuum level. Alternatively, a shallower CO absorption may be indicative of a stronger AGN contribution to the continuum, which would likely lead to stronger CL emission that is more easily detectable.

Baldassare et al. (2017a) reported 0.5-7 keV X-ray luminosities for J0906+5610 and J0954+4717, from which we convert to $L_{2-10\mathrm{keV}}$ using the Portable, Interactive Multi-Mission Simulator (PIMMS)[5]. This results in a $L_{2-10\mathrm{keV}}$ of 2.89 $\times$ 10^{40} erg s^{-1} and 6.12 $\times$ 10^{39} erg s^{-1} for J0906+5610 and J0954+4717, respectively. Additionally, using 0.3-8 keV

[5] https://cxc.harvard.edu/toolkit/pimms.jsp

fluxes from Wang et al. (2016), we calculated 2-10 keV luminosities for J0811+2328 (1.33×10^{39} erg s^{-1}) and J1005+1257 (5.20×10^{39} erg s^{-1}). Although J0811+2328 does have the lowest X-ray luminosity, we find no clear distinctions between galaxies with CL detections and those without. We do note, however, that these X-ray luminosities are about two orders of magnitude lower than the $L_{2-10\text{keV}} - L_{\text{W2}}$ relation discussed in Secrest et al. (2015). Indeed, all four targets have $L_{2-10\text{keV}}/L_{\text{W2}} <$ -2.1. Similar low L_X have been reported in low-mass galaxies (Dong et al., 2012; Simmonds et al., 2016; Cann et al., 2020), suggesting obscuration of the X-ray source emission or that AGN in dwarf galaxies are X-ray weak compared to their mid-IR emission.

3.4.2 CL and Outflow Kinematics

Photoionization is widely considered as the main excitation mechanism behind CL emission, although Rodríguez-Ardila et al. (2006) found that their models more precisely matched emission line ratios from their data when shocks were included. If, however, photoionization is the principle excitation mechanism behind CLs, then we expect a correlation between the FWHM and IP. Emission from a high-IP line would suggest that the emitting gas is located closer to the central ionizing source and thus be deeper in the gravitational well, causing a broadening of its emission line profile. Because of their high range of IPs (∼100–500 eV), CLs are ideal in investigating the gas kinematics near the AGN. Indeed, positive correlations between line width and IP have been found in past studies (eg., De Robertis & Osterbrock, 1984; De Robertis & Shaw, 1990; Veilleux, 1991a) for optical high ionization lines. A positive trend has also been found between line width and critical density in these studies. Similar trends between line width and IP for NIR lines have been seen in some galaxies (Rodríguez-Ardila et al., 2002) but larger samples are starting to show more varied CL widths (eg., Rodríguez-Ardila et al., 2011; Villar Martín et al., 2015; Cerqueira-Campos et al., 2020), and in many cases no trends are found at all. Rodríguez-Ardila et al. (2011) found a positive slope up to ∼300 eV, after which the slope turned negative (i.e. higher IP, lower FWHM). They attribute this to the increase in electron density when approaching the central AGN. Due to densities exceeding the critical densities of the high-IP CL ions, these lines may be suppressed. Specifically, collisional de-excitation could reduce emission associated with the broader, high velocity components, thus causing us to only see the narrow emission and explaining the decrease in the FWHM at high IPs.

We run a similar analysis by plotting a narrow-component FWHM versus IP and critical density for the CLs detected in our sample in Figure 3.4. We have also included optical (open circles) and NIR low-ionization lines to draw comparisons (see Table 3.3). In two galaxies, J0906+5610 and J1005+1257, the widths peak around 250 – 300 eV and subsequently decrease, consistent with collisional de-excitation of the broader components of high-IP ions. The CL emission in the other three galaxies have a lower S/N so it is difficult to evaluate any trends. Aside from these low S/N measurements (as indicated by their error bars), these CLs have widths consistent with the lower IP lines. However, some uncertainty may arise from overestimating/underestimating the broad/narrow component of the line profile. For instance, the relatively small width of [Si VI] (166.8 eV) in J0954+4717, where we have added a secondary broad component, could be due to overestimating the broad component. Regardless, our results are consistent with the recent reports finding no clear trends between the FWHM and IP.

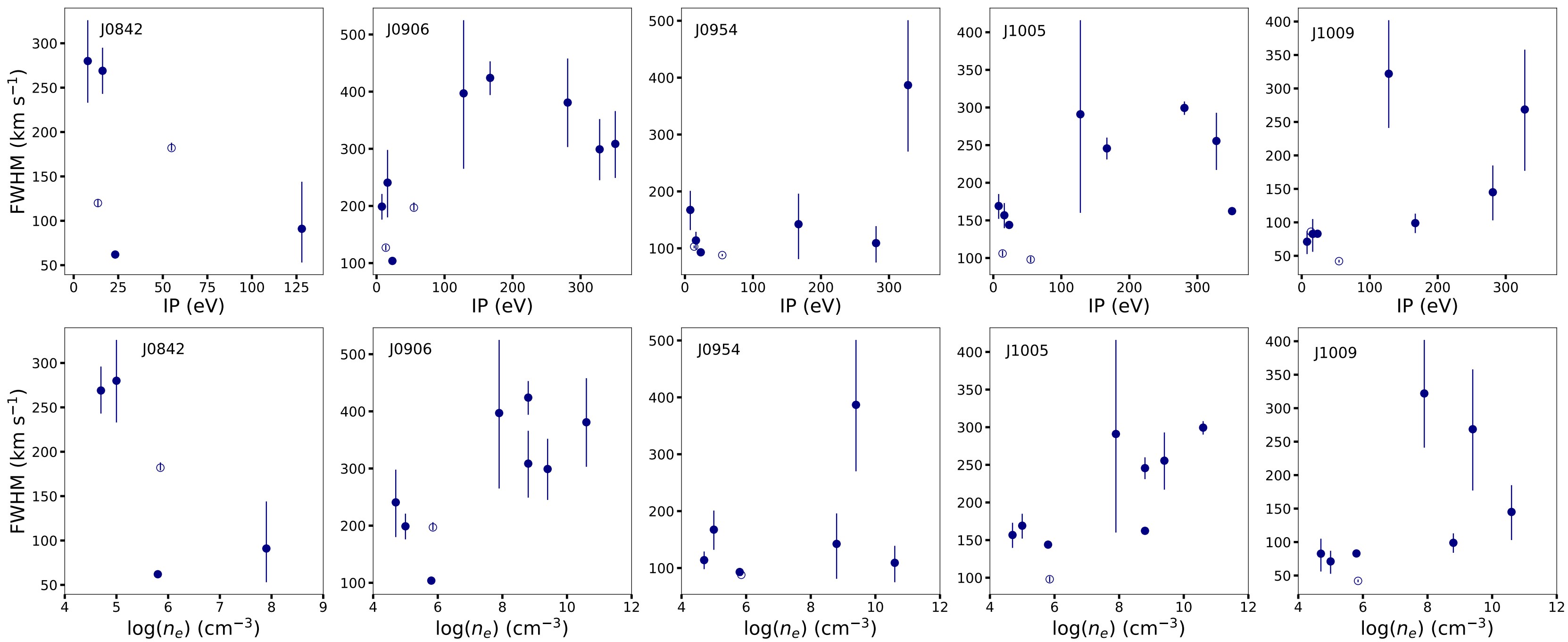

Figure 3.4: FWHM versus IP (top panels) and critical density (bottom panels) for our sample with NIR CL detections. Low-ionization optical emission lines are plotted as open circles, while all NIR emission lines are plotted as filled circles.

Table 3.3: Emission Lines with IP and Critical Densities

Emission Line (μm)	IP (eV)	log(n_e) (cm^{-3})	Emission Line (μm)	IP (eV)	log(n_e) (cm^{-3})
Hα	13.6	—	[Fe II]1.2567	7.9	5.0
[O III]0.5007	54.9	5.85	[Si X]1.4305	351.1	8.8
[S III]0.9531	23.3	5.8	[Fe II]1.6435	16.2	4.7
[S VIII]0.9913	280.9	10.6	[Si VI]1.9630	166.8	8.8
[S IX]1.2523	328.2	9.4	[Ca VIII]2.3214	127.7	7.9

Critical density, defined as the density when the collision rate matches the radiative de-excitation rate, is plotted against the FWHM in the bottom panels of Figure 3.4. Consistent with past works (De Robertis & Osterbrock, 1986; Veilleux, 1991b; Ferguson et al., 1997), we find linear correlation in some galaxies with varying degrees of slope. Regardless, we find a stronger correlation of the FWHM increasing with critical density, consistent with past studies.

Table 3.4 lists the kinematic properties of the narrow and broad (outflow) components of [O III] and [Si VI], where the [O III] values come from L20. The higher spectral resolution of the IFU data of L20 allowed for the decomposition of the emission line profile into two or three components. Generally, the C1 component traces the gas in the narrow-line region, while C2 and C3 represent the broader and bluer components to the multicomponent fit and thus likely trace the outflow. For J0811+2328, only one component (C1) was fit but it is blueshifted relative to the stellar velocity and broader than the stellar velocity dispersion, and thus L20 suggested that it is likely part of the outflow. For v_{50}, the median velocity offset of the profile relative to systemic velocity, we take the minimum values (i.e. maximum blue offset) for [O III].

The velocity of an outflow is often calculated through the use of W_{80}, the width containing 80% of the flux of an emission line (Harrison et al., 2014). For a single Gaussian profile, $W_{80} = 1.09\times$FWHM. To measure W_{80} for [Si VI] , we use the full profile due to the relatively large uncertainties in the broad component. We can define the outflow velocity as

$$v_{\rm out} = -v_{50} + \frac{\rm W_{80}}{2} \tag{3.1}$$

Although C1 likely traces the narrow-line gas, L20 and Manzano-King & Canalizo (2020, hereafter MC20) found cases where outflowing gas can be represented as a single-component profile. For this reason, we include $v_{\rm out}$ calculations for all [O III] components. In addition, for [Si VI] $v_{\rm out}$, we use v_{50} of the full profile if a multicomponent fit was used. This is because of the large uncertainties associated with the broad component fits.

Our data show the outflow velocities seen in [Si VI], measured through either W_{80} or $v_{\rm out}$, are generally faster than those seen in [O III]. The main exception to this are the velocities seen in the C3 components. This is likely due to combining the narrow and broad components of [Si VI] when calculating W_{80} and V_{50}. Using only the broad component, we find velocities to be consistent or higher than those of C3, albeit with much higher uncertainty. This overall trend of higher velocities seen in [Si VI] than in [O III] implies a decelerating outflow, one where a high velocity wind originates near the AGN and slows down as it approaches the outer, lower ionization gas.

We also note that the objects with the fastest outflows and broadest profiles seen in [O III], J0906+5610, J0954+4717, and J1005+1257, have the broadest [Si VI] emission. This is perhaps unsurprising since we are observing the same outflow, just at different locations.

We also list the bolometric AGN luminosities ($L_{\rm AGN}$) in Table 3.4. These values were derived from the observed [O III] λ5007 flux in L20. Empirical bolometric correlation

Table 3.4: Outflow Properties

Galaxy (1)	[O III] Component (2)	[O III] v_{50} (km s^{-1}) (3)	[Si VI] v_{50} (km s^{-1}) (4)	[O III] W_{80} ($v_{\rm out}$) (km s^{-1}) (5)	[Si VI] W_{80} ($v_{\rm out}$) (km s^{-1}) (6)	$\log(L_{\rm [SiVI]})$ (erg s^{-1}) (7)	$\log(L_{\rm AGN})$ (erg s^{-1}) (8)
J0100–0110	Total	-130	—	440 (350)	—	< 38.49	43.3
	C1	-60	—	210 (165)	—	—	
	C2	-240	—	650 (565)	—	—	
J0811+2328	C1	-60	—	220 (170)	—	< 37.95	41.8
J0840+1818	C1	-30	—	130 (95)	—	< 38.10	41.9
J0842+0319	Total	-110	—	700 (460)	—	< 38.42	42.7
	C1	-60	—	220 (170)	—	—	
	C2	-160	—	750 (535)	—	—	
J0906+5610	Total	-50	90, -600	670 (385)	970 (535)	39.79	43.3
	C1	-50	—	140 (120)	—	—	
	C2	30	—	680 (310)	—	—	
	C3	-150	—	1250 (775)	—	—	
J0954+4717	Total	-10	17, 60	530 (275)	650 (300)	39.09	43.6
	C1	0	—	100 (50)	—	—	
	C2	-70	—	430 (285)	—	—	
	C3	-80	—	1100 (630)	—	—	
J1005+1257	Total	-60	-70, -100	680 (400)	1350 (770)	38.87	43.2
	C1	-40	—	120 (100)	—	—	
	C2	-100	—	710 (455)	—	—	
	C3	-200	—	1200 (800)	—	—	
J1009+2656	Total	-50	-100	150 (125)	108 (155)	37.86	42.9
	C1	-30	—	100 (80)	—	—	
	C2	-60	—	480 (300)	—	—	

Columns: (1) Galaxy name. (2) Components of the [O III] fit according to L20. In general, the C3 component traces the faster, broader outflow component while C2 traces the more narrow outflow component. C1 generally traces the gas of the narrow-line region. (3) Minimum values (i.e. maximum blue offset from the systemic velocity) of v_{50} based on [O III] $\lambda5007$ measurements from L20. (4) v_{50} values for [Si VI]. The first value is for the narrow component, followed by the broad component. (5) Maximum W_{80} values based on [O III] $\lambda5007$ measurements from L20. In parentheses are $v_{\rm out}$ values as defined in Equation 3.1. (6) W_{80} of the outflow based on the full [Si VI] profile. $v_{\rm out}$ values are in parentheses. (7) Total luminosity of [Si VI]. Upper limits are included for galaxies without [Si VI] detections (see Section 3.3.3 for details). (8) Extinction-corrected AGN luminosity as derived from [O III] $\lambda5007$ in L20. Extinction values used were derived in this article.

factors from Lamastra et al. (2009) were used: $L_{\rm AGN} = 87\ L_{\rm [O\ III]}$ for $38 < \log(L_{\rm [O\ III]}) < 40$ and $L_{\rm AGN} = 142\ L_{\rm [O\ III]}$ for $40 < \log(L_{\rm [O\ III]}) < 42$. To correct for extinction, we applied the extinction values listed in Table 3.2. We find no strong correlation between AGN luminosity and outflow speeds, but there is a trend for the more luminous AGN to have a higher number and more luminous CL detections. If we assume a simple biconical outflow starting close to the AGN (for a detailed analysis, see Müller-Sánchez et al., 2011), highly ionized gas (i.e. CLs) could more easily be sent out to farther, possibly less obscured regions due to a fast outflow. Although it is difficult to make any firm conclusions due to the CL region being unresolved in our data, it appears that faster outflows may result in stronger and broader CL emission.

3.4.3 Ionization and Origin of the Outflows

In this section, we investigate whether AGN or stellar processes (or both) are the primary source of ionization and the driving mechanism for the outflows.

3.4.3.1 AGN or Stellar Ionization?

The analysis of line ratios by L20 indicates that AGN are the primary source of ionization in our sample. However, they note that ionization from shocks, possibly originating from starburst driven winds (Sharp & Bland-Hawthorn, 2010), cannot be ruled out. To investigate this further, we compare line ratios in our sample to ionization models found in the literature. Riffel et al. (2013) and Colina et al. (2015) plot [Fe II] 1.64 μm/Brγ versus H_2 2.12 μm/Brγ to separate AGN from star-forming samples. However, the five galaxies with obtainable line ratios fall within the overlap between the AGN and SNe-dominated distributions (see Figure 5 from Colina et al., 2015). We instead use the flux ratios of [Si VI]/Brγ and [Fe II] 1.64 μm/Brγ, where [Fe II] is a sensitive indicator of shocks (U et al., 2013) and Brγ serves as an indicator of stellar activity and the ionizing radiation field. We compare these ratios to the AGN ionization models from Groves et al. (2004a,b) and shock models from Allen et al. (2008). We extracted these models from the IDL Tool for Emission-line Ratio Analysis (ITERA) library (Groves & Allen, 2010) and plotted them in Figure 3.5. The shock model (Figure 3.5, left) takes into account both the shocked gas and precursor gas, which lies ahead of the shock front. Quick inspection of shock-only model (not plotted) shows a shift toward higher [Fe II]/Brγ ratios, farther away from our measured line ratios. We thus focus our analysis on the shock + precursor model (hereafter simply shock model) since the individual regions cannot be resolved in our data. Free parameters for the shock model include the shock velocity $v_{\rm shock}$ (10–1000 km s^{-1}) and the magnetic field parameter $B/n^{1/2}$ (10^{-4}–10 μG cm$^{3/2}$), where B is the transverse magnetic field. The AGN model free parameters include the power-law index α and the ionization parameter U, where $U \equiv n_{\rm ion}/n_{\rm e}$, where $n_{\rm ion}$ is the density of the ionizing photons, and $n_{\rm e}$ is the electron density. The model uses a simple power law, $F_\nu \propto \nu^\alpha$, where 5eV $< \nu <$ 1000eV (see Groves et al., 2004a,b, for further details).

To estimate the CL gas density, Landt et al. (2015a,b) used line ratios of the [Fe VII] $\lambda\lambda\lambda$3759, 5159, 6087 optical CLs. Although we do not detect all these lines in our optical data, some targets do have two [Fe VII] emission lines that are measurable. For these targets, we calculated an upper limit flux to the third [Fe VII] line and obtained a rough estimate of the gas density. These values are consistent with a density of 1000 cm^{-3}. In addition, L20

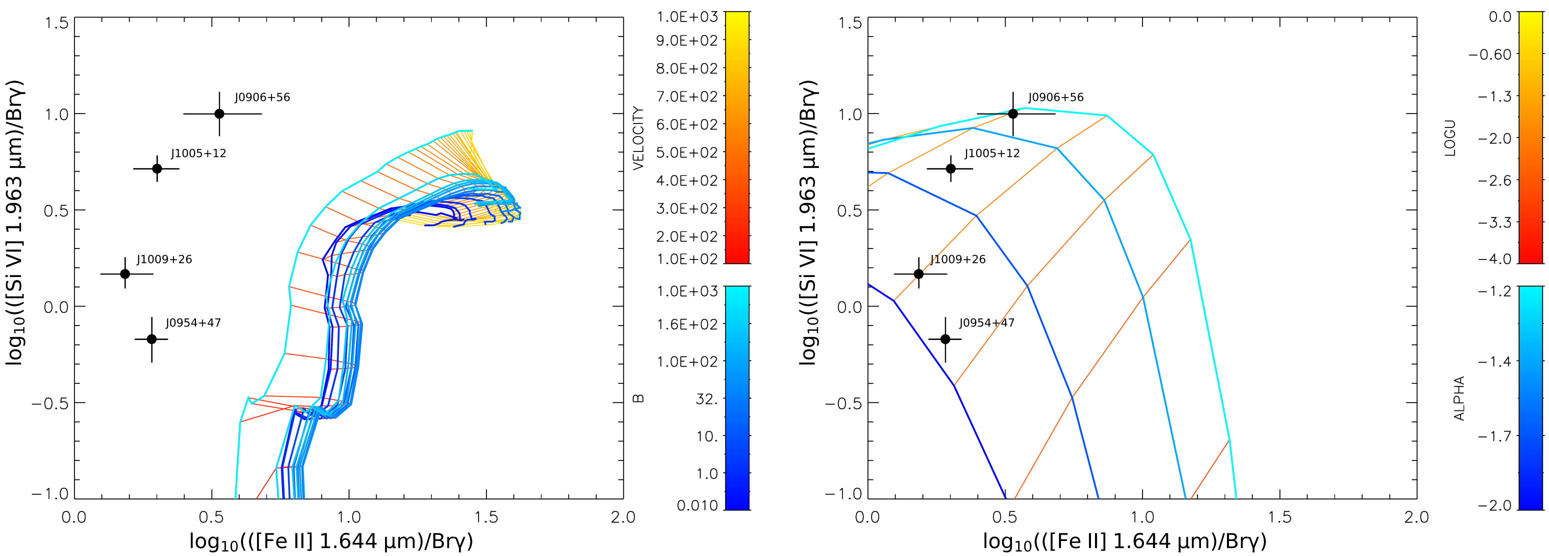

Figure 3.5: Log_{10}([Si VI]/Brγ) versus $\log_{10}$(Fe II/Brγ) for (a) shock + precursor and (b) AGN model plots. Free parameters for the shock + precursor grid lines are the shock velocity v_{shock} and magnetic field parameter B. Free parameters for the AGN grid lines are the power-law index α and the ionization parameter U. The four galaxies with detected [Si VI] emission are plotted as black circles with error bars. Metallicity was set to solar and a gas density of $n = 1000$ cm^{-3} was assumed.

used the S II $\lambda6716$/S II $\lambda6731$ line ratio (eg., Sanders et al., 2016) and obtained values of $\sim$ 500 cm^{-3} for most of their sample. They thus use a density of 1000 cm^{-3} in their models. Therefore, in both of our models, we use a gas density of 1000 cm^{-3}. Lastly, metallicity was set to solar.

We use the total flux for each emission line and plot the ratios over the shock model (Figure 3.5, left) and AGN model (Figure 3.5, right). It is clear that the line ratios are well within the AGN model parameters (-2.0 $\lesssim \alpha \lesssim$ -1.2 and -3.3 $\lesssim \log(U) \lesssim$ -2.0). As for the shock models, the line ratios are offset by more than 0.5 dex and all have systematically larger [Fe II]/Brγ ratios. In order to match the measured data, it appears a relatively large magnetic parameter ($> 10^3$) is required. Thus, it is likely that AGN are the dominant ionizing source in our sample, though a small contribution from shocks cannot be formally ruled out.

3.4.3.2 AGN or Stellar Driven Winds?

The matter of identifying the driving force behind the outflows is a difficult but important issue to investigate. Outflowing winds are often cited coming from either AGN or starburst activity (eg., Fabian, 2012; Rupke, 2018; Veilleux et al., 2020), though distinguishing between the two is often difficult. L20 investigated the energies associated with the outflows in our sample and found that the AGN are more than powerful enough to drive them. However, they found that typical core-collapse SNe can also provide the necessary energy output needed.

One avenue of checking the likelihood of starburst driven winds in our sample is to estimate the age of a stellar population. The CN absorption features at 1.1 μm have been shown to serve as an indicator of an intermediate-aged stellar population (Maraston, 2005; Riffel et al., 2007). This band most notably arises from carbon stars where there is an excess of carbon that is not bonded in CO molecules. To form a carbon star, a third "dredge-up" during the thermally pulsing asymptotic giant branch (TP-AGB) is necessary and this constrains the stellar population age to be within 0.3 – 2 Gyr. Thus, CN absorption would identify a younger to intermediate-aged stellar population and signify an occurrence of starburst activity.

The absence of CN absorption, however, may not necessarily imply an absence of a young to intermediate-aged stellar population. Riffel et al. (2009) and Martins et al. (2013) reported cases with no CN absorption but with known intermediate populations and vice versa. But as they pointed out, this is not to say that CN does not trace an intermediate population. Overlap with strong emission from He I 1.08 μm and Paγ can partially or fully obstruct the CN absorption. Telluric absorption, particularly in galaxies with low redshift ($z < 0.01$), may also interfere with CN detection. Even with proper correction from a telluric standard, the residuals can have substantial effects on the S/N on the CN features.

Visual inspection of our spectra shows no interference from strong emission lines but we do find significant telluric absorption in the region of CN in two cases (see Appendix 6.4 for more details). For the rest, this lack of CN absorption would indicate that much of the CO absorption comes from older red giants (see Section 3.4.1). This is also consistent with the stellar population age estimates of at least several Gyrs modeled from optical LRIS spectra (Manzano King, 2020). This apparent deficit of young stars would suggest a lack of starburst that could drive the outflows we see, making the outflows more likely to be driven by AGN.

3.5 Conclusion

We have presented Keck NIR spectroscopy of a sample of dwarf galaxies with strong evidence of AGN activity and have shown the outflows detected are likely AGN driven. Eight galaxies were observed with Keck NIRES, providing full wavelength coverage from 0.9 – 2.4 μm, and one galaxy with Keck NIRSPEC, with wavelength coverage from 1.97 – 2.39 μm. The main results are summarized below.

- NIR CLs (IP $>$ 100 eV) are detected in 5/9 (55%) galaxies in our sample, consistent with detection rates found in larger mass studies. Due to their high ionization potentials, CL emission is highly indicative of AGN activity. Coupled with optical and other NIR AGN diagnostics, there is strong evidence for AGN activity in these dwarf galaxies.
- For the four galaxies without NIR CL emission, we suspect a strong contribution from a population of red giants that could be dominating the continuum level and hamper any weak CL emission. The deeper CO(6-3) absorption at 1.62 μm in these galaxies indicates a larger population of old stars. Alternatively, the deeper CO absorption may be indicative of weaker AGN that would result in more elusive CL emission.
- No clear trends are found between the widths of the CLs and their IPs. Two galaxies show a decrease in width after peaking around 250 – 300 eV. As noted in previous works, this is likely due to collisional de-excitation caused by the high density environments

near the central ionizing source. In addition, we see a positive trend between the FWHM and the critical densities in these two galaxies. The other galaxies show CL widths that are consistent with lower IP lines and their widths are not as tightly correlated with critical densities.

- The outflow velocities measured from [Si VI] emission are generally faster than those measured from [O III]. This indicates the presence of a decelerating outflow. We also find that the galaxies with the highest [Si VI] luminosity also have the fastest outflows measured in [O III].

- Examination of ionization models reveals that NIR emission line ratios of our sample are more consistent with AGN models than with shock + precursor models. This indicates that AGN are the main ionizing source, though a smaller contribution from shocks cannot be formally dismissed.

- The lack of CN absorption at 1.1 μm suggests a lack of young/intermediate (0.3 – 2.0 Gyr) circumnuclear stars in our sample. This goes against the scenario where the outflows are produced by starburst activity, suggesting AGN as the main driving force of the outflows.

Chapter 4

A Near-Infrared look at AGN Feedback in Bulgeless Galaxies

4.1 Introduction

The relations between the properties of galaxies and their SMBHs have become a vital part of understanding galaxy evolution. Well-known correlations such as the $M_{\rm BH}$-σ (eg., Ferrarese & Merritt, 2000; Gebhardt et al., 2000; McConnell & Ma, 2013; Sexton et al., 2019) and the $M_{\rm BH}$ - $M_{\rm bulge}$, (eg., Marconi & Hunt, 2003; Häring & Rix, 2004) have shown that SMBHs and their host galaxies likely co-evolve with each other. In the larger mass regime, galaxy mergers are often regarded as the driving mechanism behind this co-evolution. This is because galaxy mergers are able to disrupt the angular momentum of the baryonic matter rotating in the disk. This redistribution culminates not only in a galactic bulge forming but can also result in gas being funneled toward the central BH. It is through these processes that BHs are believed to reach supermassive sizes.

This paradigm of BH growth accompanying bulge growth raises an important question regarding galaxies that have not had merger events in their history. While simulations have shown that galaxies can regrow their disks after a merger event (eg., Hopkins et al., 2009), a small bulge component can still form after a minor merger. Thus, it is likely that a galaxy with no bulge has had a merger-free history. These systems are of particular interest since their BHs have grown through secular processes. As such, their number density and occupation fraction can provide important constraints on the BH seed population. Indeed, a number of studies have investigated BHs residing in bulgeless host galaxies. Simmons et al. (2017) report BH mass estimates for a large sample of Type 1 targets and find they fall within the scatter of the $M_{\rm BH}$ - $M_{\rm stellar}$ relation. Likewise, Bohn et al. (2020) come to a similar conclusion for a Type 2 AGN through the use of near-infrared (NIR) observations. Adding to this fact that some simulations suggest mergers do not induce a significant amount of SMBH growth (Martin et al., 2018; McAlpine et al., 2020), secular processes may play a more significant role in BH growth than originally thought.

The addition of SMBHs in bulgeless galaxies necessitates a closer look at these systems. Understanding the dynamics between these BHs and their hosts is crucial to putting constraints on secular growth processes and BH-galaxy co-evolution. An important aspect of this co-evolution is the impact of AGN feedback. Outflows from AGN are believed to regulate and suppress star formation, leading their hosts to the well-defined red sequence (King & Pounds, 2015; Rupke et al., 2017). However, only a limited number of AGN-driven outflows have been observed in bulgeless galaxies (Smethurst et al., 2019, 2021). In order to place more stringent constraints and assess the impact of secularly grown BHs, a larger sample size is needed.

A central issue when identifying AGN in bulgeless galaxies is confirming the true morphology of the host. While estimates to $M_{\rm BH}$ may be relatively easy to obtain in Type 1 AGN through the use of emission from the broad-line region and the virial method, the reliability of bulge-disk decompositions could be compromised due to the bright AGN being in our direct line of sight. Consequently, a small bulge component could be hidden. Type 2 AGN benefit from more robust bulge-disk decompositions but the lack of broad emission lines, particularly in optical wavelengths, makes it difficult to obtain robust $M_{\rm BH}$ estimates. An added limitation is that bulgeless galaxies can have high levels of dust obscuration, making AGN identification difficult and thus optical selection incomplete (Satyapal et al., 2014).

A number of methods have been suggested to identify and confirm the presence of obscured AGN, including spectropolarimetry (Antonucci & Miller, 1985; Zakamska et al., 2005) and infrared observations (eg., Veilleux et al., 1997; Satyapal et al., 2007, 2008, 2014; Lamperti et al., 2017; Cann et al., 2020), where extinction is less severe in the latter. The NIR spectral region hosts a number of emission lines used for AGN analysis. Below z $\sim$ 0.3, these include coronal lines (CLs), forbidden transitions from highly ionized (>100 eV) species that are highly indicative of AGN activity, and H I recombination lines that can trace the broad-line gas. Additionally, due to the characteristically redder mid-infrared (MIR) colors of obscured AGN (Stern et al., 2012), MIR color cuts can be used to separate optically hidden

AGN from star forming galaxies. Indeed, the *Wide-field Infrared Survey Explorer* (*WISE*; Wright et al. 2010) and *Spitzer Space Telescope* have been used to separate AGN from star-forming galaxies, as shown by the AGN demarcation box in Jarrett et al. (2011). Recent follow-up work has indicated that this color-cut could identify a new group of obscured AGN that would complement existing optical data and provide a more representative picture of the AGN population (Satyapal et al., 2014, hereafter S14). However, confirmation that these galaxies do indeed host AGN is needed since contamination from star formation cannot be dismissed.

To this end, in this article we aim to confirm the presence of AGN activity in the sample of MIR-selected bulgeless galaxies presented in S14. In Section 4.2, we provide details of the sample, observations, and data reduction. Fitting of the spectra and calculations of the extinction levels and star-formation rates (SFRs) are covered in Section 4.3. In Section 4.4, we use a number of AGN indicators, including CLs, broad-line emission, and AGN diagnostic diagrams, to confirm the presence of AGN activity. Section 4.5 analyzes outflow kinematics and energies. We report virial BH mass estimates in Section 4.6 and compare these to known scaling relations. Lastly, in Section 4.7, we analyze rotational gas velocities and discuss the affects of AGN feedback in our sample. We adopt a standard ΛCDM cosmology with $H_0 = 70$ km s^{-1} Mpc^{-1}, $\Omega_M = 0.3$, and $\Omega_\Lambda = 0.7$.

4.2 Data and Observations

4.2.1 Sample Selection

Our sample of bulgeless galaxies come from those presented in S14. To summarize their selection process, they drew from Simard et al. (2011), where bulge-disk decompositions were performed on SDSS imaging. To obtain a bulgeless subsample, S14 selected galaxies with a bulge-to-total light ratio of 0.00 in both r and g-bands. SDSS spectroscopy was also required for proper redshift estimates, which resulted in a bulgeless sample of ∼18,000 galaxies (see Figure 4.1). They subsequently cross-matched this bulgeless subsample with the *WISE* all-sky data release catalog[1] in order to obtain $W1$ (3.4 μm), $W2$ (4.6 μm), and $W3$ (12 μm) bands. Utilizing the AGN demarcation zone as defined in Jarrett et al. (2011), they then formed a sample of 30 AGN candidates, all of which have $W1 - W2 > 0.7$. These candidates form the basis of our sample. In total, we obtained NIR spectroscopy of 13 of these 30 targets during our assigned telescope time, and these 13 targets span the full range of WISE colors presented in S14. In Figure 4.1, we plot these targets on the Baldwin, Phillips & Terlevich (BPT; Baldwin et al., 1981) diagram and the WISE color-cut diagram as presented in Jarrett et al. (2011). Hereafter, targets with at least one AGN indicator will be represented as a blue symbol while those whose emission is dominated by stellar processes will be shown as red symbols (see Section 4.4 for details). The redshift range of our sample is from 0.05 to 0.24, with a median of 0.117. The stellar masses range from 10.0 - 11.1 $M_\odot$ and were obtained from Chang et al. (2015), who performed SED fitting on optical and IR

[1] https://wise2.ipac.caltech.edu/docs/release/allsky/

data. Comparing to the bulgeless sample as a whole, our galaxies tend to be on the higher mass end.

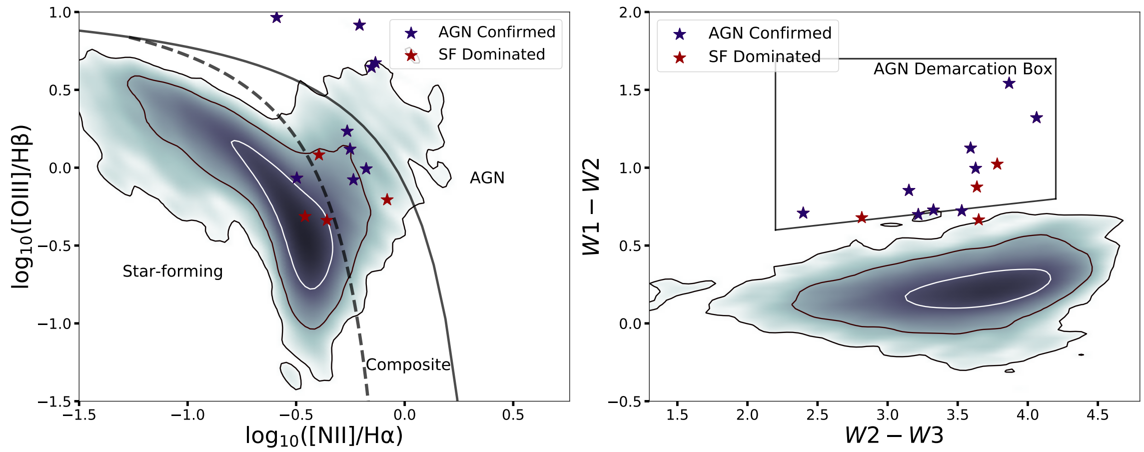

Figure 4.1: (*left*) *BPT* diagram with diagnostic lines from Kewley et al. (2001) and Kauffmann et al. (2003). The full bulgeless sample from Simard et al. (2011) are represented as contours (1σ, 2σ, and 3σ levels). Galaxies covered in this study are represented as stars, with those confirmed as AGN with at least one indicator are shown as blue stars (see Section 4.4). Targets whose emission is dominated by stellar processes are shown red stars. (*right*) *WISE* color diagram with the AGN demarcation box from Jarrett et al. (2011).

4.2.2 Observations and Data Reduction

Our Keck NIR spectroscopy was obtained throughout the 2018 and 2019 semesters using two instruments: NIRSPEC (McLean et al., 1998) and NIRES (Wilson et al., 2004). NIRSPEC is a NIR echelle spectrograph on Keck II with a wavelength coverage of 0.9 — 5.5 μm. The NIRSPEC-7 filter was used in low-resolution mode ($42'' \times 0.76''$ slit) and the cross-dispersion angle was set to 35.38°. This resulted in a wavelength coverage of 1.98 — 2.40 μm. An average spectral resolution of 197 km s^{-1} ($R \approx 1500$) was measured at 2.20 μm. All NIRSPEC observations were done on 2018-03-05 under mostly clear conditions and the seeing was typically $\sim 0.6''$.

NIRES is a NIR echelette spectrograph with a $18'' \times 0.55''$ slit and wavelength coverage of 0.94 — 2.45 μm, split into five orders. There is a small gap in coverage between 1.85 and 1.88 μm, but this is a region of low atmospheric transmission. The average spectral resolution of the five orders ranges between 85 — 95 km s^{-1} (R $\approx$ 3300). The majority of observations were done under mostly clear conditions (∼0.5" seeing); only J0122+0100 and J0333+0107 were observed under poor weather.

Individual exposures for all sets of observations were four minutes each and were done using the standard ABBA nodding. A telluric standard star, typically of A0 spectral class with measured magnitudes in J, H, and K-bands, was observed either directly before or after the target galaxy to correct for atmospheric absorption features. Typical airmass differences with the target were below 0.10. Details of the observations are summarized in Table 4.1 and PanSTARR (Chambers et al., 2016) images of our sample are shown in Figure 4.2. For J1036+0221 we provide *HST* imaging. Slit positions and contours showing the isophotes are also provided.

A similar reduction process was performed for both the NIRSPEC and NIRES data. However, the differences in the two instruments necessitated slight modifications in the two pipelines used. The first algorithm provided flat fielding and a robust background subtraction by using techniques described in Kelson (2003) and Becker et al. (2009). In short, this routine maps the 2D science frame and models the sky background before rectification, thus reducing the possibility of artifacts appearing due to the binning of sharp features. The sky subtraction attained with this procedure is excellent, despite the strong OH lines

Table 4.1: Observation Log

Galaxy (SDSS Name)	Date (YYYY-mm-dd)	Instrument	Redshift	Scale (kpc/arcsec)	Exp. Time[a]	Slit PA (degrees)	Aperture (arcsec)	Airmass
J012218.11+010025.76	2018-09-20	NIRES	0.05546	1.08	4 x 240s[b]	100, 183	1.92	1.25
J033331.86+010716.92	2018-10-24	NIRES	0.17755	3.00	2 x 240s	0	1.49	1.15
J075039.97+292845.75	2018-03-05	NIRSPEC	0.14701	2.57	12 x 240s	68	1.46	1.11
J085153.64+392611.76[c]	2019-03-25	NIRES	0.12958	2.31	5 x 240s	94	1.33	1.07
J085236.35+292853.20	2019-03-25	NIRES	0.07866	1.49	8 x 240s	162	1.34	1.04
J092907.78+002637.29	2019-03-25	NIRES	0.11732	2.12	8 x 240s	56.5	1.51	1.09
J103222.94+361727.91	2018-03-25	NIRES	0.23578	3.74	4 x 240s	131	1.18	1.05
J103631.88+022144.10	2018-03-05	NIRSPEC	0.05026	0.98	4 x 240s	42.5	1.68	1.05
J122809.19+581431.40[c]	2019-01-24	NIRES	0.10982	2.00	12 x 240s	333	1.34	1.28
J123304.57+002347.11	2019-03-25	NIRES	0.06917	1.32	8 x 240s	75.5	1.33	1.06
J132647.54+101436.53	2019-03-05	NIRSPEC	0.08943	1.67	6 x 240s	161.5	1.57	1.02
J133341.72+653619.16	2019-03-25	NIRES	0.15756	2.72	4 x 240s[d]	123, 44	1.34	1.43
J155409.08+145703.59	2019-03-25	NIRES	0.13666	2.42	8 x 240s	121	1.33	1.02

[a] Exposures were typically done in ABBA nodding, [b] Four exposures were taken for both the east and west targets, [c] J0851 and J1228 were also observed with NIRSPEC on 2018-03-05, [d] Four exposures were taken for each position angle

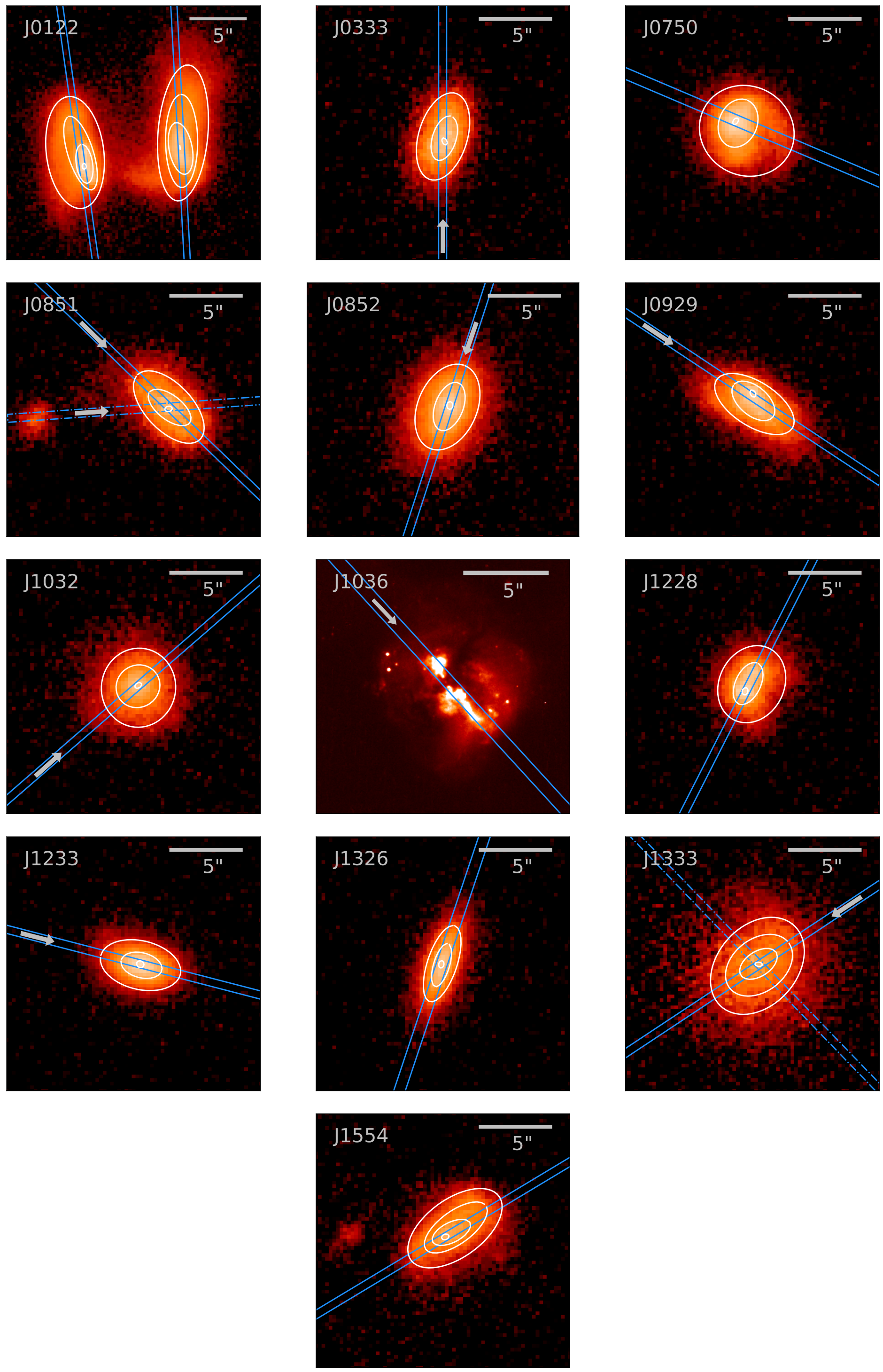

Figure 4.2: PanSTARRS (and *HST* for J1036+0221) image cut-outs of our sample. The galaxy short-name and 5" scale are listed at the top. The blue lines indicate the placement of the slit. For galaxies where we see gas rotation, we place arrows pointing in the direction from blueshifted to redshifted velocities (see Fig. 4.6). Lastly, the white contours show the isophotes of each target.

present in the NIR; the procedure is also quite insensitive to cosmic rays and hot pixels, and is reliable regardless of skyline intensity.

Rectification, telluric correction, wavelength calibration, and extraction were all done with a slightly modified version of REDSPEC.[2] Telluric correction was done by dividing by the spectrum of the telluric standard star and multiplying by a blackbody curve of the same temperature. Strong OH skylines were used for wavelength calibration and the 1D spectra were then median combined. Flux calibration of individual exposures was done using the telluric star and the Spitzer Science Center unit converter[3] to convert the magnitude of the star to the associated flux in that band. In addition to correcting for Galactic reddening, a small corrective factor (<5%) was introduced due to the differences between the center NIR bands and that of the wavelength coverage.

4.3 Analysis

4.3.1 Spectral Fitting

4.3.1.1 NIR Fitting

We fit all NIR spectra using EMCEE, an affine invariant Markov Chain Monte Carlo (MCMC) ensemble sampler (Foreman-Mackey et al., 2013). A narrow Gaussian component, along with a low order (≤ 7) Legendre polynomial for the continuum, were fit simultaneously for each emission line. We determined whether a second Gaussian component was needed to fit the emission lines using the following F-test: $F = (\sigma_{single})^2/(\sigma_{double})^2$, where σ is the

[2] https://www2.keck.hawaii.edu/inst/nirspec/redspec.html

[3] https://irsa.ipac.caltech.edu/data/SPITZER/docs/dataanalysistools/tools/pet/magtojy/index.html

standard deviation of the residuals using either single or double Gaussian components. If $F > 2.0$, then adding an extra component is justifiable and we added a component that is constrained to be broader and lower in amplitude than the first component to avoid degeneracies. Both the narrow and broad components were treated as free Gaussians with amplitude, full-width half-maximum (FWHM), and velocity offset from rest-frame wavelength as free variables. The fluxes of all NIR emission lines detected at $> 3\sigma$ level are listed in Table 6.12 of Appendix 6.5.

Various absorption features were also fit in a similar fashion. The fitting was done simultaneously with that of emission lines in order to keep the continuum level consistent across all measurements. Although we ran the F-test as defined above, only one gaussian was needed for all the absorption fits.

4.3.1.2 SDSS Fitting

As noted in Section 4.2.1, SDSS spectra are available for our entire sample and these provide full wavelength coverage from 4000 Å to 9000 Å. The SDSS spectra were fit using Bayesian AGN Decomposition Analysis for SDSS Spectra (BADASS,[4] Sexton et al., 2020), a spectral analysis tool that provides comprehensive fits to SDSS spectra. Absorption features were fit using the penalized Pixel Fitting (pPXF[5]; Cappellari & Emsellem, 2004). All components were fit simultaneously, allowing for a detailed and robust analysis of the spectrum.

A key feature of BADASS is that it allows the user to test for the presence of outflows in the form of broad components of emission lines by setting various constraints

[4] https://github.com/remingtonsexton/BADASS2
[5] https://www-astro.physics.ox.ac.uk/~mxc/software/

on parameters such as amplitude, line width, and velocity offset. [O III] λ5007 is often used as a tracer of ionized gas outflows in the optical since it is isolated (i.e., no risk of blending with broad-lines) and in a region free of significant stellar absorption. Evidence of outflow activity is generally believed to manifest itself as a broad flux excess, typically seen as an asymmetric wing that is blue-shifted relative to the rest-wavelength emission (Woo et al., 2016; Manzano-King et al., 2019). In addition to velocity shifts, widths of a few hundred to thousands of km s^{-1} have been reported in optical and NIR data (eg., Rodríguez-Ardila et al., 2006; Müller-Sánchez et al., 2011; Harrison et al., 2014; McElroy et al., 2015). These fast outflows can be seen on kiloparsec (kpc) scales (eg., Cresci et al., 2015; Rupke et al., 2017; Müller-Sánchez et al., 2018b; Liu et al., 2020) and could potentially be key contributors to suppressing star formation (Fabian, 2012; King & Pounds, 2015; Costa et al., 2020). If the outflows are driven by the AGN, then this BH feedback may lead to well-known scaling relations, such as the $M_{\rm BH}$-σ. In addition, CL emission has often been observed with strong outflows (Müller-Sánchez et al., 2011; Bohn et al., 2021), making outflow detections a unique point of interest when searching for and confirming AGN activity using CLs.

Through SDSS spectral fitting of [O III], we detect strong outflows in four galaxies: J0852+2928, J0929+0026, J1233+0023, and J1333+6536 at a $>$ 95% confidence based on the F-test model comparison included in the code. This confidence cut results in a stringent selection criteria, having only selected blue-shifted components with FWHM $>$ 400 km s^{-1} and amplitudes higher than 3σ of the noise level. In these successful cases, the outflow parameters determined in [O III] are used to constrain the outflow components found in other strong emission lines (Hα, Hβ, etc.). These constraints include a fixed amplitude ratio ($A_{outflow}/A_{core}$), FWHM, and velocity offset. This is done since blending, particularly between Hα and [N II], can be problematic in identifying and fitting outflow components.

A non-outflow detection worthy of note is J1036+0221 since it does show a high confidence, ∼90%. However, it is likely undergoing a merger event and a number of mechanisms could be causing the broader [O III] profile, such as superposition of two nuclei or tidal disruptions caused by the merger. Due to these uncertainties, we do not include J1036+0221 in our outflow analysis.

We do not detect outflows in the rest of our sample, where they all have low confidence levels ($< 65\%$). However, this does not rule out the presence of outflows in these galaxies. As Sexton et al. (2020) points out, signal-to-noise (S/N) can play an important role in detecting outflows. Additionally, spatial and spectral resolution can affect detection, as shown in Manzano-King et al. (2019), where nine outflows are detected in Keck LRIS but only two of these are detected in SDSS. Kadir et al. (*in prep.*) also find that high extinction can inhibit outflow detection. Indeed, galaxies in our sample where we do see outflows tend to have lower levels of extinction (see Tables 4.2). Thus the detection rate of outflows in our sample should be taken as a lower limit.

4.3.2 Extinction

To quantify the extinction, we used the intrinsic line ratio of Hα/Hβ = 3.1, typically used for AGN (eg., Veilleux & Osterbrock, 1987; Osterbrock et al., 1992), and a Cardelli reddening law (Cardelli et al., 1989) with an extinction factor of $R_V = 3.1$. We used the narrow-line flux measurements from the SDSS data (see Section 4.3.1.2), where we have

Table 4.2: Summary of Galaxy Properties

Galaxy (1)	W1-W2 (2)	M_{BH} ($M_\odot$) (3)	E(B-V) (4)	SFR ($M_\odot$ yr^{-1}) (5)	CL? (6)	Outflow? (7)	Overmass. DMH? (8)	BPT AGN? (9)	OVT '92 AGN? (10)	AGN Evidence? (11)
J0122ne	—	—	0.00	<0.40	—	—	—	—	✓	✓
J0122se	1.60	—	$0.80^{+0.11}_{-0.11}$	<3.47	✓[a]	—	—	—	—	✓[a]
J0122w	—	—	$1.82^{+0.07}_{-0.07}$	<8.57	—	—	—	—	—	—
J0333	0.87	—	$1.38^{+0.28}_{-0.31}$	$4.00^{+2.16}_{-1.50}$	—	—	—	—	—	—
J0750	1.00	—	$1.27^{+0.49}_{-0.57}$	$3.28^{+3.59}_{-1.91}$	—	—	—	—	—	—
J0851	0.71	6.78±0.14	$0.66^{+0.36}_{-0.40}$	$0.36^{+0.32}_{-0.19}$	—	—	—	—	✓	✓
J0852	0.76	—	0.00	<0.18	✓	✓	✓	✓	✓	✓
J0929	0.85	—	$1.28^{+0.08}_{-0.08}$	—	✓*	✓	—	✓	✓	✓
J1032	0.74	—	$0.80^{+0.25}_{-0.27}$	$2.74^{+1.33}_{-0.96}$	—	—	—	—	—	—
J1036	1.30	—	$2.17^{+0.13}_{-0.13}$	<6.53	✓[a]	—	—	—	✓	✓
J1228	0.72	6.80±0.32	$2.50^{+1.25}_{-2.12}$	<3.19	—	—	—	✓	✓	✓
J1233	0.98	—	$0.81^{+0.30}_{-0.34}$	<0.46	✓	✓	✓	—	—	✓
J1326	0.73	—	$2.88^{+1.08}_{-1.67}$	<2.04	—	—	—	—	—	—
J1333	0.73	—	$0.18^{+0.33}_{-0.18}$	—	✓*	✓	—	✓	✓	✓
J1554	1.14	—	$1.59^{+0.47}_{-0.55}$	$1.18^{+1.69}_{-0.78}$	✓	✓	—	—	—	✓

[a] NIR CLs detected in Satyapal et al. (2017)

Columns: (1) Galaxy name. (2) *WISE W1-W2* magnitude. (3) BH mass as determined in Section 4.4.2 and 4.6. (4) Extinction based on the Hα/Hβ Balmer decrement. (5) Star-formation rate based on [O II] (Kewley et al., 2004). We omit values if [Ne V] is detected and place upper limits if the presence of [Ne V] cannot be determined. (6) Presence of NIR CLs. An asterisk (*) signifies optical CLs are detected. (7) Evidence of outflows. (8) Evidence of an overmassive DMH. (9) Galaxy falls within the AGN region of the BPT diagram. (10) Galaxy falls within the AGN region of at least one of the diagnostic diagrams in Osterbrock et al. (1992). (11) Any indication of AGN activity.

decomposed the Hα and Hβ emission into narrow and broad (outflow) components. For galaxies where no broad component is detected, we used the full emission line to obtain a flux. The value of E(B-V) for each galaxy is listed in Table 4.2. Note that two galaxies, J0122+0100 (Northeast region) and J0852+2928, have Balmer decrements below the intrinsic ratio so we did not apply any extinction correction to them. For the rest of this article, we use extinction corrected flux values unless otherwise specified.

4.3.3 Star-formation Rates

We estimated the SFRs of our sample through the use of the [O II] λ3727 doublet indicator presented in Kewley et al. (2004). We list these measurements in Table 4.2. While [O II] is useful for calculating SFRs, complications can arise if an AGN is present and can ionize the [O II] gas in the extended emission line regions. This is mainly seen in cases where AGN ionization reaches beyond the NLR. In order to identify whether an AGN could be ionizing [O II], the CL [Ne V] λ3426 is often used (Maddox, 2018). As such, the presence of [Ne V] would indicate contamination of the [O II] emission from the AGN and thus it cannot be used as a SF indicator.

We find [Ne V] emission in two targets, J0929 and J1333, and thus omit their values from Table 4.2. For targets where we cannot confirm the absence of [Ne V] (mainly due to the wavelength coverage of SDSS), we report their SFRs as upper limits.

4.4 Evidence of AGN Activity

4.4.1 Coronal Line Detections

An effective method of identifying AGN activity is through the detection of CLs. This is because CLs have higher ionization potentials than what is typically produced by stellar processes. A total of seven out of the 13 bulgeless galaxies in our sample (54%) show CLs. We detect [Si VI] 1.9630 μm in the NIR spectra of five targets in our sample (see Figure 4.3 and Table 4.2; fluxes listed in Table 6.12). In addition, Satyapal et al. (2017) report the detection of [Si VI] in J0122+0100(SE) and [Si X] 1.4305 μm in J1036+0221. They used a wider slit with a different placement for J0122+0100(SE), which may explain why we did not observe [Si VI] in our NIRES spectrum. We fit their [Si VI] emission line and include it in the following analysis. For J1036+0221, we do not detect [Si X] since it is outside our selected wavelength coverage for NIRSPEC. Additional details on these two targets are included in Appendix 6.6. While we include the detection of CLs in these targets in our overall statistics, we only investigate the kinematics and other properties of the CLs observed in our NIRSPEC and NIRES spectra.

Inspection of the SDSS spectra reveals optical CL emission in only two targets, J0929+0026 and J1333+6536; these are marked with an asterisk in Table 4.2. We detect [Ne V] λ3426 in both of these galaxies, in addition to [Si VI] mentioned above. Environmental effects have been shown to inhibit optical CL detection. As suggested by comparisons between NIR and optical spectra of Sy1 and Sy2, and the reduced strength of CLs in the latter (Nagao et al., 2000; Gelbord et al., 2009), the dusty torus likely lowers the detection

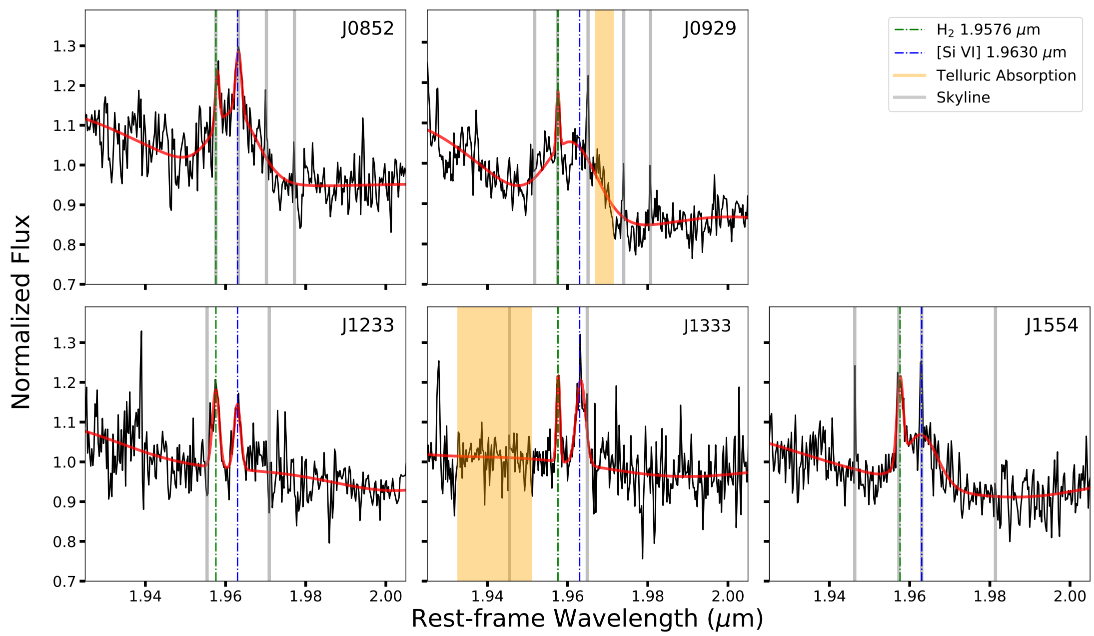

Figure 4.3: Zoom-in plots of [Si VI] emission and the surrounding region. The best-fit line from EMCEE is plotted in red and the dash-dot green and blue lines denote the rest-frame location of H_2 1.957 μm and [Si VI], respectively. Grey lines and shaded yellow regions signify the location of skylines and telluric absorption that are in close proximity to [Si VI].

frequency of such lines. This, along with the high extinction levels seen in our sample, could explain the low detection rate of optical CLs in our sample.

It is not surprising that [Si VI] is the only prominent NIR CL we detect. It has a lower ionization potential (IP = 167 eV) than other CLs and benefits from being located in a region free of stellar absorption. Indeed, other studies find [Si VI] to be the most common CL, with Rodríguez-Ardila et al. (2011) finding it in 56% of their sample and Lamperti et al. (2017) finding it in 33% of theirs.

The 54% CL detection rate in our sample should be regarded as a lower limit, as there are several factors that can affect the detectability of CLs. For instance, faint lines can be easily diluted by the underlying continuum and/or they can fall below detection limits. To obtain estimates for the expected flux values for the [Si VI] lines that we do not detect, we make use of the relation reported by Cann et al. (2021) between *WISE* $W2$ (4.6 μm) flux and [Si VI] flux. We plot this relation in Figure 4.4. Upper limit fluxes to the non-[Si VI] detections were calculated by integrating over a Gaussian with a width equaling the resolution element and the amplitude equaling the 1σ noise level where [Si VI] should appear. This value was multiplied by three to obtain the 3σ upper limit that is plotted. We include the AGN sample (black dots) from Müller-Sánchez et al. (2018a), from which the plotted line of best fit is derived in order to show the scatter in the relation. Figure 4.4 shows that the majority of our non-detections (crosses) are indeed the targets with the lowest expected fluxes.

It is worthwhile to note the [Si VI] emission in J1233+0023. It has the lowest luminosity and spatial extent of [Si VI] in our sample. As such, this faint emission is

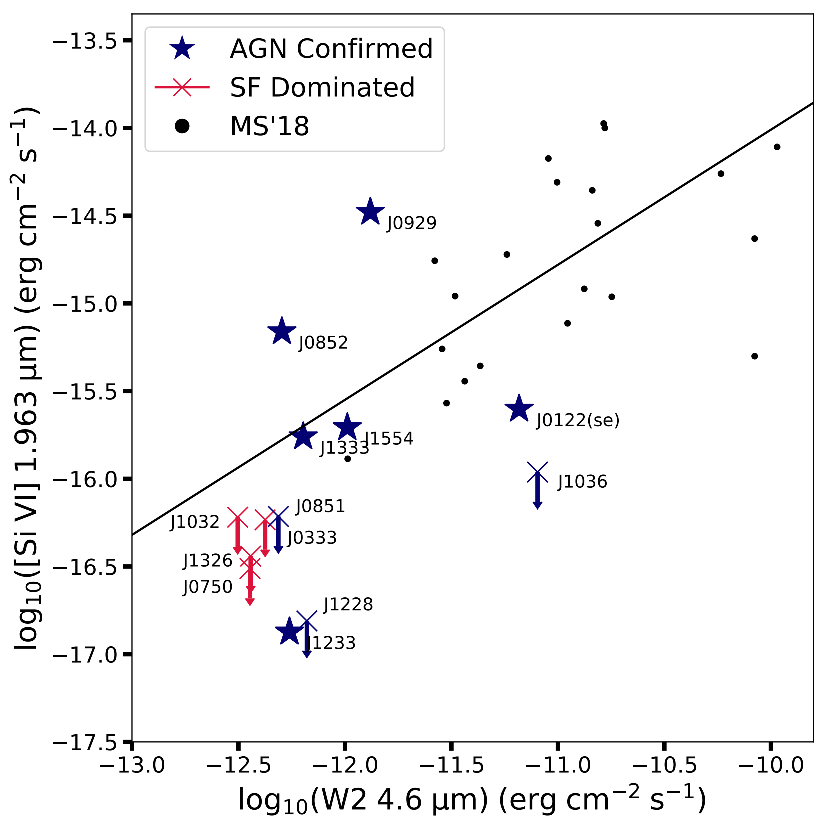

Figure 4.4: [Si VI] flux vs W2 (4.6 μm) flux. [Si VI] detections are represented as blue stars. Note that we include the [Si VI] detection from S14. Crosses represent targets with no [Si VI] emission detected. The arrows indicate these are 3σ upper limit fluxes to [Si VI]. Blue symbols represent galaxies with AGN activity while red represents galaxies with stellar emission dominating the spectra. The solid line is the best-fit line to the data found in Müller-Sánchez et al. (2018a).

susceptible to dilution from other sources of emission. Indeed, we see no trace of [Si VI] emission if we use the extraction aperture listed in Table 4.1. Only when a smaller aperture that sampled the very center was used could we confirm the presence of [Si VI]. Although this is the sole case in our sample, caution should be taken when using large apertures.

The majority of our non-detections lie below and to the left of the [Si VI] measurements, suggesting that deeper observations are likely required to detect any emission. Inspection of the SFRs (see Section 4.3.3) shows that galaxies with no [Si VI] emission have SFRs about an order of magnitude higher than those with [Si VI] emission. Visual inspection of some of these targets show that they are likely involved in an on-going merger event. In such an event, tidal forces could funnel gas towards the central regions and fuel star formation. Although these results are not indicative of starburst activity, they do suggest an increase of SF that could increase the continuum level and make weak emission lines, such as CLs, more difficult to detect.

4.4.2 NIR Broad Emission from Broad-Line Region

The NIR spectral region includes several important recombination lines, including Paα and Paβ. Like Hα and Hβ, these Paschen lines can be used to trace the broad-line gas from an AGN. They also benefit from being less affected by dust obscuration. As such, the 'hidden' broad-line (HBL) region can arise in cases where broad emission is present in the NIR but obscured in the optical, betraying the presence of an AGN.

Inspection of the NIR spectra reveals hidden broad-line emission (Paα) in two of our targets, J0851+3926 (see also Bohn et al., 2020) and J1228+5814. Our detection rate

(15%) is similar to that of other studies such as Lamperti et al. (2017), who find HBLs in 10% of their Sy2 sample, and Veilleux et al. (1997) who find HBLs in 27% of theirs.

Observations for both of our targets with HBL were conducted on two separate nights, approximately one year apart. While broad emission is certainly indicative of AGN activity, Baldassare et al. (2016) and other follow-up studies of AGN candidates with broad emission have shown that supernovae (SNe) and other stellar activity can produce similar broad profiles. Type II SNe (Pritchard et al., 2012) and luminous blue variables (Smith et al., 2011) are known to produce broad recombination lines up to thousands of km s^{-1}. If the broad Paα observed were powered by SNe, the broad emission would have persisted for more than a year, and this in turn would indicate that the SNe would likely be Type II-P. Using this time scale, we would expect to see other NIR SN features such as O I, Mg I, and Ca I (e.g., Rho et al., 2018). However, we do not see any of these features in either of our NIR observations. Additionally, we would expect the line profiles to change significantly over this time (Rho et al., 2018) but our width measurements are consistent with each other: 1490 and 1360 km s^{-1} for J0851+3926, and 1640 and 1840 km s^{-1} for J1228+5814.

Another potential origin of a broad-line could be powerful outflows driven by star formation. Broad, symmetric components to emission lines are observed in some starburst galaxies (Martin, 1998; Westmoquette et al., 2008; Manzano-King et al., 2019). However, these galaxies show broad emission in other lines, particularly in [O III]λ5007. As mentioned in Section 4.3.1.2, we utilized BADASS to check for the presence of any outflow component in the optical spectra. All reasonable criteria came back negative for outflows in these two targets, thus it is unlikely that outflows are affecting the broad-line emission. We conclude that the most likely origin of the observed broad Paα is the broad-line region of an AGN, providing strong evidence that these two targets have AGN activity.

4.4.3 NIR Diagnostic Diagrams

Optical line ratios, such as the BPT diagram shown in Figure 4.1, indicate AGN activity in only four of the 13 targets in our sample. With the inclusion of NIR data, we can use additional AGN diagnostics that are more insensitive to dust obscuration. Osterbrock et al. (1992) use where Hα, [S II] $\lambda\lambda$6718+6732, [O II] $\lambda\lambda$7320+7330, and [S III] $\lambda\lambda$9069+9531 fluxes to detect AGN activity. We plot these line ratio diagrams in Figure 4.5, where we include the AGN and star-forming samples from Osterbrock et al. (1992). We overplot narrow-line fluxes of our sample (star symbols) and exclude the galaxies with no measurable [O II] or [S III] emission. In cases where [S III] λ9531 is measurable but [S III] λ9069 is not, we use the intrinsic flux ratio of [S III] $\lambda9531/\lambda9069 = 2.6$ to obtain flux values for the latter. Lastly, for J0122+0100, SDSS provides three sets of spectra: one for the west galaxy and two for the east galaxy, a north and south component separated by about 2". We include all three of these in Figure 4.5.

Most galaxies with CLs and HBLs fall within the scatter of the other AGN. As for the rest of the sample, the line ratios of J1036+0221 and J0122+0100(ne) place them within the AGN region of Figure 4.5. J0122+0100(w+se) do not fall consistently in the same region but they generally do not fall within the scatter of the star-forming galaxies. In addition to the NIR line ratios presented here, Satyapal et al. (2017) report *Chandra* and *XMM-Newton* X-ray observations for J1036+0221 and J0122+0100(w+se). The observed luminosities of

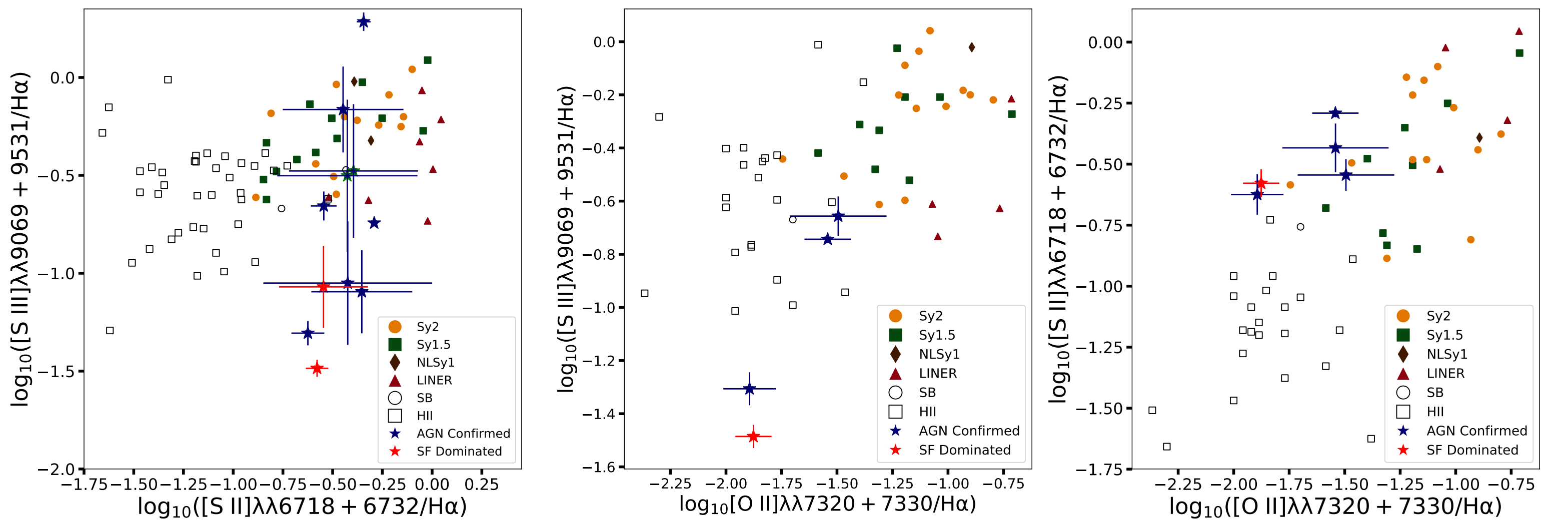

Figure 4.5: AGN diagnostic plots derived by Osterbrock et al. (1992), where we include their sample. We plot our sample as blue and red stars, where blue represents galaxies with clear signatures of AGN activity and red represents galaxies whose emission is dominated by stellar processes.

all three sources are significantly higher (>7.5 times greater) than the luminosities expected from X-ray binaries. This, along with CLs detected by Satyapal et al. (2017), indicate the presence of AGN in these galaxies.

While no single line ratio can confidently separate AGN from stellar ionization, our bulgeless sample shows optical and NIR line ratios that, when considered collectively, strongly suggest the presence of AGN. This lack of strong stellar activity not only supports ionization from the AGN, but also indicates the outflows detected (discussed in Section 4.5) are of AGN origin.

4.4.4 Summary of AGN Indicators

In the sections above, we discussed confirming AGN in our sample using a variety of methods, including CL detections, broad-line emission, and AGN diagnostic diagrams. Of our sample, we report CL detection in 54%, hidden broad-lines in 15%, and NIR AGN line ratios in 54%. Collectively, this results in 69% (9/13) unique targets with at least one indication of AGN activity. Indeed, our results show that MIR color are an effective tool to select AGN, with over half of the confirmations coming from galaxies that would not have been classified as AGN from optical studies. For those targets for which we find no clear indication of AGN, we find they have generally twice the extinction levels and an order of magnitude higher SFRs than those for which we find evidence of AGN in the NIR. If these galaxies do indeed have an AGN, then they are likely heavily obscured or the emission from stellar processes is dominating the optical and NIR spectra. For the rest of the article, we will refer to galaxies with confirmed signatures of AGN activity as 'AGN Confirmed' and those without as 'SF Dominated'.

4.5 Outflows

In Section 4.3.1, we reported the detection of fast outflows in [O III] in four of the galaxies in our sample and in Section 4.4.1 we identified an additional target with an outflow in [Si VI]. Thus, five out of the nine (54%) AGN-confirmed galaxies show fast outflows, whereas none of the SF-dominated galaxies do. This is consistent with other studies that find a higher incidence of outflows in AGN hosts as compared to star forming galaxies (e.g. Cicone et al., 2014; Harrison et al., 2016; Concas et al., 2017; Leung et al., 2019; Lutz et al., 2020; Avery et al., 2021, W. Matzko et al. in preparation).

In this section, we report an observed strong correlation between the detection of outflows and that of CLs. We also present the outflow kinematics and estimated energies, and provide supporting evidence that outflows in bulgeless galaxies may be intrinsically different than those in galaxies with merger dominated histories.

4.5.1 Outflows and Coronal Lines

CLs are often associated with outflows, where the blue-shifted emission profiles of CLs have been attributed to outflow kinematics (Rodríguez-Ardila et al., 2006; Müller-Sánchez et al., 2011). Indeed, Liu et al. (2020) and Bohn et al. (2021) find that the galaxies with the strongest and fastest outflows have the strongest and most numerous CL detections. Here, we report similar findings, where all the galaxies with detectable outflows also have CLs. We note that while J1554+1457 has NIR CL emission with a fast outflow, it does not show any evidence of an outflow in its optical spectrum. A possible reason for this is the high level of extinction, E(B-V) = 1.59, that could be inhibiting the detection of a small outflow component in the SDSS spectra.

A number of scenarios could give rise to the connection between outflows and CLs that we observe. One such case is if the AGN is responsible for both producing the outflow and ionizing the CL gas: CL emission requires a highly energetic radiative source, and this source in turn could drive a highly energetic outflow. Other scenarios are more causal. Relativistic outflowing winds have been known to produce strong shocks in the interstellar medium (ISM) surrounding the AGN (Fabian, 2012; King & Pounds, 2015; Harrison et al., 2018). These shocks can heat gas, which in turn can provide at least some of the necessary ionization for CL emission. Although photoionization is believed to be the main mechanism to produce CL emission, some studies have shown that the addition of energy input from shocks can help the observed line ratios better replicate those predicted by ionization models (Rodríguez-Ardila et al., 2006; Müller-Sánchez et al., 2011). Lastly, the outflowing winds may be simply removing the obscuring medium, allowing for a more clear view of the CL region.

4.5.2 Kinematics of Outflows and Coronal Lines

Due to the connection between CLs and outflows, CLs have been used to trace the kinematics of outflows (Rodríguez-Ardila et al., 2006; Müller-Sánchez et al., 2011). In Table 4.3, we list gas kinematics measured from the [O III] and [Si VI] lines. To calculate the velocity of an outflow, we can utilize two values: v_{50} and W_{80} (Harrison et al., 2014). Here, v_{50} is the velocity offset of the outflow component from the core component while W_{80} is the width containing 80% of the line flux. For a single Gaussian profile, $W_{80} = 1.09\times$FWHM.

In the cases where only one [Si VI] component was fit, we use the full emission profile and set v_{50} to be the offset from rest-wavelength. Using these parameters, we can define the outflow velocity as follows

$$v_{\mathrm{out}} = -v_{50} + \frac{\mathrm{W}_{80}}{2} \tag{4.1}$$

A general trend seen here is the outflow velocities associated with CLs (mean ∼890 km s^{-1}) tend to be higher than those seen in the narrow-line region (mean ∼480 km s^{-1}). Since the CL region is believed to lie closer to the SMBH, this trend would suggest a decelerating outflow. Here, a high velocity wind would originate near the AGN and would slow down as it encounters the surrounding ISM.

We additionally report the spatial extent of [Si VI] emission and bolometric AGN luminosities in Table 4.3. We derived the AGN luminositites from the measured [O III] λ5007 flux. Empirical bolometric correlation factors from Lamastra et al. (2009) were used: $L_{\mathrm{AGN}} = 87\ L_{[\mathrm{O\ III}]}$ for $38 < \log(L_{[\mathrm{O\ III}]}) < 40$ and $L_{\mathrm{AGN}} = 142\ L_{[\mathrm{O\ III}]}$ for $40 < \log(L_{[\mathrm{O\ III}]}) < 42$. We find stronger [Si VI] emission in galaxies with more luminous AGN, further suggesting that the AGN is the ionizing source for the CL emission in this sample. Due to the strong correlation between CLs and outflows, this would also indicate that the AGN are also responsible for driving the outflows. Although we do not find a strong correlation between outflow velocities and AGN luminosity (Pearson coefficient = -0.37), we do see a correlation with the spatial extent of [Si VI] and outflow speed as calculated through [Si VI] (Pearson coefficient = 0.86). A likely cause of this is that the faster and more energetic outflows are less inhibited by the ISM and can more easily clear out the surrounding gas.

Alternatively, the faster, more extended outflows could be expanding into regions that are less dense or obscured.

4.5.3 Outflow Energies

The energies of the outflows can be calculated assuming a time averaged, thin-shell, free wind model (Shih & Rupke, 2010). However, the outflows in the SDSS data are not spatially resolved and thus some simplifying assumptions need to be made on the size of the outflows. From Rupke et al. (2005), the outflow energies can be calculated using the following simplified equation:

$$\frac{dE}{dt} = \frac{1}{2}(v_{50}^2 + 3\sigma^2)\frac{dM}{dt} \tag{4.2}$$

where $\sigma = W_{80}/2.563$. The outflow mass rate, dM/dt, can be expressed as:

$$\frac{dM}{dt} = \frac{M_{out} v_{out}}{R_{out}} \tag{4.3}$$

where M_{out} is the total mass of the outflowing gas and R_{out} is the upper limit on the radius of the outflow. From Osterbrock & Ferland (2006), M_{out} can be calculated from:

$$\frac{M_{out}}{M_\odot} = 4.48\left(\frac{L_{H\alpha}}{10^{35}\ \mathrm{erg\ s^{-1}}}\right)\left(\frac{< n_e >}{1000\ \mathrm{cm^{-3}}}\right)^{-1} \tag{4.4}$$

where we assume Case B recombination with $T = 10^4$ K. Here, $L_{H\alpha}$ is the extinction corrected luminosity of the outflow component of Hα and n_e is the electron density, which we estimated using the [S II] $\lambda6716/\lambda6731$ relation (Sanders et al., 2016). The uncertainties

Table 4.3: Outflow and [Si VI] Properties

Galaxy (1)	[O III] v_{50} (km s^{-1}) (2)	[Si VI] v_{50} (km s^{-1}) (3)	[O III] W_{80} ($v_{\rm out}$) (km s^{-1}) (4)	[Si VI] W_{80} ($v_{\rm out}$) (km s^{-1}) (5)	[Si VI] Radius (kpc) (6)	$\log(L_{\rm [SiVI]})$ (erg s^{-1}) (7)	$\log(L_{\rm AGN})$ (erg s^{-1}) (8)
SDSS J0852+2928	-260±20	-250±30	1120±40 (820±40)	2130±220 (1315±140)	0.8	$39.97^{+0.06}_{-0.08}$	$42.81^{+0.09}_{-0.12}$
SDDS J0929+0026	-40±5	-510±40	700±20 (390±15)	2510±440 (1765±260)	1.4	$41.07^{+0.10}_{-0.12}$	$44.65^{+0.06}_{-0.07}$
SDSS J1233+0023	-120±20	-70±5	510±60 (375±50)	310±70 (225±40)	0.3	$38.19^{+0.07}_{-0.09}$	$42.78^{+0.16}_{-0.25}$
SDSS J1333+6536	-110±15	-40±5	470±50 (345±40)	490±50 (285±30)	0.4	$39.98^{+0.04}_{-0.04}$	$43.19^{+0.16}_{-0.27}$
SDSS J1554+1457	—	-20±15	—	1720±210 (880±120)	1.2	$39.99^{+0.07}_{-0.08}$	$42.96^{+0.26}_{-0.35}$

Columns: (1) Galaxy name. (2) Velocity offset of the [O III] λ5007 outflow component from the core component. (3) Velocity offset of [Si VI] from rest-wavelength. (4) W_{80} values of the [O III] λ5007 outflow component. In parentheses are $v_{\rm out}$ values as defined in Equation 4.1. (5) Same as the previous column but for [Si VI]. (6) Spatial extension of [Si VI]. (7) Extinction-corrected [Si VI] luminosities. (8) Extinction-corrected AGN luminosities.

in n_e are relatively large, and are incorporated into the errors listed in Table 4.4. Lastly, upper limits to R_{out} were calculated using the R_{out} - $L_{[OIII]}$ relation derived in Kang & Woo (2018). We multiply these values by a factor of 2 to account for the far side of the outflow that is blocked by the galaxy. Lower limits for the mass and energy rates of the outflows are listed in Table 4.4.

Table 4.4: Energetics of the Outflows

Galaxy	$\log(M_{out})$ ($M_\odot$)	$\log(dM/dt)$ ($M_\odot$ yr^{-1})	$\log(dE/dt)$ (erg s^{-1})
J0852+2928	5.7±0.21	>-0.6	>40.8
J0929+0026	7.6±0.25	>0.6	>41.4
J1223+0023	6.1±0.24	>-0.5	>40.2
J1333+6536	4.3±0.19	>-2.4	>38.2

Columns: (1) Galaxy name. (2) Total mass of the outflow. (3) Mass outflow rate. (4) Kinetic energy outflow rate.

Comparing the mass and mass outflow rates of our galaxies to those of the disk-dominated sample from Smethurst et al. (2019), we find that the outflows presented here have comparable values. Smethurst et al. (2019) find that the outflow rates of disk-dominated galaxies are lower than those measured in galaxies with merger dominated histories. They attribute this discrepancy to differences in black hole spin and accretion geometries that are a result of accretion by secular processes. As such, this would suggest that outflows in bulgeless galaxies may be intrinsically different than those found in galaxies that have had a significant merger history.

4.6 Scaling Relations

Since two of our targets show broad emission from the BLR, we can estimate their BH masses through the virial relation:

$$M_{\rm BH} = f\frac{V^2R}{G} \tag{4.5}$$

where f is the virial coefficient; V is the velocity of the broad-line gas; R is the distance from the broad emission gas to the central continuum source which can be estimated using relations derived from reverberation mapping; and G is the gravitational constant. The FWHM of the broad emission line can be used for the value of V, and the value of R is estimated empirically using the optical luminosity of the AGN as a proxy (Kaspi et al., 2005; Bentz et al., 2013).

The BH mass was obtained following the estimators presented by Kim et al. (2018), where they adopted the virial factor log $f = 0.05 \pm 0.12$ derived by Woo et al. (2015). From Kim et al. (2018), their Equation 10,

$$\frac{M}{M_\odot} = 10^{7.07\pm0.04}\left(\frac{L_{\rm Pa\alpha}}{10^{42}\ {\rm erg\ s^{-1}}}\right)^{0.49\pm0.06}\left(\frac{{\rm FWHM_{Pa\alpha}}}{10^3\ {\rm km\ s^{-1}}}\right)^2 \tag{4.6}$$

where the FWHM of broad Paα is the analog to the velocity in the virial mass estimator and $L_{\rm Pa\alpha}$ of the broad component is the analog to the distance to the BLR. From Equation (4.6), our NIRSPEC and NIRES measurements give a BH mass of $\log(M_{\rm BH}/M_\odot)$ $= 6.59\pm0.32$ and 6.78 ± 0.14 for J0851+3926, and 6.83 ± 0.27 and 6.80 ± 0.32 for J1228+5814. The listed uncertainties come from the random error estimates in the fitting process. Accounting for systematic uncertainties, virial BH mass estimates typically have errors of 0.3 - 0.5 dex (eg., Shen, 2013; Reines & Volonteri, 2015). For a detailed description on virial mass uncertainties, see Sexton et al. (2019).

Bohn et al. (2020) compiled a sample of galaxies with secure BH mass estimates and obtained $M_{\rm BH}$–$M_{\rm bulge}$ and $M_{\rm BH}$–$M_{\rm stellar}$ relations. They found that bulgeless and/or disk dominated galaxies fall closer to the $M_{\rm BH}$–$M_{\rm stellar}$ relation, despite it having more scatter than the $M_{\rm bulge}$ relation. Moreover, they also found that bulgeless galaxies best correlate with late-type galaxies in the $M_{\rm BH}$–$M_{\rm stellar}$ relation. Indeed, with an estimated $M_{\rm stellar} = 10.61$ (Chang et al., 2015), J0851+3926 only lies 0.37 dex below the late-type relation. Similarly, J1228+5814 lies 0.41 dex below the same relation. Thus, it appears that these two bulgeless galaxies, which have presumably grown in the absence of major mergers, have managed to grow their SMBH enough to remain within the scatter of the $M_{\rm BH}$–$M_{\rm stellar}$ relation.

An important question for AGN hosts lacking a substancial bulge is what mechanism initiated the in-fall of gas towards the center to turn the AGN on. Close inspection of J0851+3926 reveals a faint tail leading to a small galaxy (see Figure 4.2). We obtained spectra of this target with the goal of estimating a redshift, however the spectra is featureless in all five orders of NIRES. While it is uncertain whether this is a true interacting companion, 2-dimensional surface brightness decompostions show that J0851+3926 has undisturbed disk. Thus, it is unlikely that this event is a major merger. Interestingly, as we will discuss in Section 4.7, counter-rotation is seen within the central kpc (see Figure 4.6). This could have been a product of an interaction with the aforementioned companion. Alternatively, a galactic bar could be present that is altering the angular momentum of the gas (Piner et al., 1995; Sheth et al., 2002; Wang et al., 2012). Follow-up, high resolution imaging will be needed to resolve the true nature of the central region.

Imaging of J1228+5814 shows two bright sources in the central region. Two-dimensional surface brightness decompositions confirm this; adding a second disk component greatly reduces the residuals of the fit. Some possible explanations of this include an off-centered AGN or an on-going merger event. Inspection of our spectroscopic data also show two sources. Only the southern one shows broad emission while the northern source only shows absorption features. There is no significant redshift difference between the absorption features in the two sources. If a merger event is indeed occurring, this could provide the in-fall of gas needed to start the gas accretion that is fueling the current AGN episode. However, the lack of a substantial bulge still indicates a relatively mergerless past, where mergers could not have contributed significantly to the growth of the SMBH.

In conclusion, both targets fall within the scatter of other late-type galaxies and the $M_{\rm BH}$ we measure are some of the highest reported for bulgeless galaxies in the literature. Although follow-up observations are needed to ascertain the triggering mechanism of the AGN, it is certainly intriguing how these BHs grew to supermassive sizes through secular processes in the absence of major mergers that would have also built up a significant bulge component.

4.7 Probing Dark Matter via Rotation Curves

Spatially extended emission is detected in a number of galaxies, enabling us to perform analysis on the kinematics of the gas (see Figure 4.6). We describe in Appendix 6.7 the procedure used to extract rotation velocities for seven targets where this was possible.

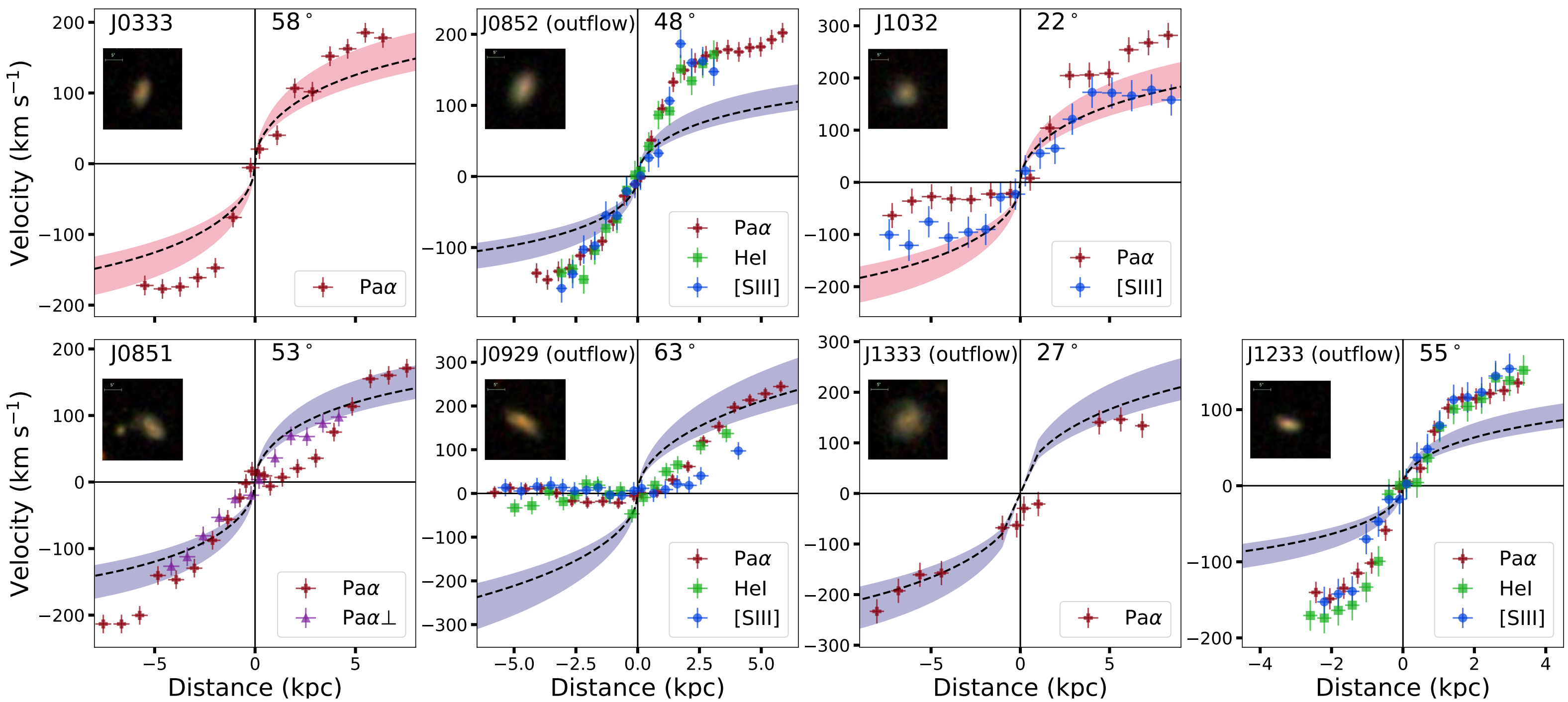

Figure 4.6: Velocity curves, corrected for inclination, showing the gas kinematics of the galaxies in our sample that show extended emission lines. The black dotted line represents velocities expected from an NFW model, assuming a concentration parameter of 10. The shaded blue/red regions represent the concentration parameter varying from 8 to 15. Here, blue identifies targets with confirmed AGN and red identifies targets dominated by stellar emission. Images from SDSS and inclination values are also included. Notice that J0851+3926 might show signs of a counter-rotating bar, as discussed in Appendix 6.6 and presented in detail in (Bohn et al., 2020).

The rotation curves of these galaxies showing measurable extended gas emission are shown in Figure 4.6.

We mainly plot Paα but also report [S III] 0.953 μm and He I 1.083 μm if detectable. Also note that two observed velocity profiles are plotted for J0851+3926. This is because we observed this target on two separate occasions with the slits positioned perpendicular to each other (see Figure 4.2). Plotted error bars include spectral and fitting errors as well as the uncertainties in the ellipticity and the value of q.

The shaded regions of Figure 4.6 represent velocity curves assuming a Navarro-Frenk-White (NFW) dark matter density profile (Navarro et al., 1996) and using abundance matching from Moster et al. (2013) to calculate the corresponding halo mass starting from the stellar masses of our targets. We assume a concentration parameter $c = 10$ (dotted black line in Figure 4.6), but vary c between $8 - 15$ to illustrate the uncertainty in this parameter (shaded areas). Our stellar mass, $M_\star$, estimates come from Chang et al. (2015), who performed SED fitting on optical and IR data. These values are also consistent with the MPA/JHU catalog[6]. The halo mass and other associated values are listed in Table 4.5.

[6] https://wwwmpa.mpa-garching.mpg.de/SDSS/

Table 4.5: Gas Rotation and Galaxy Parameters

Galaxy	$\log(M_\star)$ ($M_\odot$)	$\log(M_{DM})$ ($M_\odot$)	Inc. Angle	Outflow	> NFW Velocities
(1)	(2)	(3)	(4)	(5)	(6)
SDSS J0333+0107	$10.67^{+0.10}_{-0.08}$	$12.23^{+0.30}_{-0.17}$	58°	—	—
SDSS J0851+3926	$10.61^{+0.10}_{-0.09}$	$12.13^{+0.26}_{-0.17}$	53°	—	—
SDSS J0852+2928	$10.22^{+0.09}_{-0.09}$	$11.69^{+0.11}_{-0.11}$	48°	✓	✓
SDDS J0929+0026	$11.13^{+0.02}_{-0.09}$	$13.40^{+0.17}_{-0.33}$	63°	✓	—
SDSS J1032+3617	$10.83^{+0.09}_{-0.10}$	$12.56^{+0.32}_{-0.29}$	22°	—	—
SDSS J1233+0023	$10.01^{+0.10}_{-0.08}$	$11.54^{+0.12}_{-0.10}$	55°	✓	✓
SDSS J1333+6536	$10.93^{+0.08}_{-0.09}$	$12.84^{+0.31}_{-0.30}$	27°	✓	—

Columns: (1) Galaxy name. (2) Total stellar mass of the galaxy as determined in Chang et al. (2015). (3) Dark matter halo mass estimates as calculated through abundance matching. (4) Inclination angle of the galaxy (5) Presence of an outflow. (6) Observed rotational gas velocities are greater than NFW curve.

We find that, in general, our rotation curves are consistent with the estimates from NFW halos with masses estimated from abundance matching following Moster et al. (2013). However, two galaxies, J0852+2928 and J1233+0023, are worth highlighting since they have observed velocities that are significantly greater than those predicted by the NFW curve. They are both isolated and thus disruptions from a merger event are unlikely.

A more compelling, albeit speculative, interpretation is that these two galaxies inhabit a dark matter halo (DMH) that is more massive than estimates from abundance matching using their stellar mass. This would then indicate that some feedback process could have suppressed star formation, leading to the lower stellar galaxy mass. Since AGN-driven outflows are detected in both of these targets, winds could have expelled gas from the central regions and help lower star formation as a result of AGN feedback.

To quantify the discrepancy between the measured stellar mass and expected DMH mass of these two targets, we plot the $M_{\rm stellar}$–$M_{\rm H}$ relation in Figure 4.7 as derived in Moster et al. (2013). Here, we plot the stellar mass of our sample (as derived in Chang et al., 2015) against the DMH mass as calculated from the observed velocities in our data. Due to their high observed velocities, the estimated DMH mass of the two targets places them about 0.7 and 1.1 dex below the relation, outside the general scatter of the other targets.

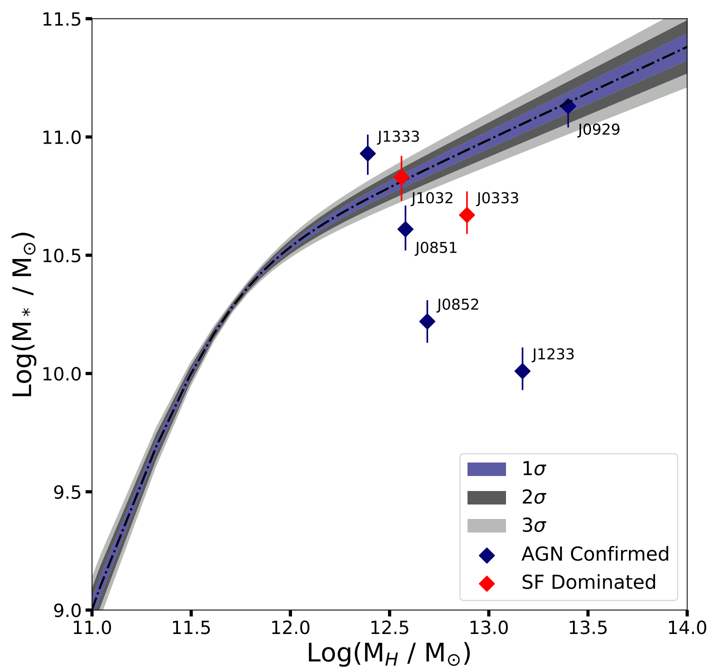

Figure 4.7: Total stellar mass vs. halo mass relation as calculated in Moster et al. (2013) through abundance matching. The colored contours represent one, two, and three sigma errors of the relation. Plotted as diamonds are the measured stellar mass and expected DMH mass of our sample. Blue represents galaxies with confirmed AGN while red represents targets whose emission is dominated by stellar processes.

When comparing these two with the other five targets, we see no distinguishing characteristics that would cause their stellar masses to be significantly underestimated. If the AGN is the source of regulating star formation, then this could lead to an intriguing and unique method of analyzing the effects of AGN feedback through rotation curves. However, further investigation with a larger sample and follow-up high-resolution IFS data will be needed to properly analyze the impact of AGN feedback on rotational velocities and assess the timescales on which AGN outflows affect star-formation in the local ISM.

As for the two targets with detected outflows but that do not show evidence of residing in a overmassive DMH (J0929+0026 and J1333+6536), a number of circumstances could explain why we do not see fast velocities. There is evidence of dust obscuration in J0929+0026 and a galactic bar in J1333+6536 that could be affecting the velocity profiles. Thus, it is difficult to judge what effect, if any, the outflows may be having on the mass distribution of these galaxies.

4.8 Conclusion

In this article, we presented Keck NIR spectroscopy of a sample of candidate AGN hosted in bulgeless galaxies. These galaxies were selected through MIR selection techniques and many are not classified as AGN by optical surveys. As such, we analyzed optical and NIR spectra to confirm AGN activity, and we also examined other characteristics that may be indicative of AGN feedback. The main results are as follows:

- We report evidence of AGN activity in 9/13 (69%) galaxies through NIR CL emission, broad emission, and Osterbrock et al. (1992) NIR line ratios.

- We detect strong [Si VI] 1.9630 μm in five galaxies. Due to the high IP of [Si VI] (167 eV), this strongly suggests AGN activity. Two of these targets also have [Ne V] λ3426 optical CL emission. Including detections of CL in two other targets of our sample by Satyapal et al. (2017), our total CL detection rate is 54% (7/13). Most of our non-detections of CLs can be explained by emission lines falling in telluric absorption, high extinction, or requiring deeper observations.

- We detect signatures of outflows in five of our targets, all of which have NIR CL detections suggesting a strong correlation between the two. The outflow velocities measured through [Si VI] (mean ∼890 km s^{-1}) tend to be faster than those measured through [O III] (mean ∼480 km s^{-1}), which is consistent with a decelerating outflow. In addition, we see a trend between AGN luminosity and [Si VI] luminosity which suggests that CL emission, and thus most likely the outflows, are of AGN origin.

- We observe a significant correlation between the spatial extent of the [Si VI] emission and the velocity of the outflowing coronal gas, with the fastest outflows (W_{80}∼2000 km s^{-1}) extending to over ∼1 kpc from the center of the galaxy, while the slower outflows (W_{80}∼400 km s^{-1}) tend to be confined to within a few hundred pc.

- Estimates to the mass and energies of the outflows in our sample are similar to those of disk-dominated galaxies with AGN-driven outflows, but are less than those of bulge-dominated galaxies. Our results are in agreement with those of (Smethurst et al., 2021), suggesting that merger-free galaxies may have outflows that are intrinsically different from those of galaxies with significant merger histories.

- We report virial estimates to BH masses in two galaxies of our sample. Both of these targets show broad Paα with no clear indication of broad-lines in their optical spectra. Their BH mass estimates, $\log(M_{\rm BH}/M_{\odot}) = 6.78$ and 6.80, respectively, place them both well within the scatter of other late-type galaxies in the $M_{\rm BH}$–$M_{\rm stellar}$ relation. More importantly, the lack of a strong bulge component indicates that secular processes, likely independent of major mergers, grew these BHs to supermassive sizes.

- Inspection of rotation curves reveals two targets with observed velocities significantly greater than those predicted by the NFW curve. This would suggest an unusually massive DMH compared to their observed stellar mass. In such interpretation, some feedback process could have quenched star formation, leading to a smaller stellar mass. Since outflows likely originating from the AGN are detected in both these galaxies, AGN feedback regulating star formation is certainly an intriguing possibility.

Chapter 5

Conclusion

To summarize the main results, we find MIR selection techniques to be an effective means to identify obscured AGN. Indeed, in Chapter 3, we report evidence of AGN activity in 9/13 (69%) galaxies through NIR CL emission, broad emission, and Osterbrock et al. (1992) NIR line ratios. Many of these targets do not show any clear indication of AGN activity in their optical spectrum. As such, we have shown that large optical surveys can indeed miss a population of hidden BHs, which highlights the need for IR spectroscopic observations to uncover them.

Through the use of broad-line emission, we report virial estimates to BH masses in two galaxies of our sample. Both of these targets show broad Paα with no clear indication of broad-lines in their optical spectra. Their BH mass estimates, $\log(M_{\rm BH}/M_{\odot}) = 6.78$ and 6.80, respectively, place them both well within the scatter of other late-type galaxies in the $M_{\rm BH}$–$M_{\rm stellar}$ relation. More importantly, the lack of a strong bulge component indicates that secular processes, likely independent of major mergers, grew these BHs to supermassive sizes.

Another key aspect of my research is the analysis of AGN outflows and their kinematics. We confirm fast, kpc outflows in both dwarf and bulgeless galaxies. Estimates to the mass and energies of the outflows in our bulgeless sample are similar to those of disk-dominated galaxies with AGN-driven outflows, but are less than those of bulge-dominated galaxies. These results are in agreement with those of (Smethurst et al., 2021), suggesting that merger-free galaxies may have outflows that are intrinsically different from those of galaxies with significant merger histories. In addition, we detect a strong correlation between the detection rete of CLs and outflows. The outflow velocities measured through [Si VI] tend to be faster than those measured through [O III], indicating the outflows are decelerating. In addition, we see a trend between AGN luminosity and [Si VI] luminosity which suggests that CL emission, and thus most likely the outflows, are of AGN origin.

Lastly, inspection of rotation curves reveals two targets with observed velocities significantly greater than those predicted by the NFW curve. This would suggest an unusually massive DMH compared to their observed stellar mass. In such interpretation, some feedback process could have quenched star formation, leading to a smaller stellar mass. Since outflows likely originating from the AGN are detected in both these galaxies, AGN feedback regulating star formation is certainly an intriguing possibility.

In conclusion, the growing number AGN discoveries in dwarf and bulgeless galaxies necessitates a re-evaluation of the impact of AGN in these populations. Through the research presented in this Dissertation paper, we confirm that the IR allows for a compelling avenue of studying these AGN that are typically heavily obscured. With the launch of JWST, a new era of IR studies is just around the corner. This researched has laid the foundation for follow-up IR studies and the samples covered here will play a pivotal role in our understanding of the origin of SMBHs and the BH-galaxy co-evolution in the JWST era.

Bibliography

Agarwal, B., Dalla Vecchia, C., Johnson, J. L., Khochfar, S., & Paardekooper, J.-P. 2014, MNRAS, 443, 648, doi: 10.1093/mnras/stu1112

Algorry, D. G., Navarro, J. F., Abadi, M. G., et al. 2014, MNRAS, 437, 3596, doi: 10.1093/mnras/stt2154

Allen, M. G., Groves, B. A., Dopita, M. A., Sutherland, R. S., & Kewley, L. J. 2008, ApJS, 178, 20, doi: 10.1086/589652

Allington-Smith, J., Murray, G., Content, R., et al. 2002, PASP, 114, 892, doi: 10.1086/341712

Antonucci, R. 1993, ARA&A, 31, 473, doi: 10.1146/annurev.aa.31.090193.002353

Antonucci, R. R. J., & Miller, J. S. 1985, ApJ, 297, 621, doi: 10.1086/163559

Araya Salvo, C., Mathur, S., Ghosh, H., Fiore, F., & Ferrarese, L. 2012, ApJ, 757, 179, doi: 10.1088/0004-637X/757/2/179

Assef, R. J., Stern, D., Kochanek, C. S., et al. 2013, ApJ, 772, 26, doi: 10.1088/0004-637X/772/1/26

Avery, C. R., Wuyts, S., Förster Schreiber, N. M., et al. 2021, MNRAS, 503, 5134, doi: 10.1093/mnras/stab780

Bae, H.-J., & Woo, J.-H. 2016, ApJ, 828, 97, doi: 10.3847/0004-637X/828/2/97

Bae, H.-J., Woo, J.-H., Karouzos, M., et al. 2017, ApJ, 837, 91, doi: 10.3847/1538-4357/aa5f5c

Baldassare, V. F., Reines, A. E., Gallo, E., & Greene, J. E. 2015, ApJL, 809, L14, doi: 10.1088/2041-8205/809/1/L14

—. 2017a, ApJ, 836, 20, doi: 10.3847/1538-4357/836/1/20

—. 2017b, ApJ, 850, 196, doi: 10.3847/1538-4357/aa9067

Baldassare, V. F., Reines, A. E., Gallo, E., et al. 2016, ApJ, 829, 57, doi: 10.3847/0004-637X/829/1/57

Baldwin, J. A., Phillips, M. M., & Terlevich, R. 1981, PASP, 93, 5, doi: 10.1086/130766

Barth, A. J., Ho, L. C., Rutledge, R. E., & Sargent, W. L. W. 2004, ApJ, 607, 90, doi: 10.1086/383302

Barth, A. J., Strigari, L. E., Bentz, M. C., Greene, J. E., & Ho, L. C. 2009, ApJ, 690, 1031, doi: 10.1088/0004-637X/690/1/1031

Becker, G. D., Rauch, M., & Sargent, W. L. W. 2009, ApJ, 698, 1010, doi: 10.1088/0004-637X/698/2/1010

Bell, E. F., McIntosh, D. H., Katz, N., & Weinberg, M. D. 2003, ApJS, 149, 289, doi: 10.1086/378847

Bentz, M. C., & Katz, S. 2015, PASP, 127, 67, doi: 10.1086/679601

Bentz, M. C., & Manne-Nicholas, E. 2018, ApJ, 864, 146, doi: 10.3847/1538-4357/aad808

Bentz, M. C., Denney, K. D., Grier, C. J., et al. 2013, ApJ, 767, 149, doi: 10.1088/0004-637X/767/2/149

Bohn, T., Canalizo, G., Satyapal, S., & Pfeifle, R. W. 2020, ApJ, 899, 82, doi: 10.3847/1538-4357/aba52c

Bohn, T., Canalizo, G., Veilleux, S., & Liu, W. 2021, ApJ, 911, 70, doi: 10.3847/1538-4357/abe70c

Bower, R. G., Benson, A. J., Malbon, R., et al. 2006, MNRAS, 370, 645, doi: 10.1111/j.1365-2966.2006.10519.x

Bradford, J. D., Geha, M. C., Greene, J. E., Reines, A. E., & Dickey, C. M. 2018, ApJ, 861, 50, doi: 10.3847/1538-4357/aac88d

Bradley, L., Sipőcz, B., Robitaille, T., et al. 2020, astropy/photutils: 1.0.0, 1.0.0, Zenodo, doi: 10.5281/zenodo.4044744. https://doi.org/10.5281/zenodo.4044744

Bromm, V., & Loeb, A. 2003, ApJ, 596, 34, doi: 10.1086/377529

Cann, J. M., Satyapal, S., Bohn, T., et al. 2020, ApJ, 895, 147, doi: 10.3847/1538-4357/ab8b64

Cann, J. M., Satyapal, S., Rothberg, B., et al. 2021, ApJL, 912, L2, doi: 10.3847/2041-8213/abf56d

Cappellari, M. 2017, MNRAS, 466, 798, doi: 10.1093/mnras/stw3020

Cappellari, M., & Emsellem, E. 2004, PASP, 116, 138, doi: 10.1086/381875

Cardelli, J. A., Clayton, G. C., & Mathis, J. S. 1989, ApJ, 345, 245, doi: 10.1086/167900

Cattaneo, A., Faber, S. M., Binney, J., et al. 2009, Nature, 460, 213, doi: 10.1038/nature08135

Cerqueira-Campos, F. C., Rodríguez-Ardila, A., Riffell, R., et al. 2020, arXiv e-prints, arXiv:2010.12595. https://arxiv.org/abs/2010.12595

Chambers, K. C., Magnier, E. A., Metcalfe, N., et al. 2016, arXiv e-prints, arXiv:1612.05560. https://arxiv.org/abs/1612.05560

Chang, Y.-Y., van der Wel, A., da Cunha, E., & Rix, H.-W. 2015, ApJS, 219, 8, doi: 10.1088/0067-0049/219/1/8

Ciambur, B. C. 2015, ApJ, 810, 120, doi: 10.1088/0004-637X/810/2/120

—. 2016, PASA, 33, e062, doi: 10.1017/pasa.2016.60

Cicone, C., Maiolino, R., Sturm, E., et al. 2014, A&A, 562, A21, doi: 10.1051/0004-6361/201322464

Cisternas, M., Jahnke, K., Bongiorno, A., et al. 2011, ApJ, 741, L11, doi: 10.1088/2041-8205/741/1/L11

Coelho, B., Antón, S., Lobo, C., & Ribeiro, B. 2013, MNRAS, 436, 2426, doi: 10.1093/mnras/stt1736

Colina, L., Piqueras López, J., Arribas, S., et al. 2015, A&A, 578, A48, doi: 10.1051/0004-6361/201425567

Combes, F. 2008, in IAU Symposium, Vol. 245, Formation and Evolution of Galaxy Bulges, ed. M. Bureau, E. Athanassoula, & B. Barbuy, 151–160

Concas, A., Popesso, P., Brusa, M., et al. 2017, A&A, 606, A36, doi: 10.1051/0004-6361/201629519

Costa, T., Pakmor, R., & Springel, V. 2020, MNRAS, 497, 5229, doi: 10.1093/mnras/staa2321

Cresci, G., Mainieri, V., Brusa, M., et al. 2015, ApJ, 799, 82, doi: 10.1088/0004-637X/799/1/82

Croton, D. J., Springel, V., White, S. D. M., et al. 2006, MNRAS, 365, 11, doi: 10.1111/j.1365-2966.2005.09675.x

Dabringhausen, J., & Fellhauer, M. 2016, MNRAS, 460, 4492, doi: 10.1093/mnras/stw1248

Davis, B. L., Graham, A. W., & Cameron, E. 2018, ApJ, 869, 113, doi: 10.3847/1538-4357/aae820

—. 2019, ApJ, 873, 85, doi: 10.3847/1538-4357/aaf3b8

Davis, B. L., Graham, A. W., & Seigar, M. S. 2017, MNRAS, 471, 2187, doi: 10.1093/mnras/stx1794

De Robertis, M. M., & Osterbrock, D. E. 1984, ApJ, 286, 171, doi: 10.1086/162585

—. 1986, ApJ, 301, 727, doi: 10.1086/163939

De Robertis, M. M., & Shaw, R. A. 1990, ApJ, 348, 421, doi: 10.1086/168251

den Brok, M., Seth, A. C., Barth, A. J., et al. 2015, ApJ, 809, 101, doi: 10.1088/0004-637X/809/1/101

Di Matteo, T., Springel, V., & Hernquist, L. 2005, Nature, 433, 604, doi: 10.1038/nature03335

Dimitrijević, M. S., Popović, L. Č., Kovačević, J., Dačić, M., & Ilić, D. 2007, MNRAS, 374, 1181, doi: 10.1111/j.1365-2966.2006.11238.x

Dong, R., Greene, J. E., & Ho, L. C. 2012, ApJ, 761, 73, doi: 10.1088/0004-637X/761/1/73

Dopita, M. A., & Sutherland, R. S. 2003, Astrophysics of the diffuse universe

Ellison, S. L., Patton, D. R., Mendel, J. T., & Scudder, J. M. 2011, MNRAS, 418, 2043, doi: 10.1111/j.1365-2966.2011.19624.x

Erkens, U., Appenzeller, I., & Wagner, S. 1997, A&A, 323, 707

Eskridge, P. B., Frogel, J. A., Pogge, R. W., et al. 2000, AJ, 119, 536, doi: 10.1086/301203

Fabian, A. C. 2012, ARA&A, 50, 455, doi: 10.1146/annurev-astro-081811-125521

Fall, S. M., & Romanowsky, A. J. 2018, ApJ, 868, 133, doi: 10.3847/1538-4357/aaeb27

Feoli, A., Mancini, L., Marulli, F., & van den Bergh, S. 2011, General Relativity and Gravitation, 43, 1007, doi: 10.1007/s10714-010-0963-y

Ferguson, J. W., Korista, K. T., & Ferland, G. J. 1997, ApJS, 110, 287, doi: 10.1086/312998

Ferrarese, L., & Merritt, D. 2000, ApJL, 539, L9, doi: 10.1086/312838

Ferrarese, L., Côté, P., Dalla Bontà, E., et al. 2006, ApJL, 644, L21, doi: 10.1086/505388

Filippenko, A. V., & Ho, L. C. 2003, ApJ, 588, L13, doi: 10.1086/375361

Filippenko, A. V., & Sargent, W. L. W. 1989, ApJL, 342, L11, doi: 10.1086/185472

Fisher, D. B., & Drory, N. 2008, AJ, 136, 773, doi: 10.1088/0004-6256/136/2/773

Foreman-Mackey, D., Hogg, D. W., Lang, D., & Goodman, J. 2013, PASP, 125, 306, doi: 10.1086/670067

Fruscione, A., McDowell, J. C., Allen, G. E., et al. 2006, in Proc. SPIE, Vol. 6270, Society of Photo-Optical Instrumentation Engineers (SPIE) Conference Series, 62701V

Gebhardt, K., Bender, R., Bower, G., et al. 2000, ApJL, 539, L13, doi: 10.1086/312840

Gehrels, N. 1986, ApJ, 303, 336, doi: 10.1086/164079

Gelbord, J. M., Mullaney, J. R., & Ward, M. J. 2009, MNRAS, 397, 172, doi: 10.1111/j.1365-2966.2009.14961.x

Georgiev, I. Y., Böker, T., Leigh, N., Lützgendorf, N., & Neumayer, N. 2016, MNRAS, 457, 2122, doi: 10.1093/mnras/stw093

Gimeno, G., Roth, K., Chiboucas, K., et al. 2016, in Society of Photo-Optical Instrumentation Engineers (SPIE) Conference Series, Vol. 9908, Proc. SPIE, 99082S

Giovanelli, R., Haynes, M. P., Salzer, J. J., et al. 1994, AJ, 107, 2036, doi: 10.1086/117014

Glikman, E., Helfand, D. J., & White, R. L. 2006, ApJ, 640, 579, doi: 10.1086/500098

Gliozzi, M., Satyapal, S., Eracleous, M., Titarchuk, L., & Cheung, C. C. 2009, ApJ, 700, 1759, doi: 10.1088/0004-637X/700/2/1759

Graham, A. W. 2001, AJ, 121, 820, doi: 10.1086/318767

Graham, A. W., & Scott, N. 2015, ApJ, 798, 54, doi: 10.1088/0004-637X/798/1/54

Graham, A. W., & Worley, C. C. 2008, MNRAS, 388, 1708, doi: 10.1111/j.1365-2966.2008.13506.x

Greene, J. E., & Ho, L. C. 2007, ApJ, 670, 92, doi: 10.1086/522082

Greene, J. E., Strader, J., & Ho, L. C. 2020, ARA&A, 58, 257, doi: 10.1146/annurev-astro-032620-021835

Greene, J. E., Peng, C. Y., Kim, M., et al. 2010, ApJ, 721, 26, doi: 10.1088/0004-637X/721/1/26

Groves, B. A., & Allen, M. G. 2010, NewA, 15, 614, doi: 10.1016/j.newast.2010.02.005

Groves, B. A., Dopita, M. A., & Sutherland, R. S. 2004a, ApJS, 153, 9, doi: 10.1086/421113

—. 2004b, ApJS, 153, 75, doi: 10.1086/421114

Häring, N., & Rix, H.-W. 2004, ApJL, 604, L89, doi: 10.1086/383567

Harrison, C. M., Alexander, D. M., Mullaney, J. R., & Swinbank, A. M. 2014, MNRAS, 441, 3306, doi: 10.1093/mnras/stu515

Harrison, C. M., Costa, T., Tadhunter, C. N., et al. 2018, Nature Astronomy, 2, 198, doi: 10.1038/s41550-018-0403-6

Harrison, C. M., Alexander, D. M., Mullaney, J. R., et al. 2016, MNRAS, 456, 1195, doi: 10.1093/mnras/stv2727

Hartmann, M., Debattista, V. P., Cole, D. R., et al. 2014, MNRAS, 441, 1243, doi: 10.1093/mnras/stu627

Heckman, T. M., Kauffmann, G., Brinchmann, J., et al. 2004, ApJ, 613, 109, doi: 10.1086/422872

Heckman, T. M., & Thompson, T. A. 2017, arXiv e-prints, arXiv:1701.09062. https://arxiv.org/abs/1701.09062

Hill, T. L., Heisler, C. A., Sutherland, R., & Hunstead, R. W. 1999, AJ, 117, 111, doi: 10.1086/300666

Ho, L. C., Filippenko, A. V., & Sargent, W. L. W. 1997, ApJ, 487, 568, doi: 10.1086/304638

Hopkins, P. F., Cox, T. J., Younger, J. D., & Hernquist, L. 2009, ApJ, 691, 1168, doi: 10.1088/0004-637X/691/2/1168

Hopkins, P. F., Kocevski, D. D., & Bundy, K. 2014, MNRAS, 445, 823, doi: 10.1093/mnras/stu1736

Hu, J. 2008, MNRAS, 386, 2242, doi: 10.1111/j.1365-2966.2008.13195.x

—. 2009, arXiv e-prints, arXiv:0908.2028. https://arxiv.org/abs/0908.2028

Hughes, T. M., Cortese, L., Boselli, A., Gavazzi, G., & Davies, J. I. 2013, A&A, 550, A115, doi: 10.1051/0004-6361/201218822

Into, T., & Portinari, L. 2013, MNRAS, 430, 2715, doi: 10.1093/mnras/stt071

Jaffarian, G. W., & Gaskell, C. M. 2020, MNRAS, 493, 930, doi: 10.1093/mnras/staa262

Jarrett, T. H., Cohen, M., Masci, F., et al. 2011, ApJ, 735, 112, doi: 10.1088/0004-637X/735/2/112

Jiang, N., Ho, L. C., Dong, X.-B., Yang, H., & Wang, J. 2013, ApJ, 770, 3, doi: 10.1088/0004-637X/770/1/3

Jiang, N., Wang, T., Zhou, H., et al. 2018, ApJ, 869, 49, doi: 10.3847/1538-4357/aaeb90

Jiang, Y.-F., Greene, J. E., Ho, L. C., Xiao, T., & Barth, A. J. 2011, ApJ, 742, 68, doi: 10.1088/0004-637X/742/2/68

Jogee, S., Scoville, N., & Kenney, J. D. P. 2005, ApJ, 630, 837, doi: 10.1086/432106

Johnson, J. L., & Bromm, V. 2007, MNRAS, 374, 1557, doi: 10.1111/j.1365-2966.2006.11275.x

Kang, D., & Woo, J.-H. 2018, ApJ, 864, 124, doi: 10.3847/1538-4357/aad561

Kaspi, S., Maoz, D., Netzer, H., et al. 2005, ApJ, 629, 61, doi: 10.1086/431275

Kauffmann, G., & Haehnelt, M. 2000, MNRAS, 311, 576, doi: 10.1046/j.1365-8711.2000.03077.x

Kauffmann, G., White, S. D. M., & Guiderdoni, B. 1993, MNRAS, 264, 201, doi: 10.1093/mnras/264.1.201

Kauffmann, G., Heckman, T. M., Tremonti, C., et al. 2003, MNRAS, 346, 1055, doi: 10.1111/j.1365-2966.2003.07154.x

Kelly, P. L., & Kirshner, R. P. 2012, ApJ, 759, 107, doi: 10.1088/0004-637X/759/2/107

Kelson, D. D. 2003, PASP, 115, 688, doi: 10.1086/375502

Kewley, L. J., Geller, M. J., & Jansen, R. A. 2004, AJ, 127, 2002, doi: 10.1086/382723

Kewley, L. J., Heisler, C. A., Dopita, M. A., & Lumsden, S. 2001, ApJS, 132, 37, doi: 10.1086/318944

Kim, D., Im, M., & Kim, M. 2010, ApJ, 724, 386, doi: 10.1088/0004-637X/724/1/386

Kim, D., Im, M., Canalizo, G., et al. 2018, ApJS, 238, 37, doi: 10.3847/1538-4365/aadfd5

King, A., & Pounds, K. 2015, ARA&A, 53, 115, doi: 10.1146/annurev-astro-082214-122316

Knop, R. A., Armus, L., Larkin, J. E., et al. 1996, AJ, 112, 81, doi: 10.1086/117990

Kormendy, J., & Ho, L. C. 2013, ARA&A, 51, 511, doi: 10.1146/annurev-astro-082708-101811

Kormendy, J., & Kennicutt, Robert C., J. 2004, Annual Review of Astronomy and Astrophysics, 42, 603, doi: 10.1146/annurev.astro.42.053102.134024

Kotilainen, J. K., Hyvönen, T., Reunanen, J., & Ivanov, V. D. 2012, MNRAS, 425, 1057, doi: 10.1111/j.1365-2966.2012.21425.x

La Franca, F., Onori, F., Ricci, F., et al. 2015, MNRAS, 449, 1526, doi: 10.1093/mnras/stv368

Lamastra, A., Bianchi, S., Matt, G., et al. 2009, A&A, 504, 73, doi: 10.1051/0004-6361/200912023

Lamperti, I., Koss, M., Trakhtenbrot, B., et al. 2017, MNRAS, 467, 540, doi: 10.1093/mnras/stx055

Landt, H., Bentz, M. C., Ward, M. J., et al. 2008, ApJS, 174, 282, doi: 10.1086/522373

Landt, H., Ward, M. J., Steenbrugge, K. C., & Ferland, G. J. 2015a, MNRAS, 449, 3795, doi: 10.1093/mnras/stv062

—. 2015b, MNRAS, 454, 3688, doi: 10.1093/mnras/stv2176

Leung, G. C. K., Coil, A. L., Aird, J., et al. 2019, ApJ, 886, 11, doi: 10.3847/1538-4357/ab4a7c

Liu, W., Veilleux, S., Canalizo, G., et al. 2020, arXiv e-prints, arXiv:2010.09008. https://arxiv.org/abs/2010.09008

Łokas, E. L., & Mamon, G. A. 2001, MNRAS, 321, 155, doi: 10.1046/j.1365-8711.2001.04007.x

Lutz, D., Sturm, E., Janssen, A., et al. 2020, A&A, 633, A134, doi: 10.1051/0004-6361/201936803

Maddox, N. 2018, MNRAS, 480, 5203, doi: 10.1093/mnras/sty2201

Manzano King, C. 2020, PhD thesis, Physics, University of California, Riverside

Manzano-King, C. M., & Canalizo, G. 2020, MNRAS, 498, 4562, doi: 10.1093/mnras/staa2654

Manzano-King, C. M., Canalizo, G., & Sales, L. V. 2019, ApJ, 884, 54, doi: 10.3847/1538-4357/ab4197

Maraston, C. 2005, MNRAS, 362, 799, doi: 10.1111/j.1365-2966.2005.09270.x

Maraston, C., Strömbäck, G., Thomas, D., Wake, D. A., & Nichol, R. C. 2009, MNRAS, 394, L107, doi: 10.1111/j.1745-3933.2009.00621.x

Marconi, A., & Hunt, L. K. 2003, ApJL, 589, L21, doi: 10.1086/375804

Marleau, F. R., Clancy, D., Habas, R., & Bianconi, M. 2017, A&A, 602, A28, doi: 10.1051/0004-6361/201629832

Martin, C. L. 1998, ApJ, 506, 222, doi: 10.1086/306219

Martin, G., Kaviraj, S., Volonteri, M., et al. 2018, MNRAS, 476, 2801, doi: 10.1093/mnras/sty324

Martins, L. P., Rodríguez-Ardila, A., de Souza, R., & Gruenwald, R. 2010, MNRAS, 406, 2168, doi: 10.1111/j.1365-2966.2010.17042.x

Martins, L. P., Rodríguez-Ardila, A., Diniz, S., Riffel, R., & de Souza, R. 2013, MNRAS, 435, 2861, doi: 10.1093/mnras/stt1482

Mason, R. E., Rodríguez-Ardila, A., Martins, L., et al. 2015, ApJS, 217, 13, doi: 10.1088/0067-0049/217/1/13

Mathur, S., Fields, D., Peterson, B. M., & Grupe, D. 2012, ApJ, 754, 146, doi: 10.1088/0004-637X/754/2/146

McAlpine, S., Harrison, C. M., Rosario, D. J., et al. 2020, MNRAS, 494, 5713, doi: 10.1093/mnras/staa1123

McAlpine, W., Satyapal, S., Gliozzi, M., et al. 2011, ApJ, 728, 25, doi: 10.1088/0004-637X/728/1/25

McConnell, N. J., & Ma, C.-P. 2013, ApJ, 764, 184, doi: 10.1088/0004-637X/764/2/184

McDermid, R. M., Alatalo, K., Blitz, L., et al. 2015, MNRAS, 448, 3484, doi: 10.1093/mnras/stv105

McElroy, R., Croom, S. M., Pracy, M., et al. 2015, MNRAS, 446, 2186, doi: 10.1093/mnras/stu2224

McGaugh, S. S., & Schombert, J. M. 2014, AJ, 148, 77, doi: 10.1088/0004-6256/148/5/77

McLean, I. S., Becklin, E. E., Bendiksen, O., et al. 1998, in Proc. SPIE, Vol. 3354, Infrared Astronomical Instrumentation, ed. A. M. Fowler, 566–578

Meidt, S. E., Schinnerer, E., van de Ven, G., et al. 2014, ApJ, 788, 144, doi: 10.1088/0004-637X/788/2/144

Moran, E. C., Shahinyan, K., Sugarman, H. R., Vélez, D. O., & Eracleous, M. 2014, AJ, 148, 136, doi: 10.1088/0004-6256/148/6/136

Morrissey, P., Matuszewski, M., Martin, D. C., et al. 2018, ApJ, 864, 93, doi: 10.3847/1538-4357/aad597

Moster, B. P., Naab, T., & White, S. D. M. 2013, MNRAS, 428, 3121, doi: 10.1093/mnras/sts261

Müller-Sánchez, F., Hicks, E. K. S., Malkan, M., et al. 2018a, ApJ, 858, 48, doi: 10.3847/1538-4357/aab9ad

Müller-Sánchez, F., Nevin, R., Comerford, J. M., et al. 2018b, Nature, 556, 345, doi: 10.1038/s41586-018-0033-2

Müller-Sánchez, F., Prieto, M. A., Hicks, E. K. S., et al. 2011, ApJ, 739, 69, doi: 10.1088/0004-637X/739/2/69

Nagao, T., Taniguchi, Y., & Murayama, T. 2000, AJ, 119, 2605, doi: 10.1086/301411

Navarro, J. F., Frenk, C. S., & White, S. D. M. 1996, ApJ, 462, 563, doi: 10.1086/177173

Nguyen, D. D., Seth, A. C., Reines, A. E., et al. 2014, ApJ, 794, 34, doi: 10.1088/0004-637X/794/1/34

Oke, J. B., Cohen, J. G., Carr, M., et al. 1995, PASP, 107, 375, doi: 10.1086/133562

Oliva, E., Origlia, L., Kotilainen, J. K., & Moorwood, A. F. M. 1995, A&A, 301, 55

Omand, C. M. B., Balogh, M. L., & Poggianti, B. M. 2014, MNRAS, 440, 843, doi: 10.1093/mnras/stu331

Osterbrock, D. E., & Ferland, G. J. 2006, Astrophysics of gaseous nebulae and active galactic nuclei

Osterbrock, D. E., Tran, H. D., & Veilleux, S. 1992, ApJ, 389, 196, doi: 10.1086/171197

Peng, C. Y., Ho, L. C., Impey, C. D., & Rix, H.-W. 2002, AJ, 124, 266, doi: 10.1086/340952

—. 2010, AJ, 139, 2097, doi: 10.1088/0004-6256/139/6/2097

Penny, S. J., Masters, K. L., Smethurst, R., et al. 2018, MNRAS, 476, 979, doi: 10.1093/mnras/sty202

Penston, M. V., Fosbury, R. A. E., Boksenberg, A., Ward, M. J., & Wilson, A. S. 1984, MNRAS, 208, 347, doi: 10.1093/mnras/208.2.347

Peterson, B. M., Bentz, M. C., Desroches, L.-B., et al. 2005, ApJ, 632, 799, doi: 10.1086/444494

Pfeifle, R. W., Satyapal, S., Secrest, N. J., et al. 2019, ApJ, 875, 117, doi: 10.3847/1538-4357/ab07bc

Piner, B. G., Stone, J. M., & Teuben, P. J. 1995, ApJ, 449, 508, doi: 10.1086/176075

Pritchard, T. A., Roming, P. W. A., Brown, P. J., et al. 2012, ApJ, 750, 128, doi: 10.1088/0004-637X/750/2/128

Rakshit, S., Stalin, C. S., Chand, H., & Zhang, X.-G. 2017, ApJS, 229, 39, doi: 10.3847/1538-4365/aa6971

Reines, A. E., Greene, J. E., & Geha, M. 2013, ApJ, 775, 116, doi: 10.1088/0004-637X/775/2/116

Reines, A. E., & Volonteri, M. 2015, ApJ, 813, 82, doi: 10.1088/0004-637X/813/2/82

Rho, J., Geballe, T. R., Banerjee, D. P. K., et al. 2018, ApJL, 864, L20, doi: 10.3847/2041-8213/aad77f

Ricci, F., La Franca, F., Onori, F., & Bianchi, S. 2017, A&A, 598, A51, doi: 10.1051/0004-6361/201629380

Rich, J. A., Kewley, L. J., & Dopita, M. A. 2011, ApJ, 734, 87, doi: 10.1088/0004-637X/734/2/87

—. 2014, ApJL, 781, L12, doi: 10.1088/2041-8205/781/1/L12

Riffel, R., Pastoriza, M. G., Rodríguez-Ardila, A., & Bonatto, C. 2009, MNRAS, 400, 273, doi: 10.1111/j.1365-2966.2009.15448.x

Riffel, R., Pastoriza, M. G., Rodríguez-Ardila, A., & Maraston, C. 2007, ApJL, 659, L103, doi: 10.1086/517999

Riffel, R., Rodríguez-Ardila, A., Aleman, I., et al. 2013, MNRAS, 430, 2002, doi: 10.1093/mnras/stt026

Rockosi, C., Stover, R., Kibrick, R., et al. 2010, in Society of Photo-Optical Instrumentation Engineers (SPIE) Conference Series, Vol. 7735, Proc. SPIE, 77350R

Rodríguez-Ardila, A., Prieto, M. A., Portilla, J. G., & Tejeiro, J. M. 2011, ApJ, 743, 100, doi: 10.1088/0004-637X/743/2/100

Rodríguez-Ardila, A., Prieto, M. A., Viegas, S., & Gruenwald, R. 2006, ApJ, 653, 1098, doi: 10.1086/508864

Rodríguez-Ardila, A., Viegas, S. M., Pastoriza, M. G., & Prato, L. 2002, ApJ, 579, 214, doi: 10.1086/342840

Rupke, D. 2018, Galaxies, 6, 138, doi: 10.3390/galaxies6040138

Rupke, D. S., Veilleux, S., & Sanders, D. B. 2005, ApJS, 160, 115, doi: 10.1086/432889

Rupke, D. S. N., Gültekin, K., & Veilleux, S. 2017, ApJ, 850, 40, doi: 10.3847/1538-4357/aa94d1

Sahu, N., Graham, A. W., & Davis, B. L. 2019, ApJ, 876, 155, doi: 10.3847/1538-4357/ab0f32

Sanders, D. B., Soifer, B. T., Elias, J. H., et al. 1988, ApJ, 325, 74, doi: 10.1086/165983

Sanders, R. L., Shapley, A. E., Kriek, M., et al. 2016, ApJ, 816, 23, doi: 10.3847/0004-637X/816/1/23

Sartori, L. F., Schawinski, K., Treister, E., et al. 2015, MNRAS, 454, 3722, doi: 10.1093/mnras/stv2238

Sarzi, M., Falcón-Barroso, J., Davies, R. L., et al. 2006, MNRAS, 366, 1151, doi: 10.1111/j.1365-2966.2005.09839.x

Satyapal, S., Böker, T., Mcalpine, W., et al. 2009, ApJ, 704, 439, doi: 10.1088/0004-637X/704/1/439

Satyapal, S., Secrest, N. J., McAlpine, W., et al. 2014, ApJ, 784, 113, doi: 10.1088/0004-637X/784/2/113

Satyapal, S., Vega, D., Dudik, R. P., Abel, N. P., & Heckman, T. 2008, ApJ, 677, 926, doi: 10.1086/529014

Satyapal, S., Vega, D., Heckman, T., O'Halloran, B., & Dudik, R. 2007, ApJ, 663, L9, doi: 10.1086/519995

Satyapal, S., Secrest, N. J., Rothberg, B., et al. 2016, ApJ, 827, 58, doi: 10.3847/0004-637X/827/1/58

Satyapal, S., Secrest, N. J., Ricci, C., et al. 2017, ApJ, 848, 126, doi: 10.3847/1538-4357/aa88ca

Savorgnan, G. A. D., Graham, A. W., Marconi, A. r., & Sani, E. 2016, ApJ, 817, 21, doi: 10.3847/0004-637X/817/1/21

Schawinski, K., Urry, M., Treister, E., et al. 2011b, ApJ, 743, L37, doi: 10.1088/2041-8205/743/2/L37

Schinnerer, E., Eckart, A., & Tacconi, L. J. 1998, ApJ, 500, 147, doi: 10.1086/305714

Schutte, Z., Reines, A. E., & Greene, J. E. 2019, ApJ, 887, 245, doi: 10.3847/1538-4357/ab35dd

Secrest, N. J., Satyapal, S., Gliozzi, M., et al. 2012, ApJ, 753, 38, doi: 10.1088/0004-637X/753/1/38

—. 2015, ApJ, 798, 38, doi: 10.1088/0004-637X/798/1/38

Sexton, R. O., Canalizo, G., Hiner, K. D., et al. 2019, ApJ, 878, 101, doi: 10.3847/1538-4357/ab21d5

Sexton, R. O., Matzko, W., Darden, N., Canalizo, G., & Gorjian, V. 2020, MNRAS, doi: 10.1093/mnras/staa3278

Sharp, R. G., & Bland-Hawthorn, J. 2010, ApJ, 711, 818, doi: 10.1088/0004-637X/711/2/818

Shen, Y. 2013, Bulletin of the Astronomical Society of India, 41, 61. https://arxiv.org/abs/1302.2643

Sheth, K., Vogel, S. N., Regan, M. W., et al. 2002, AJ, 124, 2581, doi: 10.1086/343835

Shields, J. C., Walcher, C. J., Böker, T., et al. 2008, ApJ, 682, 104, doi: 10.1086/589680

Shih, H.-Y., & Rupke, D. S. N. 2010, ApJ, 724, 1430, doi: 10.1088/0004-637X/724/2/1430

Shirazi, M., & Brinchmann, J. 2012, MNRAS, 421, 1043, doi: 10.1111/j.1365-2966.2012.20439.x

Simard, L., Mendel, J. T., Patton, D. R., Ellison, S. L., & McConnachie, A. W. 2011, ApJS, 196, 11, doi: 10.1088/0067-0049/196/1/11

Simard, L., Willmer, C. N. A., Vogt, N. P., et al. 2002, ApJS, 142, 1, doi: 10.1086/341399

Simmonds, C., Bauer, F. E., Thuan, T. X., et al. 2016, A&A, 596, A64, doi: 10.1051/0004-6361/201629310

Simmons, B. D., Smethurst, R. J., & Lintott, C. 2017, MNRAS, 470, 1559, doi: 10.1093/mnras/stx1340

Simmons, B. D., Lintott, C., Schawinski, K., et al. 2013, MNRAS, 429, 2199, doi: 10.1093/mnras/sts491

Smethurst, R. J., Simmons, B. D., Lintott, C. J., & Shanahan, J. 2019, MNRAS, 489, 4016, doi: 10.1093/mnras/stz2443

Smethurst, R. J., Simmons, B. D., Coil, A., et al. 2021, MNRAS, 507, 3985, doi: 10.1093/mnras/stab2340

Smith, N., Li, W., Silverman, J. M., Ganeshalingam, M., & Filippenko, A. V. 2011, MNRAS, 415, 773, doi: 10.1111/j.1365-2966.2011.18763.x

Stern, D., Assef, R. J., Benford, D. J., et al. 2012, ApJ, 753, 30, doi: 10.1088/0004-637X/753/1/30

Stern, J., & Laor, A. 2013, MNRAS, 431, 836, doi: 10.1093/mnras/stt211

Thomas, D., Steele, O., Maraston, C., et al. 2013, MNRAS, 431, 1383, doi: 10.1093/mnras/stt261

Thompson, R. I. 1995, ApJ, 445, 700, doi: 10.1086/175732

Thornton, C. E., Barth, A. J., Ho, L. C., Rutledge, R. E., & Greene, J. E. 2008, ApJ, 686, 892, doi: 10.1086/591519

Tully, R. B., & Fisher, J. R. 1977, A&A, 500, 105

U, V., Medling, A., Sanders, D., et al. 2013, ApJ, 775, 115, doi: 10.1088/0004-637X/775/2/115

U, V., Medling, A. M., Inami, H., et al. 2019, ApJ, 871, 166, doi: 10.3847/1538-4357/aaf1c2

Veilleux, S. 1991a, ApJ, 369, 331, doi: 10.1086/169765

—. 1991b, ApJS, 75, 383, doi: 10.1086/191535

Veilleux, S., Cecil, G., & Bland-Hawthorn, J. 2005, ARA&A, 43, 769, doi: 10.1146/annurev.astro.43.072103.150610

Veilleux, S., Goodrich, R. W., & Hill, G. J. 1997, ApJ, 477, 631, doi: 10.1086/303735

Veilleux, S., Maiolino, R., Bolatto, A. D., & Aalto, S. 2020, A&A Rv, 28, 2, doi: 10.1007/s00159-019-0121-9

Veilleux, S., & Osterbrock, D. E. 1987, ApJS, 63, 295, doi: 10.1086/191166

Villar Martín, M., Bellocchi, E., Stern, J., et al. 2015, MNRAS, 454, 439, doi: 10.1093/mnras/stv1864

Volonteri, M., Haardt, F., & Madau, P. 2003, ApJ, 582, 559, doi: 10.1086/344675

Wandel, A. 2002, ApJ, 565, 762, doi: 10.1086/338134

Wang, J., Kauffmann, G., Overzier, R., et al. 2012, MNRAS, 423, 3486, doi: 10.1111/j.1365-2966.2012.21147.x

Wang, S., Liu, J., Qiu, Y., et al. 2016, ApJS, 224, 40, doi: 10.3847/0067-0049/224/2/40

Westmoquette, M. S., Smith, L. J., & Gallagher, J. S. 2008, MNRAS, 383, 864, doi: 10.1111/j.1365-2966.2007.12628.x

Wilson, J. C., Henderson, C. P., Herter, T. L., et al. 2004, in Proc. SPIE, Vol. 5492, Ground-based Instrumentation for Astronomy, ed. A. F. M. Moorwood & M. Iye, 1295–1305

Woo, J.-H., Bae, H.-J., Son, D., & Karouzos, M. 2016, ApJ, 817, 108, doi: 10.3847/0004-637X/817/2/108

Woo, J.-H., Yoon, Y., Park, S., Park, D., & Kim, S. C. 2015, ApJ, 801, 38, doi: 10.1088/0004-637X/801/1/38

Wright, E. L., Eisenhardt, P. R. M., Mainzer, A. K., et al. 2010, AJ, 140, 1868, doi: 10.1088/0004-6256/140/6/1868

Yuan, W., Zhou, H., Dou, L., et al. 2014, ApJ, 782, 55, doi: 10.1088/0004-637X/782/1/55

Zakamska, N. L., Schmidt, G. D., Smith, P. S., et al. 2005, AJ, 129, 1212, doi: 10.1086/427543

Zibetti, S., Charlot, S., & Rix, H.-W. 2009, MNRAS, 400, 1181, doi: 10.1111/j.1365-2966.2009.15528.x

Chapter 6

Appendix

6.1 NIRSPEC Measurements

Here we show the fit to the NIRSPEC data (see Fig. 6.1). As mentioned in Section 2.3.2, our NIRSPEC data have a high degree of extinction due to heavy cloud cover, so we do not include the flux measurements in the bulk of our analysis. However, the FWHM of the broad component is still comparable to the NIRES data (see Table 2.2) and indicates that the broad emission is due to AGN activity and is not stellar in origin (see Section 2.3.2 for further details).

6.2 SDSS Measurements

In this section, we show the BADASS (R. Sexton et al. 2020, in preparation) fits to the SDSS spectrum. We fit two models: one with broad components included (Fig. 6.2, right panel) and the other without (Fig. 6.2, left panel). The best-fit model (overlaid in

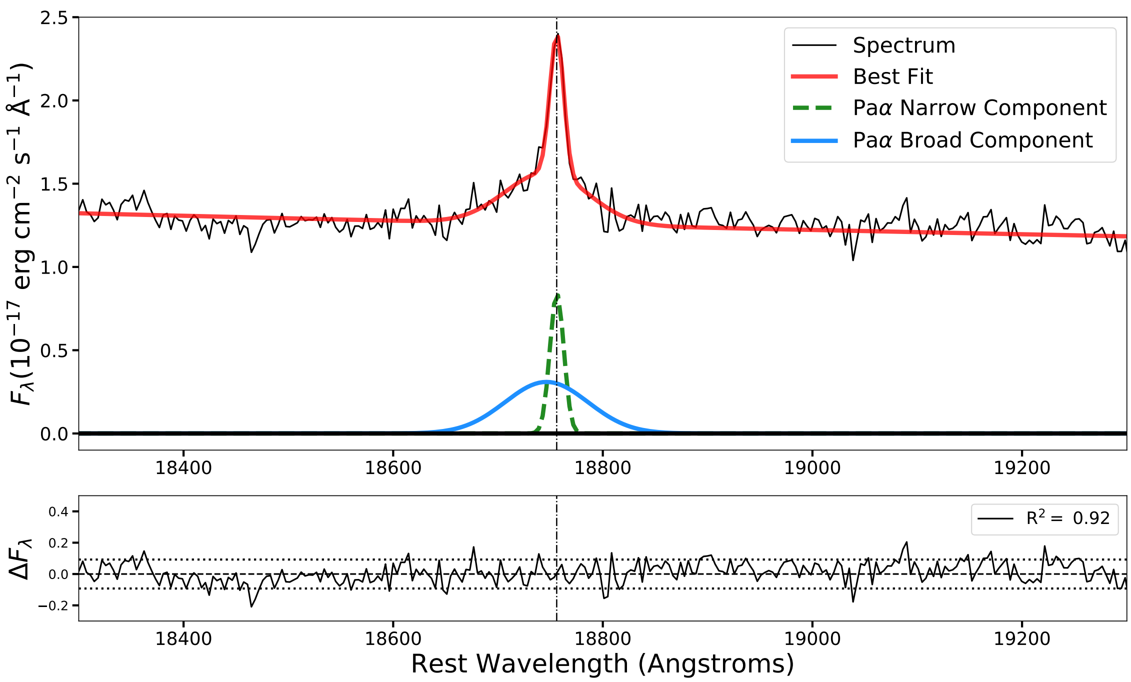

Figure 6.1: The MCMC fit to the NIRSPEC spectrum. In the top panel, Paα is centered with the best fit plotted over the spectrum. Below the spectrum are the narrow (dotted) and broad (solid) components. The bottom panel plots the residuals, 1σ noise level (horizontal dotted lines), and the R^2 value.

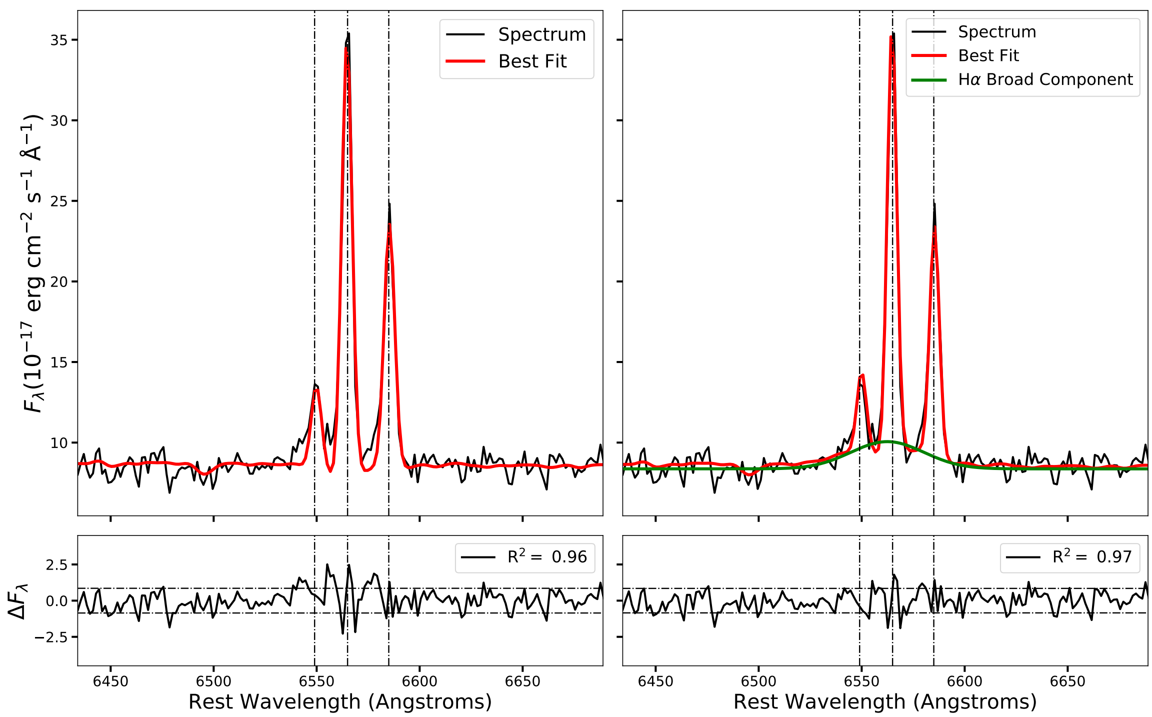

Figure 6.2: The MCMC fit to the SDSS spectrum. In the two top panels, Hα and [N II] $\lambda\lambda$6549, 6585 emission lines are shown, and the best fit to the data is plotted in red. The model on the left uses only single-component gaussian fits to each emission line, while the model on the right adds a broad Hα component, plotted in green. The bottom two panels plot the residuals, the 1σ noise level (horizontal dotted lines), and the R^2 values.

red) incorporates both Fe II emission and stellar absorption from the host galaxy. Outflows were tested for, but none were detected (see R. Sexton et al. 2020, in preparation for further details). Although the full SDSS spectrum was fit, we only show the Hα complex since there is substantial absorption in Hβ and no broad Hβ emission is detected. The FWHM of the broad Hα emission is $1911.81^{+248.66}_{-212.38}$ km s^{-1}, a factor of 1.4 above our NIRES Paα value. The amplitude is about two times the 1σ level of the noise, suggesting that a component could be there.

To compare the fits and quantify whether a broad component is needed, we ran the F-test: $F = (\sigma_{single})^2/(\sigma_{double})^2$, where σ is the standard deviation of the residuals using either single or double gaussian components. For the region around Hα, we obtain $F = 1.41$. Although this value suggests that adding a broad component does improve the fit, we cannot say for certain whether a significant broad component exists; a value closer to 2 or 3 is needed to provide more conclusive evidence. It is likely that the broad emission is heavily absorbed and any emission detected is dominated by the noise in the spectrum.

6.3 Methods and Measurements for M_{BH} Relations

Below is a summary of the methods used to estimate M_{bulge} and M_{stellar} of our sample described in Sections 2.4.1 and 2.4.2. The following tables quote the measurements and errors from each reference. Table 6.1 lists the bulgeless galaxies discussed in Section 2.4.1. The subsequent tables list mass measurements from Section 2.4.2 and are categorized based on the method used to estimate M_{BH}. Note that the M_{BH} derived from reverberation mapping and the virial method were recalculated using the updated f factor from Woo et al.

(2015) (see Section 2.4.2.1). Lastly, if uncertainties were not listed, then they are assumed to be 0.3 dex. All of the following tables are available for download.

Fall & Romanowsky (2018) calculated total stellar masses from K-band (2.2 μm) luminosities using a mass-to-light ratio, M_*/L_K, based on $B-V$ colors. To estimate M/L, they used $M_*/L_K = 0.96(B-V) + 0.01$. For spiral galaxies, which NGC 1024 is classified as, disk stellar masses were calculated separately and summed together with any measured bulge component to get the total stellar mass.

Davis et al. (2018, 2019) performed 2D decompositions of 3.6 μm images from the Spitzer Survey of Stellar Structure in Galaxies, with additional imaging from the *Hubble Space Telescope (HST)* F814W filter and the Two Micron All Sky Survey (2MASS) K_s band (2.2 μm). M/L ratios of 0.60, 1.88, and 0.62 were used for *Spitzer*, *HST*, and 2MASS data. To account for the contribution of dust emission at 3.6 μm, a $\sim 25\%$ reduction in the luminosity was included, leading to a $M_*/L_{\rm obs,IRAC1}$ of 0.453 for dusty galaxies.

Georgiev et al. (2016) obtained total stellar masses using the M/L color relations derived in Bell et al. (2003). B magnitudes and $B-V$ colors were obtained from HyperLeda[1] and were used in $\log(M_*/L_B) = 1.737(B-V)$ - 0.942 to obtain $M_{\rm stellar}$ for NGC 3319.

Kelly & Kirshner (2012) calculated total stellar masses by first estimating the flux using MAG_AUTO in SExtractor[2], where the radius of the aperture was set to be 2.5 Kron. M/L ratios were then estimated with SED fitting using PEGASE2[3] stellar population models.

[1] http://leda.univ-lyon1.fr/
[2] http://astroa.physics.metu.edu.tr/MANUALS/sextractor/
[3] http://www2.iap.fr/pegase/

McGaugh & Schombert (2014) compiled mass-to-light relations for a number of wavelength bands (V, I, and 3.6 μm) from various sources, including those from Bell et al. (2003) and Into & Portinari (2013), where $B-V$ colors were used. Magnitudes were taken from *Spitzer* and 2MASS. Values of $M_{\rm stellar}$ for NGC 3621 are consistent across all bands (within the assumed error of 0.3 dex), so we use the average of the values given by Into & Portinari (2013).

Hughes et al. (2013) utilized the $B-V$ color-dependent relations derived in Bell et al. (2003). H-band (1.65 μm) luminosities were taken from 2MASS and used in the equation: $\log(M_*/L_H) = 0.21(B-V) - 0.059$. $B-V$ colors were calculated using either B and V magnitudes from GOLDMine[4] or morphologically averaged values if observations were not available (taken from NED[5]).

Bentz & Manne-Nicholas (2018) obtained both optical and NIR imaging of their sample, with the optical data coming from high-resolution medium-band V HST observations and the NIR data from H-band images taken at WIYN Observatory. 2D decompositions were done with GALFIT with the higher-resolution HST fits guiding the NIR fit parameters. Masses were calculated using $V-H$ colors and the M/L relation $M_*/L_V = 1.493(V-H) - 0.681$ as derived in Into & Portinari (2013).

Reines & Volonteri (2015) present $M_{\rm stellar}$ of a sample of broad-line AGN utilizing SDSS g- and i-band photometry. A mock AGN spectrum was constructed for each source and then removed to isolate the host luminosity contribution. After correcting for galactic reddening, host galaxy masses were then calculated using $\log(M_*/L_i) = 1.032(g-i) - 0.963$

[4] http://goldmine.mib.infn.it/
[5] https://ned.ipac.caltech.edu/

(Zibetti et al., 2009). Additional stellar masses for a sample of dwarf galaxies, galaxies with reverberation-mapped AGN, and galaxies with dynamical $M_{\rm BH}$ are also provided. The AGN contribution was removed from the dwarf galaxy and reverberation-mapped subsamples, and the stellar mass was obtained in the same way as for the broad-line AGN. For the dynamical BH mass sample and Pox 52, which is not in the SDSS footprint, B and V magnitudes were obtained and stellar masses were calculated using $\log(M_*/L_K) = 1.176(B-V) - 1.390$ (Zibetti et al., 2009). For Pox 52, a dwarf elliptical, Barth et al. (2004) did not find any indication of a spiral or disk component with GALFIT decompositions, and so we adopt the same value of $M_{\rm stellar}$ as $M_{\rm bulge}$.

For UM 625, Graham & Scott (2015) report a $M_{\rm bulge}$ of 5.4×10^9 $M_\odot$. This is estimated from a V-band bulge magnitude of -19.06 and stellar M/L ratio of 1.6 (Jiang et al., 2013). For $M_{\rm stellar}$, we use the value given by Stern & Laor (2013), who obtained masses from SDSS z-band photometry. After removal of the AGN contribution, luminosities were converted to masses through a $L_{\rm [OIII]}$-dependent M/L ratio. Ratios ranged from 2.6 to 1.7 based on luminosities between 10^{39} and $10^{42.5}$ erg s^{-1}.

Chang et al. (2015) provide a catalog of stellar masses calculated from spectral energy distribution (SED) fitting of SDSS and WISE photometry. For the two galaxies analyzed, SDSS J004042.10–110957.6 and SDSS J074345.47+480813.5, Omand et al. (2014) have characterized these galaxies as bulge dominated with r-band B/T greater than 0.5 (0.53 and 0.58, respectively, when using a de Vaucouleurs model). Using the stellar mass and assuming a constant M/L ratio, we can obtain a rough estimate for $M_{\rm bulge}$: log $M_{\rm bulge}$

= 9.31 ± 0.30 for SDSS J004042.10–110957.6 and log $M_{\rm bulge}$ = 9.50 ± 0.30 for SDSS J074345.47+480813.5.

Schutte et al. (2019) expand on the work done by Reines & Volonteri (2015) by calculating $M_{\rm bulge}$ of their active dwarf galaxy sample. Optical and IR HST images were run through GALFIT to acquire magnitudes of each component. Magnitudes from HST filters (F606W and F110W) were then converted into SDSS r and g and 2MASS J magnitudes by fitting a wavelength-dependent flux density power law to the HST measurements and then evaluating the fit at the appropriate wavelengths. These new magnitudes were subsequently used in the M/L relation $\log(M_*/L_J) = 1.398(r-z) - 1.271$ provided by Zibetti et al. (2009).

Savorgnan et al. (2016) report bulge luminosities derived from decompositions of 3.6 μm *Spitzer* images. Individual M/L ratios based on [3.6] – [4.5] colors were used in the relation $\log(M_*/L_{3.6}) = 3.98(\pm0.98)([3.6] - [4.5]) + 0.13(\pm0.08)$ (Meidt et al., 2014) to convert luminosities to masses for each galaxy bulge component.

Table 6.1: Bulgeless Galaxy Sample

Galaxy	$\log(\frac{M_{\rm BH}}{M_\odot})$	Ref	$\log(\frac{M_{\rm stellar}}{M_\odot})$	Ref
NGC 1024	1.78 - 6.48	1	11.21 ± 0.10	2
NGC 2748	7.54 (+0.15, -0.23)	3	10.09 ± 0.22	4
NGC 3319	2.48 - 5.48	5	9.50 (+0.12, -0.17)	6
NGC 3367	8.75 ± 0.20	7	10.68 ± 0.30	8
NGC 3621	3.60 - 6.48	9	9.81 ± 0.30	10
NGC 4178	4.0 - 5.0	11	10.19 ± 0.30	12
NGC 4395	5.64 (+0.22, -0.12)	3	9.45 ± 0.08	4
NGC 4536	4.0 - 6.0	13	10.80 ± 0.30	12
NGC 4561	$> 4.30^a$	14	9.63 ± 0.30	12
NGC 6926	7.74 (+0.26, -0.74)	3	11.31 ± 0.08	4

[a] Lower Limit

Columns: (1) Galaxy name. (2) $M_{\rm BH}$ estimates from X-ray, IR, or virial measurements, typically lower/upper limits. (3) References for $M_{\rm BH}$. (4) Estimates for $M_{\rm stellar}$ of the galaxy. (5) References for $M_{\rm stellar}$.

References: (1) (Shields et al., 2008). (2) (Fall & Romanowsky, 2018). (3) (Davis et al., 2017). (4) (Davis et al., 2018). (5) (Jiang et al., 2018). (6) (Georgiev et al., 2016). (7) (Rakshit et al., 2017). (8) (Kelly & Kirshner, 2012). (9) (Satyapal et al., 2007; Barth et al., 2009; Gliozzi et al., 2009). (10) (McGaugh & Schombert, 2014). (11) (Secrest et al., 2012). (12) (Hughes et al., 2013). (13) (McAlpine et al., 2011). (14) (Araya Salvo et al., 2012).

Table 6.2: Galaxy Sample with Reverberation Mapped $M_{\rm BH}$ Measurements

Galaxy	$\log(\frac{M_{\rm BH}}{M_\odot})$	Ref	$\log(\frac{M_{\rm bulge}}{M_\odot})$	Ref	$\log(\frac{M_{\rm stellar}}{M_\odot})$	Ref
Ark 120	8.08 (+0.17, -0.18)	1	10.53 ± 0.30	2	10.68 ± 0.30	2
Arp 151	6.69 ± 0.17	1	10.19 ± 0.30	2	10.19 ± 0.30	2
3C 120	7.76 ± 0.16	1	10.70 ± 0.30	2	10.54 ± 0.30	2
3C 390.3	8.65 (+0.16, -0.17)	1	10.33 ± 0.30	2	10.66 ± 0.30	2
PG 0026+129	8.50 (+0.22, -0.24)	1	9.55 ± 0.30	2	9.55 ± 0.30	2
PG 0844+349	7.88 (+0.27, -0.35)	1	10.31 ± 0.30	2	10.36 ± 0.30	2
PG 1226+023	8.86 (+0.20, -0.23)	1	10.37 ± 0.30	2	10.37 ± 0.30	2
PG 1229+204	7.78 (+0.30, -0.34)	1	10.77 ± 0.30	2	10.73 ± 0.30	2
PG 1307+085	8.55 (+0.21, -0.28)	1	10.55 ± 0.30	2	10.55 ± 0.30	2
PG 1411+442	8.56 (+0.25, -0.29)	1	10.69 ± 0.30	2	10.69 ± 0.30	2
PG 1426+015	9.02 (+0.23, -0.28)	1	10.48 ± 0.30	2	10.67 ± 0.30	2
PG 1613+658	8.36 (+0.28, -0.39)	1	11.34 ± 0.30	2	11.34 ± 0.30	2
PG 1617+175	8.68 (+0.20, -0.25)	1	9.74 ± 0.30	2	9.74 ± 0.30	2
PG 1700+518	8.80 (+0.21, -0.22)	1	10.69 ± 0.30	2	10.69 ± 0.30	2
PG 2130+099	7.45 ± 0.18	1	11.11 ± 0.30	2	10.92 ± 0.30	2
SBS 1116+583A	6.58 (+0.20, -0.21)	1	9.05 ± 0.30	2	10.05 ± 0.30	2
Zw 229-015	6.93 (+0.19, -0.24)	1	9.64 ± 0.30	2	9.87 ± 0.30	2
Mrk 6	8.12 ± 0.16	1	10.82 ± 0.30	2	10.31 ± 0.30	2
Mrk 79	7.63 (+0.23, -0.26)	1	10.27 ± 0.30	2	10.31 ± 0.30	2
Mrk 110	7.31 ± 0.22	1	10.64 ± 0.30	2	10.47 ± 0.30	2
Mrk 202	6.15 ± 0.29	1	9.90 ± 0.30	2	9.69 ± 0.30	2
Mrk 279	7.45 (+0.22, -0.25)	1	10.92 ± 0.30	2	10.86 ± 0.30	2
Mrk 335	7.25 ± 0.16	1	9.99 ± 0.30	2	9.78 ± 0.30	2
Mrk 590	7.59 (+0.18, -0.19)	1	10.19 ± 0.30	2	11.01 ± 0.30	2
Mrk 817	7.60 (+0.18, -0.19)	1	10.91 ± 0.30	2	10.63 ± 0.30	2
Mrk 1310	6.23 (+0.19, -0.21)	1	9.71 ± 0.30	2	9.53 ± 0.30	2
Mrk 1501	8.08 (+0.24, -0.29)	1	10.49 ± 0.30	2	10.00 ± 0.30	2
NGC 3227	6.79 (+0.20, -0.23)	1	10.65 ± 0.30	2	10.78 ± 0.30	2
NGC 3516	7.41 (+0.16, -0.18)	1	10.30 ± 0.32	2	10.08 ± 0.32	2
NGC 4051	6.15 (+0.24, -0.28)	1	8.56 ± 0.32	2	9.56 ± 0.32	2
NGC 4151	7.57 ± 0.17	1	9.59 ± 0.32	2	10.01 ± 0.32	2
NGC 4253	6.84 (+0.17, -0.18)	1	9.64 ± 0.31	2	9.70 ± 0.31	2
NGC 4395	5.47 (+0.25, -0.26)	1	—	3	9.45 ± 0.08	4
NGC 4593	6.90 (+0.20, -0.22)	1	10.48 ± 0.32	2	10.40 ± 0.32	2
NGC 4748	6.42 (+0.23, -0.30)	1	10.66 ± 0.30	2	10.07 ± 0.30	2
NGC 6814	7.05 ± 0.18	1	9.45 ± 0.35	2	9.85 ± 0.35	2
NGC 7469	6.97 ± 0.17	1	9.64 ± 0.30	2	10.45 ± 0.30	2

Columns: (1) Galaxy name. (2) $M_{\rm BH}$ estimates from reverberation mapping. (3) References for $M_{\rm BH}$. (4) Estimates for $M_{\rm bulge}$. (5) References for $M_{\rm bulge}$. (6) Estimates for $M_{\rm stellar}$ of the galaxy. (7) References for $M_{\rm stellar}$.
References: (1) (Bentz & Katz, 2015). (2) (Bentz & Manne-Nicholas, 2018). (3) (Davis et al., 2019). (4) (Davis et al., 2018).

Hu (2009) analyzed K-band images from 2MASS and ran them through BUDDA[6], a 2D decomposition program, to obtain bulge luminosities. Masses of the bulges were then calculated from either $\log(M_*/L_K) = 0.135(B-V) - 0.356$ or $\log(M_*/L_K) = 0.349(r-i) -$

[6] http://www.sc.eso.org/~dgadotti/budda.html

Table 6.3: Galaxy Sample with Virial $M_{\rm BH}$ Measurements

Galaxy	$\rm FWHM_{H\alpha}{}^{a}$	$\log(\rm L_{H\alpha})^{b}$	$\log(\frac{M_{\rm BH}}{M_\odot})$	Ref	$\log(\frac{M_{\rm bulge}}{M_\odot})$	Ref	$\log(\frac{M_{\rm stellar}}{M_\odot})$	Ref
Pox 52	765 ± 30^{c}	$41.64\ (+0.10, -0.14)^{d}$	5.38 (+0.16, -0.18)	1	8.63 ± 0.30	5	8.63 ± 0.30	5
UM 625	1801 ± 48	40.36 ± 0.01	6.36 (+0.15, -0.14)	2	9.73 ± 0.30	6	10.00 ± 0.30	9
SDSS J004042.10-110957.6	2240 ± 224	39.53 ± 0.05	6.17 (+0.24, -0.23)	3	9.31 ± 0.30	7	9.59 ± 0.10	10
SDSS J074345.47+480813.5	1450 ± 145	39.81 ± 0.05	5.92 (+0.23, -0.24)	3	9.50 ± 0.30	7	9.74 ± 0.09	10
SDSS J024656.39-003304.8	1577 ± 158	39.38 (+0.06, -0.08)	5.81 (+0.22, -0.27)	4	8.21 ± 0.30	8	9.45 ± 0.30	5
SDSS J090613.75+561015.5	703 ± 70	40.15 ± 0.02	5.44 (+0.20, -0.24)	4	8.96 ± 0.30	8	9.30 ± 0.30	5
SDSS J095418.15+471725.1	636 ± 64	39.41 ± 0.06	5.01 (+0.22, -0.26)	4	7.97 ± 0.30	8	9.24 ± 0.30	5
SDSS J144012.70+024743.5	747 ± 75	39.73 (+0.05, -0.06)	5.31 (+0.21, -0.26)	4	8.14 ± 0.30	8	9.30 ± 0.30	5
SDSS J085125.81+393541.7	894 ± 89	39.67 (+0.05, -0.06)	5.44 (+0.21, -0.26)	4	7.87 ± 0.30	8	9.12 ± 0.30	5
SDSS J152637.36+065941.6	1043 ± 104	40.16 ± 0.02	5.80 (+0.20, -0.24)	4	7.49 ± 0.30	8	9.36 ± 0.30	5
SDSS J160531.84+174826.1	792 ± 79	39.45 ± 0.05	5.23 (+0.21, -0.26)	4	7.75 ± 0.30	8	9.36 ± 0.30	5

[a] FWHM are in units of km $\rm s^{-1}$, [b] Luminosities are in units of erg $\rm s^{-1}$, [c] FWHM of Hβ, [d] $\log(\lambda \rm L_{5100})$

Columns: (1) Galaxy Name. (2) FWM of the broad Hα (or Hβ for Pox 52) emission line. (3) Luminosity of broad Hα (or $\lambda \rm L_{5100}$ for Pox 52). (3) $M_{\rm BH}$ estimates from virial measurements. (3) References for $M_{\rm BH}$. (4) Estimates for $M_{\rm bulge}$. (5) References for $M_{\rm bulge}$. (6) Estimates for $M_{\rm stellar}$ of the galaxy. (7) References for $M_{\rm stellar}$.

References: (1) (Thornton et al., 2008). (2) (Jiang et al., 2013). (3) (Yuan et al., 2014). (4) (Reines et al., 2013). (5) (Reines & Volonteri, 2015). (6) (Graham & Scott, 2015). (7) (Omand et al., 2014) (8) (Schutte et al., 2019). (9) (Stern & Laor, 2013). (10) (Chang et al., 2015).

Table 6.4: Galaxy Sample with Dynamical $M_{\rm BH}$ Measurements

Galaxy	$\log(\frac{M_{\rm BH}}{M_\odot})$	Ref	$\log(\frac{M_{\rm bulge}}{M_\odot})$	Ref	$\log(\frac{M_{\rm stellar}}{M_\odot})$	Ref
Milky Way	6.60 ± 0.02	1	9.96 ± 0.05	5	10.78 ± 0.10	6
Circinus	6.25 (+0.07, -0.08)	1	10.12 ± 0.20	5	10.62 ± 0.18	6
Cygnus A	9.44 (+0.11, -0.14)	1	12.36 ± 0.20	5	12.38 ± 0.20	6
ESO 558-G009	7.26 (+0.03, -0.04)	1	9.89 ± 0.11	5	11.03 ± 0.10	6
IC 1459	9.38 (+0.15, -0.23)	2	11.32 ± 0.15	3	11.28 ± 0.30	7
IC 4296	9.04 (+0.07, -0.09)	2	12.12 ± 0.15	3	11.45 ± 0.30	7
IC 2560	6.49 (+0.08, -0.10)	1	9.63 ± 0.39	5	10.66 ± 0.37	6
PGC 49940	9.59 (+0.05, -0.06)	3	10.98 ± 0.15	3	11.54 ± 0.12	7
SDSS J043703.67+245606.8	6.51 (+0.04, -0.05)	1	9.90 ± 0.20	5	10.97 ± 0.10	6
Mrk 1029	6.33 (+0.10, -0.13)	1	9.90 ± 0.11	5	10.66 ± 0.09	6
NGC 221	6.40 (+0.08, -0.10)	3	8.53 ± 0.15	3	8.77 ± 0.30	7
NGC 224	8.15 (+0.22, -0.10)	1	10.11 ± 0.09	5	10.88 ± 0.10	6
NGC 253	7.00 ± 0.30	1	9.76 ± 0.09	5	10.71 ± 0.08	6
NGC 307	8.34 ± 0.13	4	10.43 ± 0.33	4	10.76 ± 0.12	4
NGC 404	4.85 ± 0.13	4	7.96 ± 0.27	4	9.12 ± 0.12	4
NGC 524	8.92 ± 0.10	4	10.57 ± 0.26	4	11.07 ± 0.12	4
NGC 821	7.59 (+0.22, -0.11)	2	10.55 ± 0.15	3	10.66 ± 0.30	7
NGC 1023	7.62 ± 0.04	2	10.26 ± 0.15	3	10.63 ± 0.30	7
NGC 1068	6.75 ± 0.02	1	10.27 ± 0.24	5	10.78 ± 0.18	6
NGC 1097	8.38 ± 0.03	1	10.83 ± 0.20	5	11.40 ± 0.10	6
NGC 1194	7.81 ± 0.04	4	10.71 ± 0.33	4	10.94 ± 0.12	4
NGC 1275	8.90 ± 0.20	4	11.84 ± 0.26	4	11.88 ± 0.12	4
NGC 1300	7.71 (+0.17, -0.12)	1	9.42 ± 0.25	5	10.30 ± 0.17	6
NGC 1316	8.18 (+0.18, -0.33)	2	11.01 ± 0.15	3	11.48 ± 0.30	7
NGC 1320	6.78 (+0.16, -0.26)	1	10.25 ± 0.40	5	10.58 ± 0.40	6
NGC 1332	9.16 (+0.06, -0.07)	2	10.91 (+0.26, -0.35)	2	10.92 ± 0.30	7
NGC 1374	8.76 ± 0.05	4	10.22 ± 0.26	4	10.52 ± 0.12	4
NGC 1398	8.03 ± 0.08	1	10.57 ± 0.20	5	11.25 ± 0.18	6
NGC 1399	8.67 (+0.05, -0.06)	2	11.12 ± 0.15	3	11.17 ± 0.30	7
NGC 1407	9.65 ± 0.08	4	11.46 ± 0.27	4	11.52 ± 0.12	4
NGC 1550	9.57 ± 0.06	4	11.13 ± 0.12	4	11.13 ± 0.12	4
NGC 1600	10.23 ± 0.05	4	11.82 ± 0.12	4	11.82 ± 0.12	4
NGC 2273	6.97 ± 0.03	1	9.98 ± 0.20	5	10.77 ± 0.19	6
NGC 2549	7.15 (+0.06, -1.15)	2	9.94 ± 0.15	3	10.01 ± 0.30	7
NGC 2748	7.54 (+0.15, -0.23)	1	—	5	10.09 ± 0.22	6
NGC 2778	7.18 (+0.20, -0.48)	2	9.40 (+0.24, -0.28)	2	10.66 ± 0.30	8
NGC 2787	7.60 ± 0.06	4	9.13 ± 0.26	4	9.99 ± 0.12	4
NGC 2960	7.06 ± 0.03	1	10.44 ± 0.36	5	10.86 ± 0.34	6
NGC 2974	8.23 ± 0.05	1	10.23 ± 0.13	5	10.73 ± 0.12	6
NGC 3031	7.83 (+0.11, -0.07)	1	10.16 ± 0.11	5	10.65 ± 0.08	6
NGC 3079	6.38 (+0.08, -0.10)	1	9.92 ± 0.25	5	10.68 ± 0.18	6
NGC 3091	9.56 (+0.01, -0.02)	2	11.48 (+0.04, -0.08)	2	11.29 ± 0.30	7
NGC 3115	8.94 (+0.33, -0.16)	2	10.19 ± 0.15	3	10.64 ± 0.30	7
NGC 3227	7.86 (+0.17, -0.25)	1	10.04 ± 0.17	5	10.80 ± 0.14	6
NGC 3245	8.30 (+0.10, -0.12)	2	10.44 ± 0.15	3	10.50 ± 0.30	7
NGC 3368	6.89 (+0.08, -0.10)	1	9.81 ± 0.10	5	10.69 ± 0.09	6
NGC 3377	7.88 (+0.02, -0.04)	2	9.96 ± 0.15	3	10.14 ± 0.30	7
NGC 3379 (M105)	8.60 (+0.10, -0.12)	2	10.67 ± 0.15	3	10.59 ± 0.30	7
NGC 3384	7.23 (+0.02, -0.05)	2	10.20 ± 0.15	3	10.46 ± 0.30	7
NGC 3393	7.49 (+0.05, -0.06)	1	10.23 ± 0.12	5	11.00 ± 0.10	6
NGC 3414	8.38 (+0.05, -0.06)	2	10.47 ± 0.15	3	10.95 ± 0.30	8
NGC 3489	6.76 ± 0.06	2	9.62 (+0.23, -0.26)	2	10.21 ± 0.30	7
NGC 3585	8.49 (+0.16, -0.09)	2	10.95 ± 0.15	3	10.96 ± 0.30	7
NGC 3607	8.11 (+0.14, -0.21)	2	10.90 ± 0.15	3	10.93 ± 0.30	7
NGC 3608	8.30 (+0.19, -0.15)	2	10.61 ± 0.15	3	10.69 ± 0.30	7
NGC 3627	6.95 ± 0.05	1	9.74 ± 0.20	5	10.78 ± 0.10	6
NGC 3665	8.76 ± 0.10	4	11.03 ± 0.26	4	11.28 ± 0.12	4
NGC 3842	9.99 (+0.12, -0.14)	2	11.79 (+0.05, -0.07)	2	11.44 ± 0.30	7
NGC 3923	9.45 ± 0.13	4	11.4 ± 0.15	4	11.40 ± 0.12	4

Galaxy	$\log(\frac{M_{\rm BH}}{M_\odot})$	Ref	$\log(\frac{M_{\rm bulge}}{M_\odot})$	Ref	$\log(\frac{M_{\rm stellar}}{M_\odot})$	Ref
NGC 3998	8.91 (+0.10, -0.12)	2	10.66 ± 0.15	3	10.41 ± 0.30	7
NGC 4026	8.26 ± 0.11	4	10.11 ± 0.33	4	10.36 ± 0.12	4
NGC 4151	7.68 (+0.15, -0.60)	1	10.27 ± 0.15	5	10.62 ± 0.14	6
NGC 4258	7.60 ± 0.01	1	10.05 ± 0.18	5	10.72 ± 0.09	6
NGC 4261	8.70 (+0.08, -0.10)	2	11.19 ± 0.15	3	11.33 ± 0.30	7
NGC 4291	8.52 (+0.10, -0.62)	2	10.55 ± 0.15	3	10.52 ± 0.30	7
NGC 4303	6.58 (+0.07, -0.26)	1	9.42 ± 0.10	5	10.48 ± 0.09	6
NGC 4339	7.63 ± 0.33	4	9.67 ± 0.26	4	10.17 ± 0.12	4
NGC 4342	8.65 ± 0.18	4	9.94 ± 0.25	4	10.26 ± 0.12	4
NGC 4350	8.86 ± 0.41	4	10.28 ± 0.26	4	10.55 ± 0.12	4
NGC 4371	6.84 ± 0.08	4	9.89 ± 0.26	4	10.60 ± 0.12	4
NGC 4374 (M84)	8.95 ± 0.04	2	11.45 (+0.23, -0.27)	2	11.29 ± 0.30	7
NGC 4388	6.90 (+0.04, -0.05)	1	10.07 ± 0.22	5	10.44 ± 0.22	6
NGC 4395	5.64 (+0.22, -0.12)	1	—	5	9.45 ± 0.08	6
NGC 4429	8.18 ± 0.09	4	10.46 ± 0.26	4	10.90 ± 0.12	4
NGC 4434	7.84 ± 0.17	4	9.91 ± 0.26	4	10.18 ± 0.12	4
NGC 4459	7.83 (+0.08, -0.09)	2	10.36 ± 0.15	3	10.56 ± 0.30	7
NGC 4472 (M49)	9.40 (+0.05, -0.02)	2	11.59 (+0.04, -0.07)	2	11.51 ± 0.30	7
NGC 4473	8.08 (+0.12, -0.60)	2	10.64 ± 0.15	3	10.55 ± 0.30	7
NGC 4486 (M87)	9.76 ± 0.03	2	11.28 ± 0.15	3	11.38 ± 0.30	7
NGC 4486A	7.11 (+0.12, -0.34)	3	10.06 ± 0.15	3	9.71 ± 0.30	7
NGC 4486B	8.76 ± 0.24	4	9.46 ± 0.33	4	9.46 ± 0.12	4
NGC 4501	7.13 ± 0.08	1	10.11 ± 0.16	5	10.67 ± 0.08	6
NGC 4526	8.67 ± 0.04	4	10.70 ± 0.26	4	11.04 ± 0.12	4
NGC 4552 (M89)	8.67 ± 0.05	4	10.88 ± 0.25	4	10.95 ± 0.12	4
NGC 4564	7.78 (+0.02, -0.07)	2	10.10 ± 0.15	3	10.23 ± 0.30	7
NGC 4578	7.28 ± 0.35	4	9.77 ± 0.26	4	10.23 ± 0.12	4
NGC 4594	8.81 ± 0.08	1	10.81 ± 0.20	5	11.03 ± 0.14	6
NGC 4596	7.90 (+0.17, -0.28)	2	10.19 ± 0.15	3	10.48 ± 0.30	7
NGC 4621 (M59)	8.59 (+0.04, -0.05)	2	10.53 ± 0.15	3	10.97 ± 0.30	8
NGC 4649	9.67 ± 0.10	4	11.44 ± 0.12	4	11.44 ± 0.12	4
NGC 4697	8.26 (+0.05, -0.02)	2	10.28 ± 0.15	3	10.63 ± 0.30	7
NGC 4699	8.34 ± 0.05	1	11.12 ± 0.26	5	11.29 ± 0.23	6
NGC 4736	6.78 (+0.09, -0.11)	1	9.89 ± 0.09	5	10.37 ± 0.08	6
NGC 4742	7.15 ± 0.18	4	9.87 ± 0.26	4	10.15 ± 0.12	4
NGC 4751	9.15 ± 0.05	4	10.49 ± 0.26	4	10.72 ± 0.12	4
NGC 4762	7.36 ± 0.15	4	9.97 ± 0.28	4	11.06 ± 0.12	4
NGC 4826	6.07 (+0.10, -0.12)	1	9.55 ± 0.22	5	10.41 ± 0.21	6
NGC 4889	10.32 (+0.25, -0.62)	2	11.96 (+0.05, -0.07)	2	11.81 ± 0.30	7
NGC 4945	6.15 ± 0.30	1	9.39 ± 0.19	5	10.52 ± 0.09	6
NGC 5018	8.02 ± 0.09	4	10.98 ± 0.27	4	11.35 ± 0.12	4
NGC 5055	8.94 (+0.09, -0.11)	1	10.49 ± 0.11	5	10.81 ± 0.10	6
NGC 5077	8.87 (+0.21, -0.23)	2	11.03 ± 0.15	3	10.99 ± 0.30	7
NGC 5128	7.65 (+0.14, -0.11)	2	10.09 ± 0.15	3	10.73 ± 0.30	7
NGC 5252	9.00 ± 0.40	4	10.85 ± 0.26	4	11.38 ± 0.12	4
NGC 5328	9.67 ± 0.15	4	11.49 ± 0.12	4	11.49 ± 0.12	4
NGC 5419	9.86 ± 0.14	4	11.44 ± 0.12	4	11.44 ± 0.12	4
NGC 5495	7.04 (+0.08, -0.09)	1	10.54 ± 0.12	5	11.31 ± 0.10	6
NGC 5516	9.52 ± 0.06	4	11.44 ± 0.12	4	11.44 ± 0.12	4
NGC 5576	8.20 (+0.07, -0.12)	2	10.28 ± 0.15	3	10.64 ± 0.30	7
NGC 5765b	7.72 ± 0.03	1	10.04 ± 0.13	5	11.11 ± 0.12	6
NGC 5813	8.83 ± 0.06	4	10.86 ± 0.26	4	11.23 ± 0.12	4
NGC 5845	8.41 ± 0.22	4	10.12 ± 0.26	4	10.32 ± 0.12	4
NGC 5846	9.04 ± 0.04	2	11.10 ± 0.15	3	11.40 ± 0.30	8
NGC 6086	9.57 ± 0.16	4	11.52 ± 0.26	4	11.52 ± 0.12	4
NGC 6251	8.77 (+0.15, -0.22)	2	11.66 (+0.04, -0.07)	2	11.55 ± 0.30	7
NGC 6264	7.51 ± 0.02	1	10.01 ± 0.15	5	11.06 ± 0.14	6
NGC 6323	7.02 ± 0.02	1	9.86 ± 0.31	5	11.04 ± 0.28	6
NGC 6861	9.30 ± 0.08	4	10.94 ± 0.29	4	11.02 ± 0.12	4
NGC 6926	7.74 (+0.26, -0.74)	1	—	5	11.31 ± 0.08	6

Galaxy	$\log(\frac{M_{\rm BH}}{M_\odot})$	Ref	$\log(\frac{M_{\rm bulge}}{M_\odot})$	Ref	$\log(\frac{M_{\rm stellar}}{M_\odot})$	Ref
NGC 7052	8.57 ± 0.23	4	11.46 ± 0.12	4	11.46 ± 0.12	4
NGC 7332	7.11 ± 0.20	4	10.22 ± 0.34	4	10.84 ± 0.12	4
NGC 7457	7.00 ± 0.30	4	9.40 ± 0.26	4	10.19 ± 0.12	4
NGC 7582	7.67 (+0.09, -0.08)	1	10.15 ± 0.20	5	10.77 ± 0.11	6
NGC 7619	9.40 (+0.12, -0.06)	2	11.52 (+0.23, -0.26)	2	11.34 ± 0.30	7
NGC 7768	9.11 (+0.14, -0.16)	2	11.76 (+0.20, -0.26)	2	11.40 ± 0.30	7
UGC 3789	7.06 (+0.02, -0.03)	1	10.18 ± 0.14	5	10.74 ± 0.13	6
UGC 6093	7.45 ± 0.04	1	10.35 ± 0.14	5	11.26 ± 0.11	6

Columns: Same as table 6.2 but with $M_{\rm BH}$ estimates from dynamical measurements.
References: (1) (Davis et al., 2017). (2) (Savorgnan et al., 2016). (3) (Hu, 2009). (4) (Sahu et al., 2019). (5) (Davis et al., 2019). (6) (Davis et al., 2018). (7) (Reines & Volonteri, 2015). (8) (Dabringhausen & Fellhauer, 2016).

0.336 (Bell et al., 2003) where extinction-corrected $B-V$ colors are provided by HyperLeda and the $r-i$ colors are from SDSS. If an AGN component was detected, the central 3″ region was removed to avoid contamination from the AGN. When available, we choose the $r-i$ relation since the magnitudes of the bulge effective radius were directly measured using the SDSS images.

Sahu et al. (2019) provide decompositions of early-type galaxies with archived *Spitzer* IRAC 3.6 μm images, SDSS r-band images, or 2MASS K_s-band images. PROFILER (Ciambur, 2015, 2016) and two IRAF tasks, ISOFIT and CMODEL, were used to model individual galaxy components and obtain magnitudes from which luminosities for the entire galaxy and bulge could be calculated. These luminosities were converted to stellar masses using the following constant stellar M/L ratios for each band: $M_*/L_{3.6\mu m} = 0.6$, $M_*/L_{K_s} = 0.7$, and $M_*/L_r = 2.8$.

For three galaxies, NGC 3414, NGC 4621, and NGC 5846, $M_{\rm stellar}$ were obtained from Dabringhausen & Fellhauer (2016). Here, age, color, and luminosity were all treated as parameters in their M/L calculations. Ages of the stellar population for all three galaxies are quoted from McDermid et al. (2015). V-band luminosity and $B-V$ colors came from

HyperLeda, and $g-r$ and $g-i$ values came from SDSS. A M/L ratio and $M_{\rm stellar}$ were then calculated from these values (see Equation 18 and Table 13 in Dabringhausen & Fellhauer (2016)).

6.4 Details of CL Emission

In this section, we cover the NIR spectra in our sample of dwarf galaxies, with particular detail to the CL emission and important absorption bands. The following subsections are in order of increasing RA of the galaxy. In the figures showing the full wavelength coverage of our data, we provide subplots that give additional detail to key features, such as absorption features and emission lines (or lack thereof). The measured properties of every NIR emission line detected at the 3σ level are listed in Tables 6.3 through 6.11. The listed uncertainties come from the random error estimates during the fitting process.

6.4.1 J010005.92-011058.89

J0100-0110 is one of only two galaxies in the composite region of the BPT diagram. Based on optical emission line measurements, Manzano-King & Canalizo (2020) reported disturbed gas that is offset from the stellar rotation curve derived from a Navarro-Frenk-White dark matter density profile (Navarro et al., 1996). Indeed, L20 reported strong, blueshifted [O III] emission in the southern portion of J0100-0110, seen predominately in the C2 component. They suggested that could be emission from the near side of a biconical outflow.

The NIR spectrum of J0100-0110 is shown in Figure 6.3 and line measurements are listed in Table 6.3. It is the only galaxy in our sample observed with NIRSPEC (wavelength coverage from ∼1.97 — 2.39 μm). Because of this, we cannot make estimates to the stellar age as we have done with the rest of the sample. The spectrum shows strong Paα and Brγ; it shows no CL emission in the K band. No significant optical CL emission is detected in this galaxy.

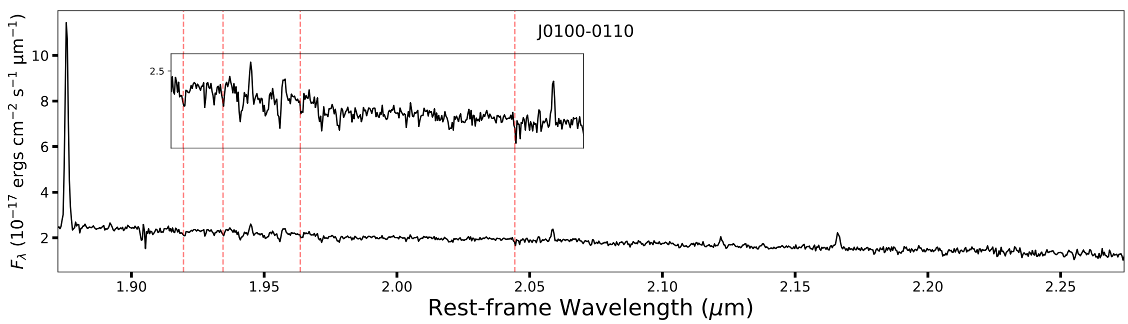

Figure 6.3: Spectrum of J0100-0110 taken with NIRSPEC, shifted to rest-frame wavelength using the systemic redshift. Red-dashed lines represent CLs that we do not detect at the 2σ level.

6.4.2 J081145.29+232825.72

Moran et al. (2014) reported a lower limit to the BH mass of log($M_{\rm BH}/M_\odot$) > 4.4 based on Eddington luminosity arguments. Wang et al. (2016) reported Chandra 0.3-8 keV flux, from which we calculate a 2-10 keV luminosity of 1.33 × 10^{39} erg s^{-1}. MC20 reported both disturbed and stratified gas in J0811+2328. Here, the gas is both offset from the stellar rotation curve, and the Balmer and forbidden lines are kinematically distinct from one another. In L20, only a single component was needed to fit the [O III] profile, but the larger line widths (relative to the velocity dispersion of the stellar components) and velocity offsets (up to -60 km s^{-1}) indicate that the outflow could be traced by this single profile.

The NIR spectrum of J0811+2328 is shown in Figure 6.4 and line measurements are listed in Table 6.4. We detect no NIR CL emission at the 2σ level, though deeper observations could reveal faint [S VIII], [Fe XIII], [S IX], and [Ca VIII]. These lines either fall on skylines or their S/N is consistent with the noise level so we do not include them in our analysis. The rest of the spectrum is relatively featureless aside from a handful of typically strong NIR lines, such as [S III] 0.9531 μm and He I 1.0830 μm. Unfortunately, the CN absorption at 1.1 μm falls within heavy telluric absorption so we cannot make an estimate on the contribution of a younger stellar population.

6.4.3 J084025.54+181858.99

Like J0811+2328, Moran et al. (2014) also reported a lower limit to the BH mass for J0840+1818, $\log(M_{\rm BH}/M_\odot) > 4.3$. MC20 reported evidence of disturbed gas and MK19 detect an outflow through a multicomponent fit to [O III]. Data from L20, however, show velocity offsets ranging from -30 km s^{-1} to +20 km s^{-1} and only a single Gaussian was used in the fit. In addition, the line widths are smaller than the velocity dispersions of the stellar component. This all suggests that the gas is rotating in the same direction as the stars and they found no clear evidence of outflows in their data.

The NIR spectrum of J0840+1818 is shown in Figure 6.5 and line measurements are listed in Table 6.5. We find no CLs at the 2σ detection level, though faint [Ca VIII] may be present. Similar to J0811+2328, we only detect a handful of emission lines and the 1.1 μm CN absorption falls within significant telluric absorption. MK19 do report the optical CL [Ne V] λ3426 emission.

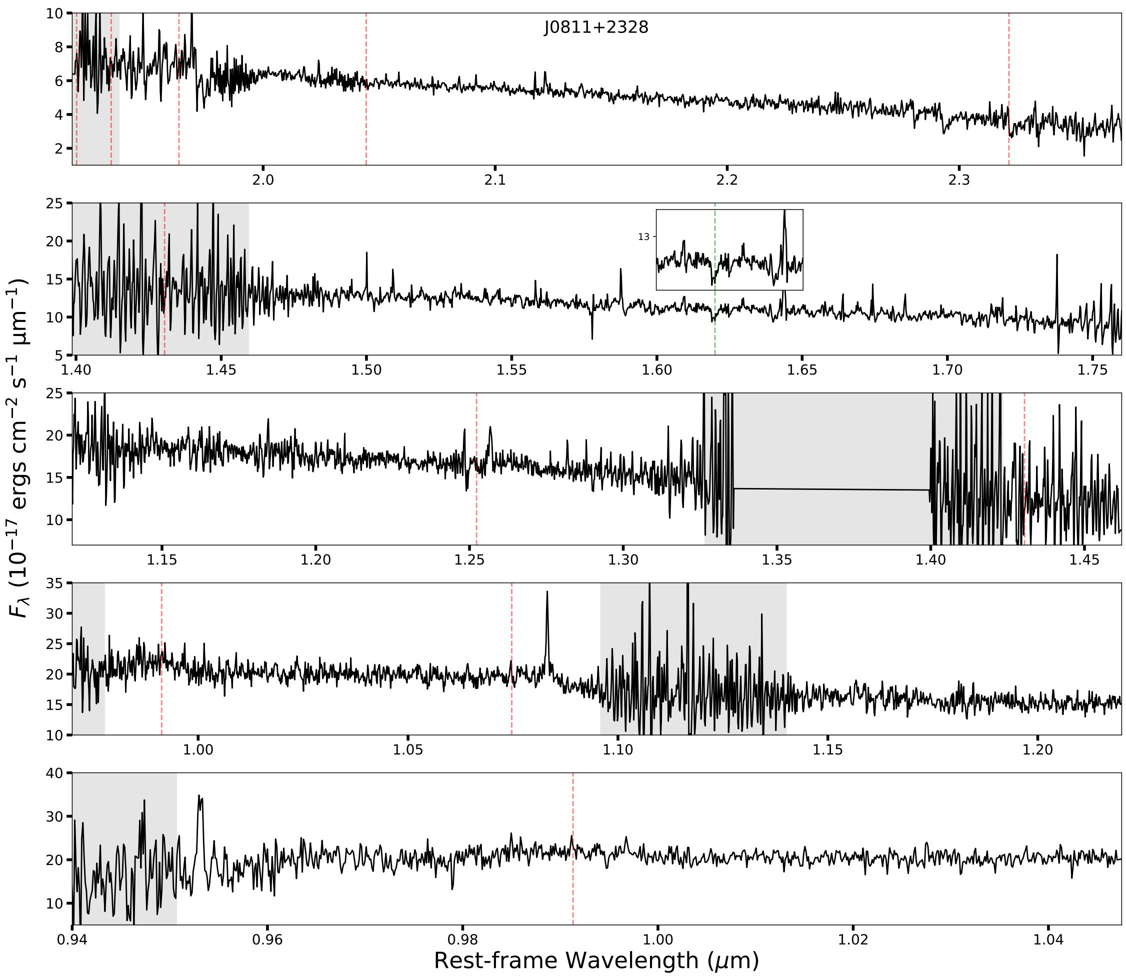

Figure 6.4: Spectrum of J0811+2328 taken with NIRES, shifted to rest-frame wavelength using the systemic redshift. Red- and green-dashed lines represent CLs that we do not detect at the 2σ level and the CO (6–3) absorption at 1.62 μm, respectively. The grey-shaded regions indicate areas of significant telluric absorption.

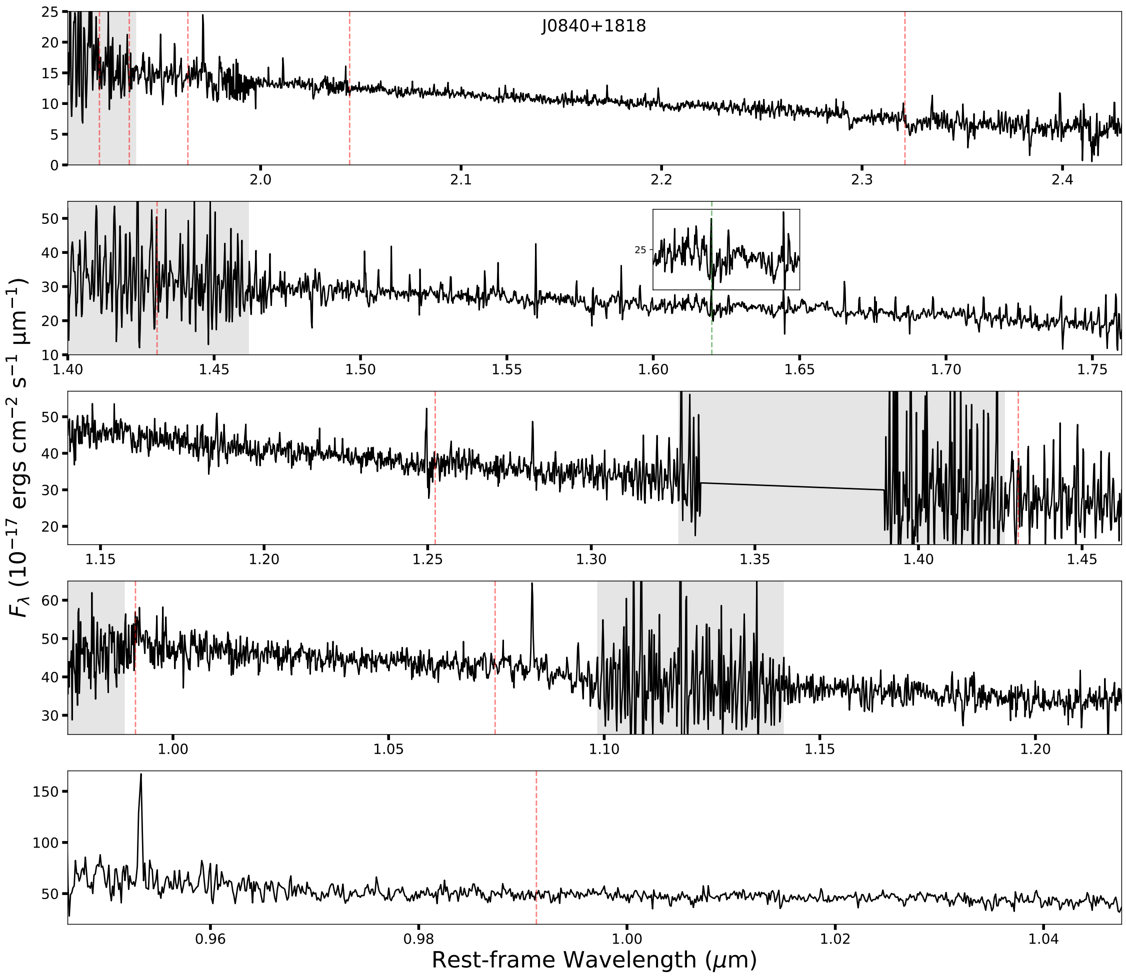

Figure 6.5: Same as Figure 6.4 but for J0840+1818.

6.4.4 J084234.50+031930.68

MK19 reported broad Hα J0842+0319, from which they calculated a BH mass of $\log(M_{\rm BH}/M_{\odot}) = 5.84$. MC20 reported both disturbed and stratified gas, which is consistent with the findings of L20 where they found blueshifted gas up to -160 km s^{-1}.

The NIR spectrum of J0842+0319 is shown in Figure 6.6 and line measurements are listed in Table 6.6. We detect [Ca VIII] as the only NIR CL in this object. To provide a more accurate measurement of the flux and width, we include simultaneous fits to the CO band absorption. Of the objects that show NIR CL emission, J0842+0319 has the lowest $L_{\rm AGN}$ and deepest CO(6-3) band absorption feature. Deeper observations may reveal other, more faint CLs. The rest of the spectrum shows a number of hydrogen recombination, H_2, and He I lines, and significant CN absorption is seen, suggesting an older stellar population.

6.4.5 J090613.75+561015.5

Reines & Volonteri (2015) reported a BH mass of $\log(M_{\rm BH}/M_{\odot}) = 5.40$, based on virial mass estimates. Marleau et al. (2017) also report a BH mass using bolometric luminosities from WISE IR data, from which they calculate $\log(M_{\rm BH}/M_{\odot}) = 6.93$. Baldassare et al. (2017a) reported bright X-ray emission, $L_{0.5-7{\rm keV}} = 4.47 \times 10^{40}$ erg s^{-1}, in Chandra data that is higher than what is expected from high-mass X-ray binaries. They concluded that AGN activity is the likely source of this X-ray emission. MC20 reported disturbed gas and three components were used in the fits done by L20. Maximum widths of the third component reach up 1250 km s^{-1}, the largest seen in the sample and is indicative of a fast outflow.

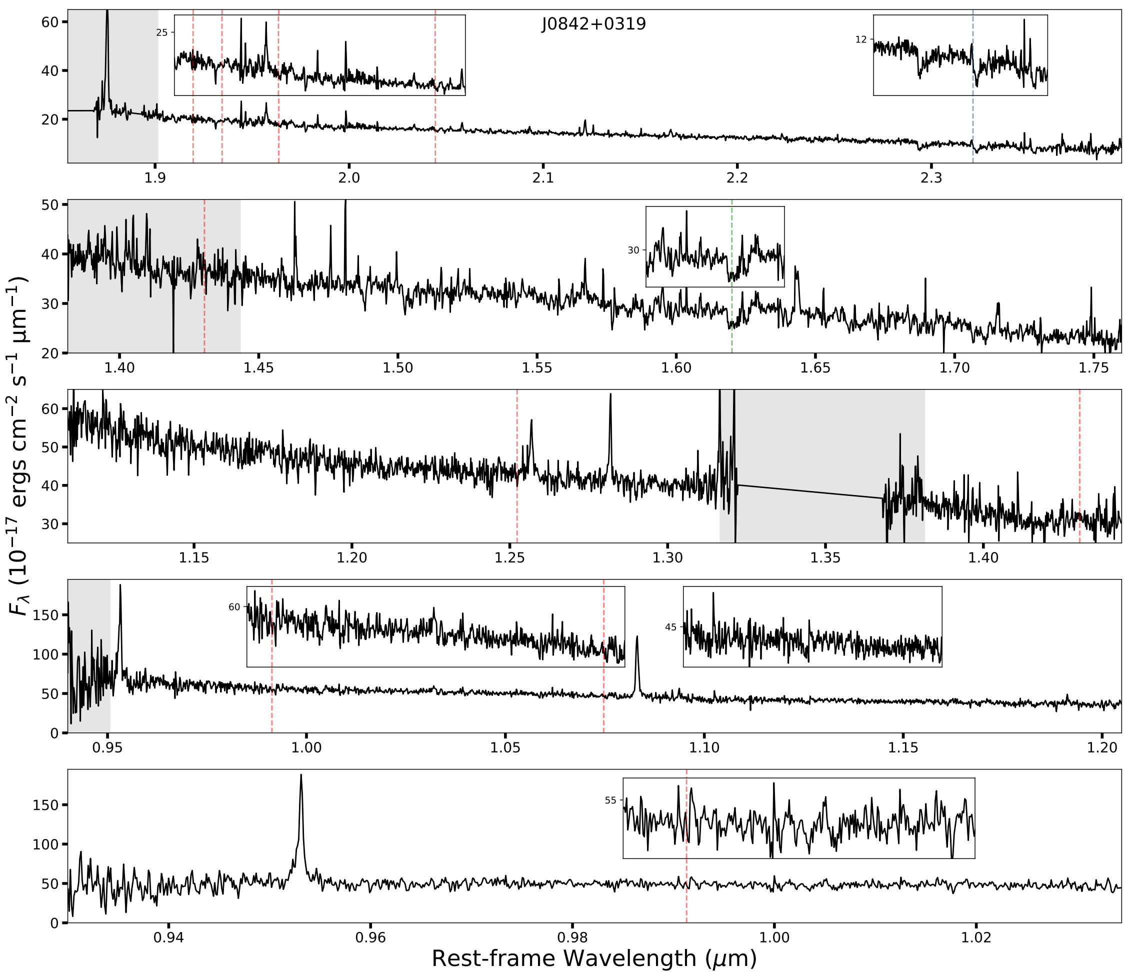

Figure 6.6: Same as Figure 6.4 but for J0842+1818. The blue-dashed line indicates a CL with a 2σ detection.

We also note that the C2 component of [O III] measured in L20 is redshifted 60 km s^{-1} relative to the systemic velocity. One explanation for this is that they are observing the far side of the outflow. Interestingly, this redshifted component is also seen in [Si VI], where it is offset by $\sim$90 km s^{-1}. Since the two values are consistent with each other, we are both likely observing the far side of the outflow.

The NIR spectrum of J0906+5610 is shown in Figure 6.7 and line measurements are listed in Table 6.7. The spectrum has an abundant number of emission lines, including strong hydrogen recombination, H_2, and He I lines. The CL emission is also strong, with significant emission from [Si VI], [S IX], and [Si X]. We also detect weaker emission from [S VIII] and [Ca VIII]. [Si VI] is best fit with two Gaussian components (see Figure 6.8) while only one Gaussian was necessary to fit the other CLs properly. It is noteworthy that [Si VI] falls within a region of telluric absorption and skylines. However, on closer inspection of the telluric standard star used, the degree of absorption is comparable to that seen redward at 1.98 μm. Thus, we expect the noise level around [Si VI] to be at similar levels. The skylines are also similar to those blueward and the effects can be seen in the residuals of the fit. Lastly, we do not detect CN absorption in the J band.

Inspection of the available optical data from SDSS, LRIS, GMOS, and KCWI yields a number of CLs. These include [Ne V] λ3426, [Fe VII] $\lambda\lambda\lambda$5721, 5159, 6087, and [Fe X] λ6374.

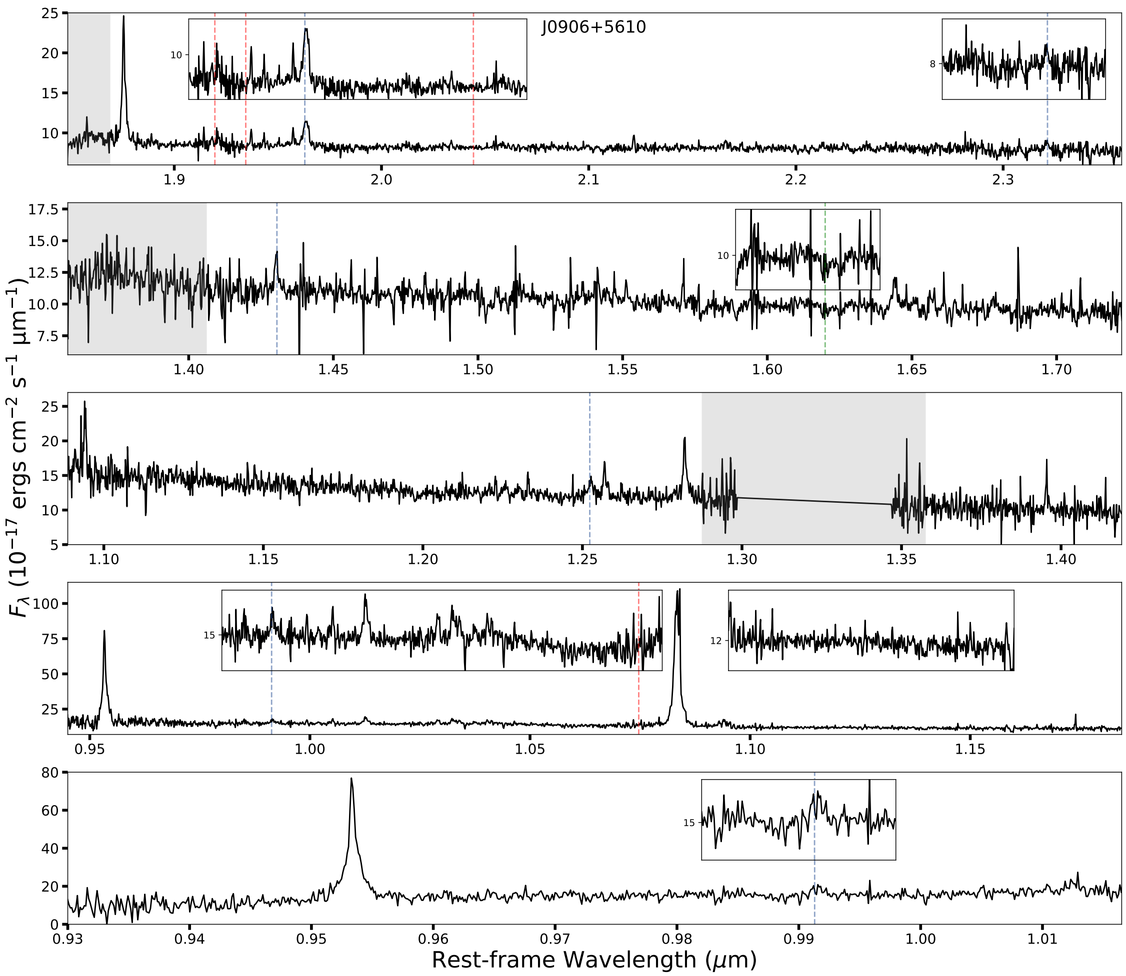

Figure 6.7: Same as Figure 6.4 but for J0906+5610.

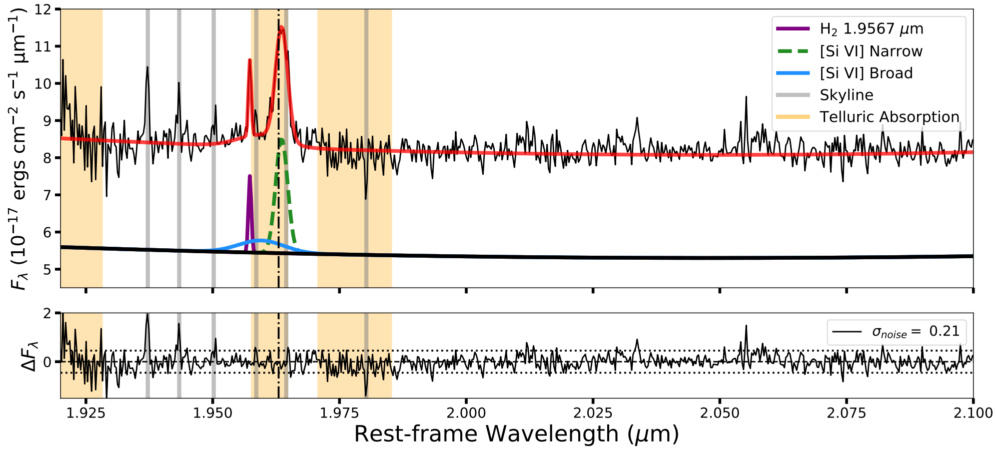

Figure 6.8: MCMC fit to [Si VI]1.9630 μm and $H_2$1.9576 μm emission for J0906. The spectrum is shifted to rest-frame wavelength using the systemic redshift. The purple line represents the fit to the H_2 emission, while the green-dotted and blue line fits represent the narrow and broad components of [Si VI]. The bottom panels show residuals to the fits and 1σ noise level (represented as dotted lines). The location of skylines and regions of telluric absorption near [Si VI] are represented as gray and and yellow lines, respectively. Note that running na F-test on these fits suggests that a two-component fit is needed.

6.4.6 J095418.16+471725.1

Both Reines & Volonteri (2015) and Marleau et al. (2017) reported a BH mass for J0954+4717. Using the methods described in Section 6.4.5, they reported $\log(M_{\rm BH}/M_\odot)$ equal to 5.00 and 6.46, respectively. Similar to J0906+5610, Baldassare et al. (2017a) also report strong X-ray emission, $L_{0.5-7\rm keV} = 9.77 \times 10^{39}$ erg s^{-1} that is likely coming from AGN activity. MC20 reported disturbed gas, and as shown in L20, three components were needed to properly describe the profile. Both of these indicate the presence of outflows.

The NIR spectrum of J0954+4717 is shown in Figure 6.9 and line measurements are listed in Table 6.8. Strong emission is seen in various hydrogen recombination, H_2, and He I lines. A large number of these emission lines require a multicomponent fit to properly match their profile, possibly due to the outflow. [Si VI], plotted in Figure 6.10, is the only strong CL. Inspecting the skyline immediately on top of [Si VI], we find it to be of similar strength to those redward. As shown in the bottom panel, the residuals at the locations of the skylines are comparable, leading us to believe our fit is representative of the emission. Evaluating the emission profile of [Si VI], we obtain an F-test value of $\sim$1.5 when adding a broad component. Although this is suggestive of the presence of broad emission, we cannot say for certain whether adding a broad component is justifiable. As such, we treat this as an upper limit to the broad flux and width.

In addition to [Si VI], we also detect two sulfur lines, [S VIII] and [S IX]. Similar to the other galaxies in our sample, we do not detect any CN absorption in the J band.

Like J0906+5610, inspection of the available optical data from SDSS, LRIS, GMOS, and KCWI yields a number of CLs. These include [Ne V] $\lambda\lambda$3346, 3426, [Fe V] λ3839, and [Fe VII] $\lambda\lambda$5159, 6087.

6.4.7 J100551.19+125740.6

Marleau et al. (2017) reported a BH mass of $\log(M_{\rm BH}/M_{\odot}) = 6.47$ and MC20 found disturbed gas in their optical data. Like J0811+2328, Wang et al. (2016) reported a $L_{0.3-8\rm keV}$ flux for J1005+1257, from which we obtain a $L_{2-10\rm keV}$ of 5.20×10^{39} erg s^{-1}. L20 fit three components to the [O III] emission line profile, and the broadest component, C3, have widths up to 1200 km s^{-1}. This is the second broadest they see in the sample and suggests the presence of a fast outflow.

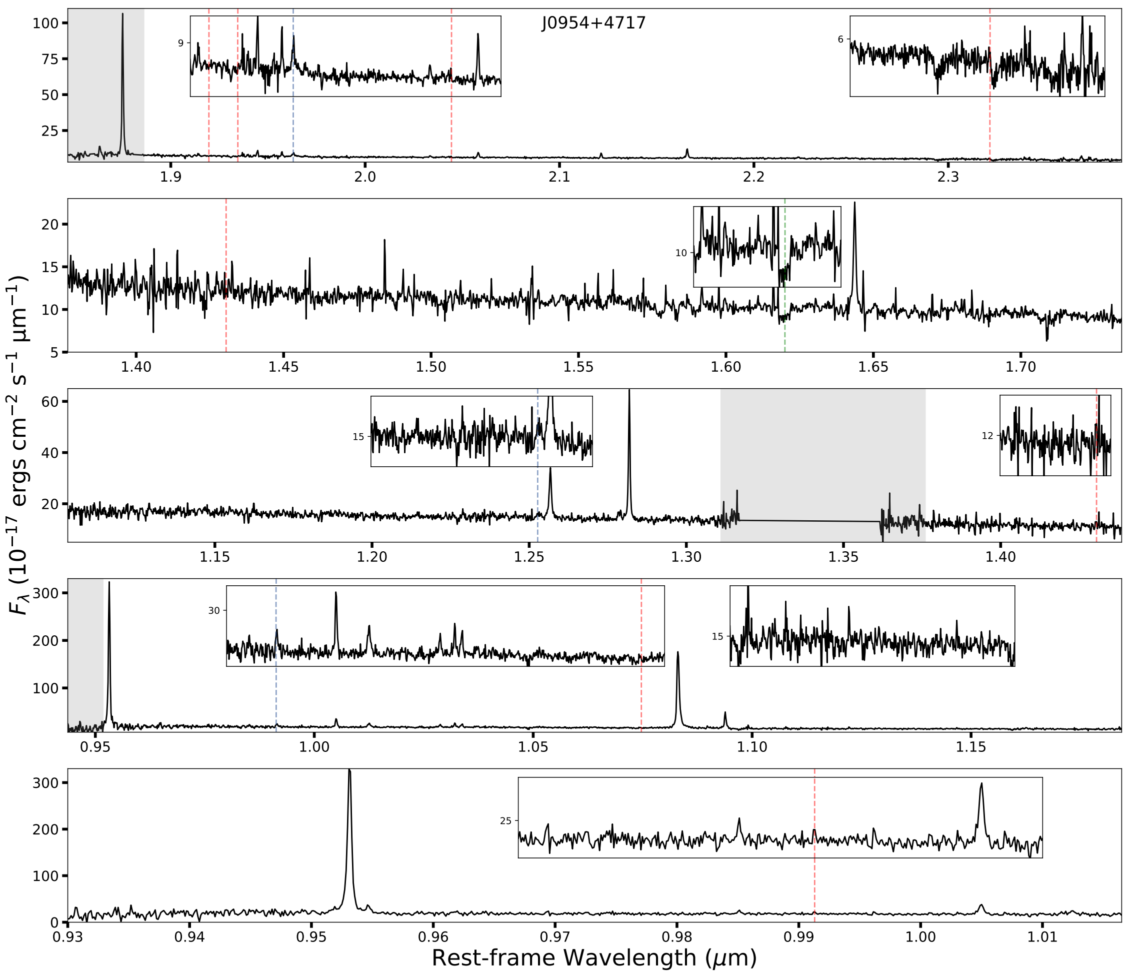

Figure 6.9: Same as Figure 6.4 but for J0954+4717.

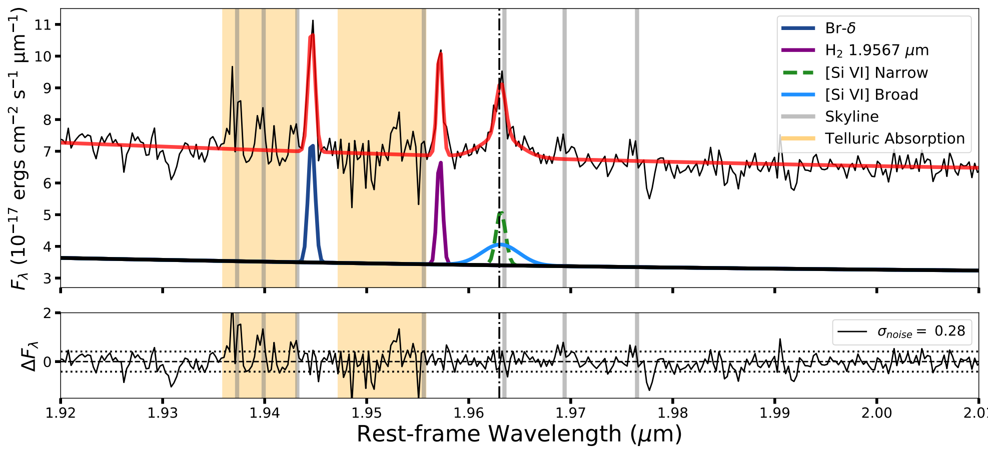

Figure 6.10: Same as Figure 6.8 but for J0954+4717. We additionally fit Brδ, represented as a cobalt-colored line.

The NIR spectrum of J1005+1257 is shown in Figure 6.11 and line measurements are listed in Table 6.9. Like the other galaxies with CL emission, its spectrum shows a wealth of strong emission lines. Of particular note is [Si VI], which shows a strong broad component (see Figure 6.12, right). Unfortunately, the emission falls in a number of small telluric absorption features, but they do not drastically alter the fit. The region that was most affected was the large telluric feature redward of the [Si VI] line. In order to not overestimate the [Si VI] emission, particularly the broad component, we masked out the entire telluric feature (as represented as the large yellow block) from the fit.

We also detect strong emission of [Si X] and [S IX], and weaker emission of [S VIII] and [Ca VIII]. We detect [Si X] in two NIRES orders and list both measurements. We select the values from order 5 since the S/N is higher and the measurements are less uncertain. Also, we do not detect any CN absorption in the J band.

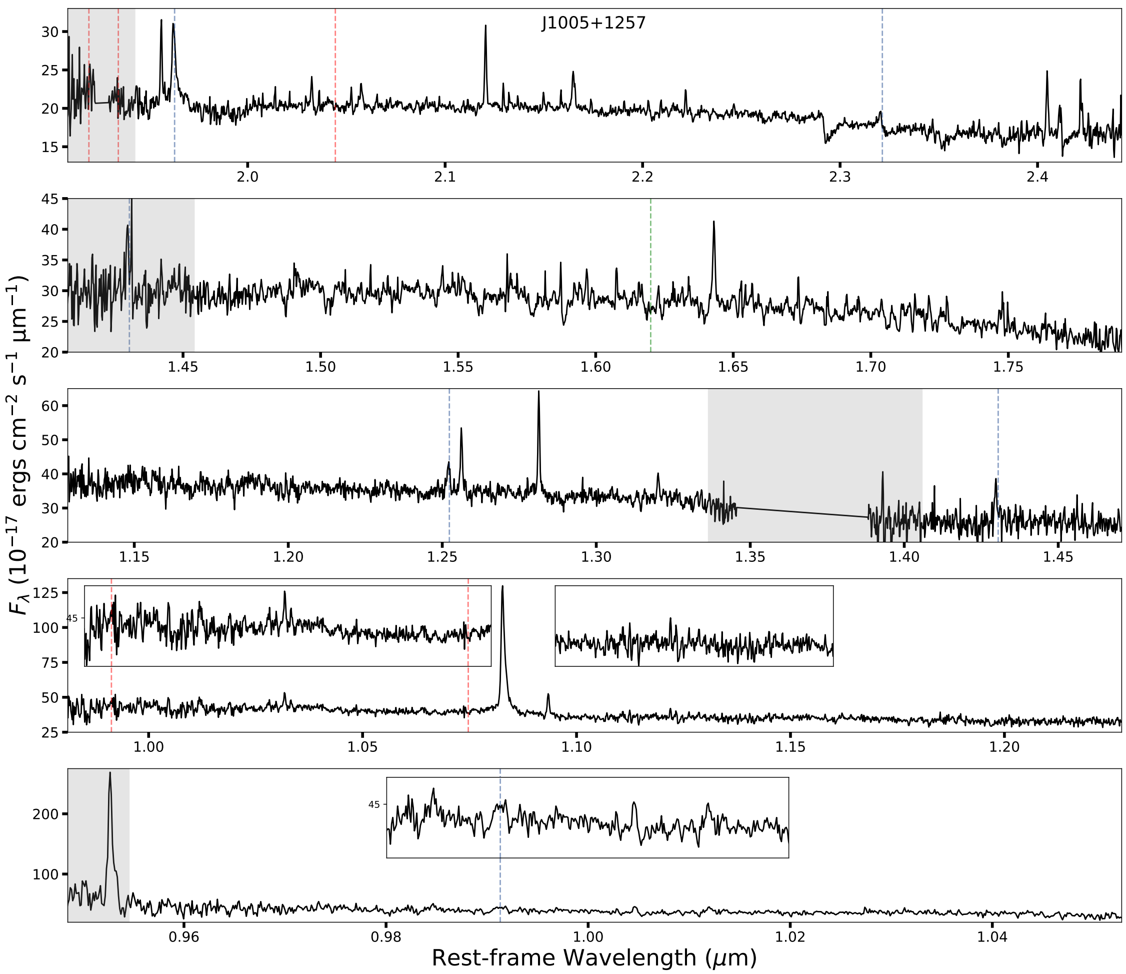

Figure 6.11: Same as Figure 6.4 but for J1005+1257.

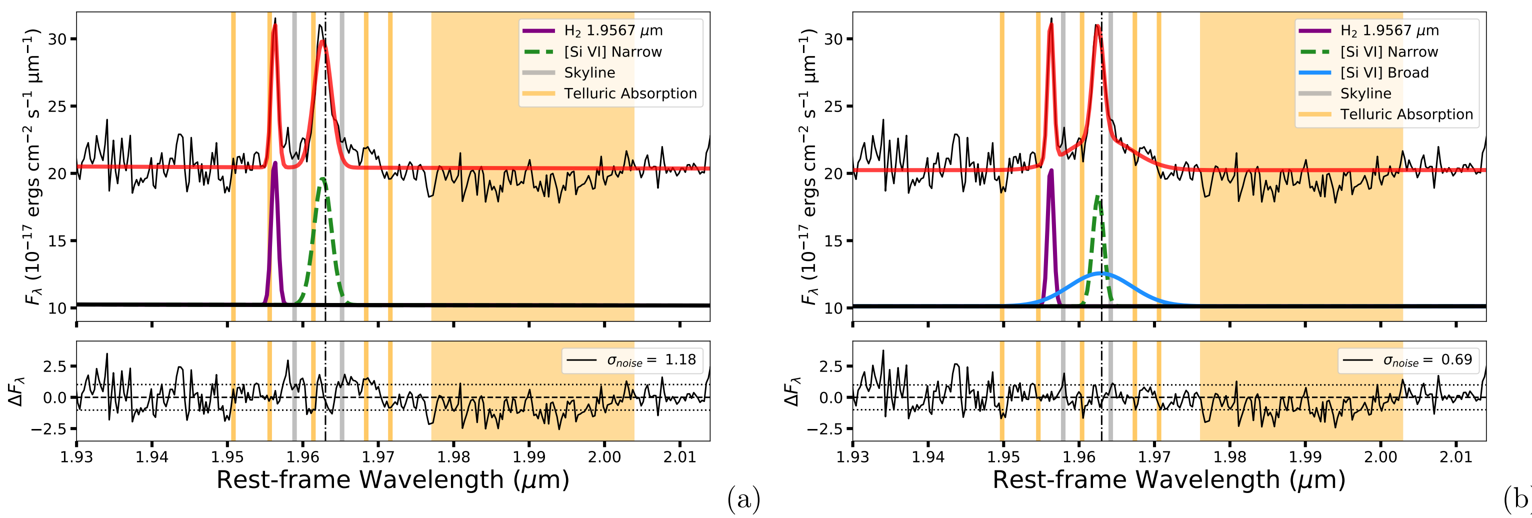

Figure 6.12: Same as Figure 6.8 but for J1005+1257. We plot a single-component fit (left) and a double-component fit (right). Note that running an F-test on these fits suggests that a two-component fit is needed.

Optical data reveal [Fe X] λ6374 emission and possible [Fe VII] λ5721 emission. The relative abundance of NIR CL emission and lack of optical CL emission is not surprising since J1005+1257 exhibits the highest extinction of our sample (see Table 3.2).

6.4.8 J100935.66+265648.9

Moran et al. (2014) provided an upper limit to the BH mass through Eddington luminosity arguments, $\log(M_{\rm BH}/M_{\odot}) > 5.1$. In addition, MC20 reported disturbed gas and a two-component fit was needed to properly fit the IFU data in L20. Due to the kinematic differences and velocity offsets between the C1 and C2 components, they suggested that the C2 component could represent a tilted, biconcial outflow, similar to that of J0100-0110.

The NIR spectrum of J1009+2656 is shown in Figure 6.13 and line measurements are listed in Table 6.10. Only one component is needed to properly fit [Si VI] (see Figure 6.14), this being the only case in our sample. Although there appears to be a red broad component, closer inspection of the standard star reveals telluric absorption in that region, which leads us to believe that it is due to a poorly corrected telluric feature. We also detect weak emission in [S VIII], [S IX], and [Ca VIII]. Lastly, we detect no CN absorption.

We also detect the optical CL [Ne V] λ3426, with other possible detections including [Fe VII] $\lambda\lambda$5721, 6087. Deeper observations will be needed to confirm these detections.

6.4.9 J144252.78+205451.67

J1442+2054 is one of two galaxies in our sample that falls in the composite region of the BPT diagram (see Manzano-King et al. (2019)). MC20 found both disturbed and

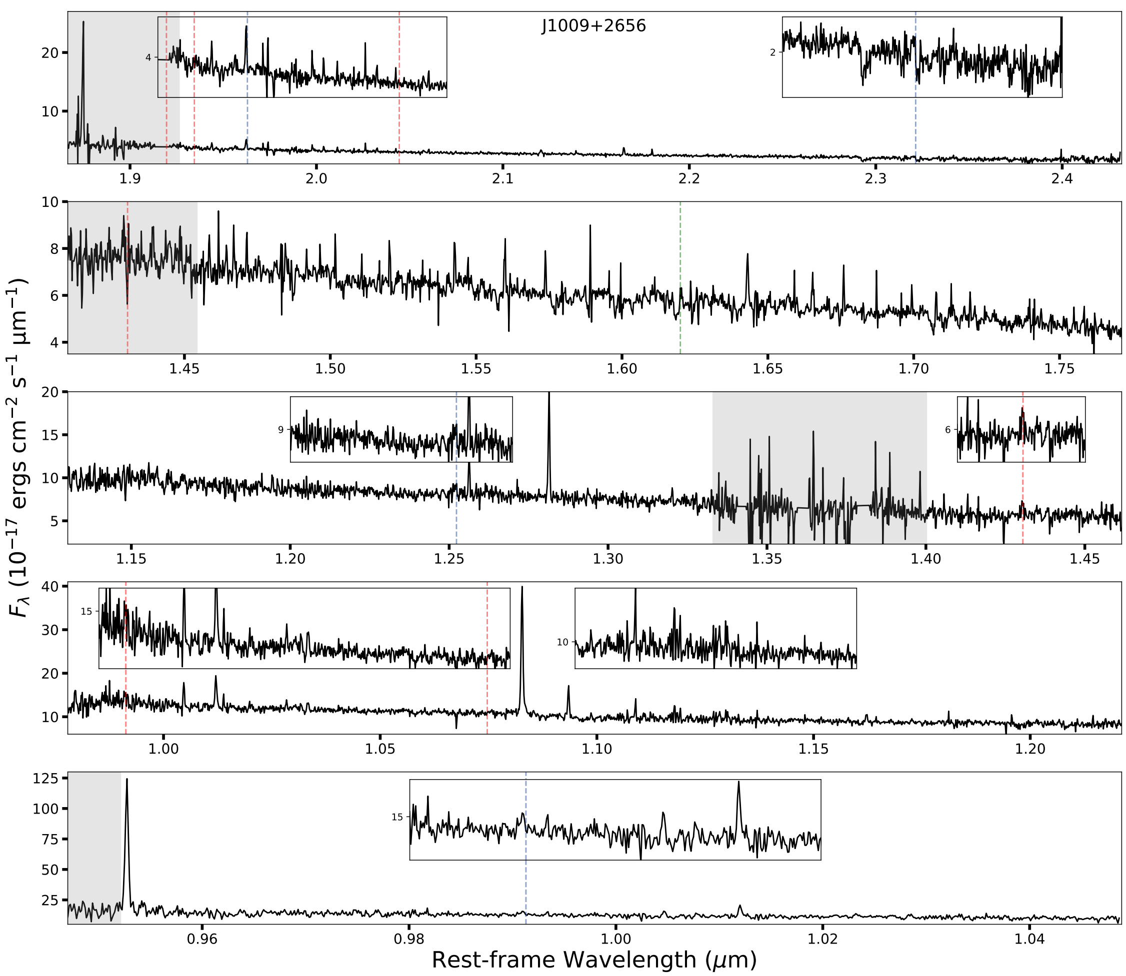

Figure 6.13: Same as Figure 6.4 but for J1009+2656.

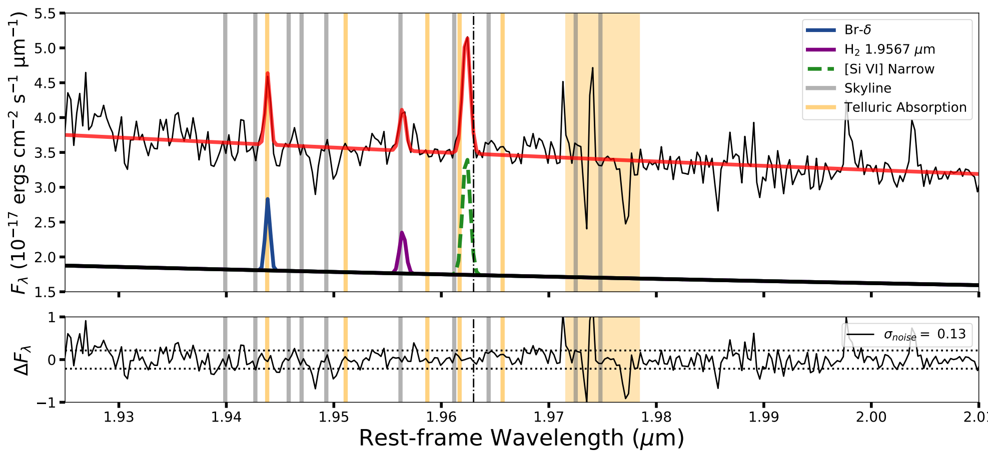

Figure 6.14: Same as Figure 6.10 but for J1009+2656. No broad component could be fit.

stratified gas in their optical data. This object was not observed in L20 and no BH mass has been reported to date.

The NIR spectrum of J1442+2054 is shown in Figure 6.15 and line measurements are listed in Table 6.11. The NIR is relatively featureless, with only a handful of typically strong emission lines appearing. We detect no CL emission (optical nor NIR) in this galaxy. We also do not detect any CN absorption.

Table 6.3: J0100 NIR Emission Line Parameters

Emission	FWHM (km s^{-1})	Flux (10^{-17} erg $cm^{-2}s^{-1}$)	Notes
Paα 1.8756 μm	62 ±7	141 ±6	Edge of wavelength coverage
Brγ 2.1661 μm	97 ±46	11 ±1	

Only NIRSPEC (K band) observations were done.
Columns: (1) Emission line. (2) FWHM of the emission line and its error after instrument correction. Uncertainties are only representative of random error in the fit. (3) Flux and error of the emission line, where uncertainties are from random errors. (4) Notes regarding the fitting.

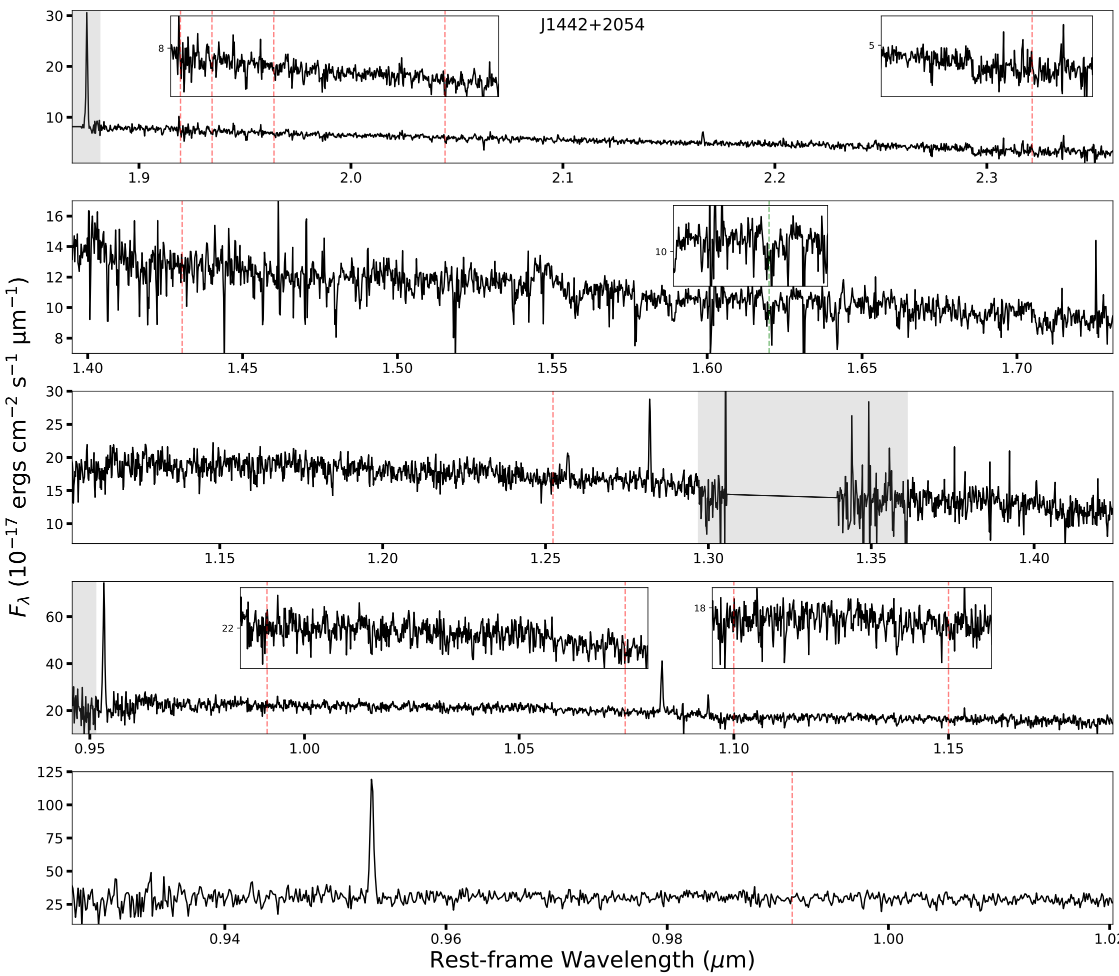

Figure 6.15: Same as Figure 6.4 but for J1442+2054.

Table 6.4: J0811 NIR Emission Line Parameters

Emission	FWHM (km s^{-1})	Flux (10^{-17} erg cm^{-2}s^{-1})	Notes
[S III] 0.9531 μm	173 ±9	153 ±26	Low transmission
He I 1.0830 μm Total	137 ±16	98 ±17	
[Fe II] 1.2486 μm	19^{+42}_{-19}	21 ±6	On skyline
[Fe II] 1.2567 μm	265 ±44	61 ±13	On skyline
Paβ 1.2822 μm	51 ±48	19 ±6	On skyline
[Fe II] 1.6435 μm	110 ±19	39 ±6	On skyline
H_2 2.1218 μm	66^{+32}_{-57}	11 ±2	
CO(6-3) 1.62 μm	386 ±81	—	Absorption feature

Same as Table 6.3. The CO(6-3) absorption feature at 1.62 μm is added at the bottom, along with the full-width half-minimum. The depth of the absorption feature measures about 13% of the continuum, suggesting roughly 65% of the H-band continuum comes from GMK red giants.

Table 6.5: J0840 NIR Emission Line Parameters

Emission	FWHM (km s^{-1})	Flux (10^{-17} erg cm^{-2}s^{-1})	Notes
[S III] 0.9531 μm	82 ±2	410 ±4	Low transmission
He I 1.0830 μm	89 ±4	109 ±2	
Paγ 1.0941 μm	10^{+19}_{-10}	32 ±2	Within telluric absorption
[Fe II] 1.2567 μm	43 ±31	28 ±4	On skyline
Paβ 1.2822 μm	3^{+34}_{-3}	57 ±4	On skyline
Brγ 2.1661 μm	152 ±140	11 ±5	
CO(6-3) 1.62 μm	518 ±126	—	Absorption feature, on skyline

Same as Table 6.4. The depth of the absorption feature measures about 14% of the continuum, suggesting roughly 70% of the H-band continuum comes from GMK red giants.

Table 6.6: J0842 NIR Emission Line Parameters

Emission	FWHM (km s^{-1})	Flux (10^{-17} erg cm^{-2}s^{-1})	Notes
[S III] 0.9531 μm Total	—	950 ±14	Order 7, $F > 2$
Narrow	62 ±3	341 ±8	Order 7
Broad	415 ±8	609 ±11	Order 7
[S III] 0.9531 μm Total	—	986 ±19	Order 6, low transmission, $F = 2$
Narrow	62 ±6	310 ±12	Order 6
Broad	350 ±6	677 ±15	Order 6
Paϵ 0.9549 μm	155 ±16	76 ±5	Order 7, blend with [S III]λ9531
Paϵ 0.9549 μm	171 ±15	103 ±6	Order 6, blend with [S III]λ9531
Paδ 1.0052 μm	48 ±34	24 ±3	Order 7
Paδ 1.0052 μm	77 ±60	24 ±4	Order 6
[S II] 1.0323 μm	299 ±40	71 ±7	
[S II] 1.0339 μm	71 ±40	20 ±4	
He I 1.0830 μm	200 ±6	618 ±13	
[Fe II] 1.2567 μm	280 ±46	159 ±16	
Paβ 1.2822 μm	127 ±12	152 ±28	Blue asymmetric tail
[Fe II] 1.6435 μm	269 ±27	152 ±12	On skyline
Paα 1.8756 μm	192 ±3	661 ±7	Within telluric absorption
H_2 1.9576 μm	165 ±21	84 ±7	
H_2 2.0338 μm	129 ±74	17 ±5	On skyline
He I 2.0587 μm	64 ±34	25 ±4	On skyline
H_2 2.1218 μm	82 ±13	53 ±3	
Brγ 2.1661 μm	136 ±29	30 ±4	
H_2 2.2235 μm	50 ±35	14 ±5	
[Ca VIII] 2.3214 μm	90 ±53	29 ±13	
CO(6-3) 1.62 μm	723 ±136	—	Absorption feature

Same as Table 6.4. The depth of the absorption feature measures about 13% of the continuum, suggesting roughly 65% of the H-band continuum comes from GMK red giants.

Table 6.7: J0906 NIR Emission Line Parameters

Emission	FWHM (km s^{-1})	Flux (10^{-17} erg $cm^{-2}s^{-1}$)	Notes
[S III] 0.9531 μm Total	—	710 ±6	Order 7, $F > 2$
Narrow	104 ±3	168 ±4	Order 7
Broad	657 ±9	542 ±5	Order 7
[S III] 0.9531 μm Total	—	694 ±16	Order 6, low transmission, $F > 2$
Narrow	88 ±8	163 ±10	Order 6
Broad	630 ±25	531 ±12	Order 6
[S VIII] 0.9913 μm	277 ±20	32 ±2	Order 7, on skyline
[S VIII] 0.9913 μm	381 ±77	29 ±9	Order 6, on skyline
Paδ 1.0052 μm	92 ±29	15 ±2	Order 6
He II 1.0126 μm	306 ±73	42 ±8	
[S II] 1.0289 μm	206 ±71	21 ±5	On skyline
[S II] 1.0323 μm	350 ±122	35 ±9	Blend with [S II] 1.0339 μm
[S II] 1.0339 μm	235.16 ±127.78	16 ±8	Blend with [S II] 1.0323 μm
[N I] 1.0400 μm	151 ±77	15 ±5	
He I 1.0830 μm Total	—	1660 ±45	On skyline, within telluric absorption, $F > 2$
Narrow	394 ±5	1260 ±33	
Broad	1081 ±81	401 ±31	
[S IX] 1.2523 μm	299 ±53	31 ±4	
[Fe II] 1.2567 μm	199 ±23	44 ±3	On skyline
Paβ 1.2822 μm	282 ±27	102 ±6	On skyline
[Si X] 1.4305 μm	309 ±58	46 ±6	
[Fe II] 1.6435 μm	344 ±57	44 ±5	On skyline
Paα 1.8756 μm Total	—	300 ±19	On skyline, $F > 2$
Narrow	71 ±30	66 ±13	
Broad	440 ±37	234 ±14	
H_2 1.9576 μm	63 ±36	15 ±2	On skyline
[Si VI] 1.9630 μm Total	—	127 ±15	On skyline, within telluric absorption, $F > 2$
Narrow	424 ±29	92 ±7	
Broad	1683 ±479	35 ±13	
H_2 2.0338 μm	97 ±44	7 ±1	
H_2 2.1218 μm	81 ±42	14 ±3	
Brγ 2.1661 μm	174 ±34	13 ±3	
[Ca VIII] 2.3214 μm	397 ±131	33 ±8	
CO(6-3) 1.62 μm	508 ±135	—	Absorption feature, on skyline

Same as Table 6.4. The depth of the absorption feature measures about 10% of the continuum, suggesting roughly 50% of the H-band continuum comes from GMK red giants.

Table 6.8: J0954 NIR Emission Line Parameters

Emission	FWHM (km s^{-1})	Flux (10^{-17} erg cm^{-2}s^{-1})	Notes
[S III] 0.9531 μm Total	—	1719 ±75	Order 7, $F > 2$
Narrow	87 ±2	1251 ±56	Order 7
Broad	530 ±36	468 ±46	Order 7
[S III] 0.9531 μm Total	—	1736 ±74	Order 6, $F > 2$
Narrow	73 ±2	1147 ±60	Order 6
Broad	401 ±21	590 ±43	Order 6
Paϵ 0.9549 μm	75 ±24	52 ±10	Order 7, blend with [S III]λ9531
Paϵ 0.9549 μm	129 ±42	64 ±13	Order 6
[C I] 0.9853 μm	75 ±45	24 ±8	Order 7, on skyline
[S VIII] 0.9913 μm	109 ±30	30 ±5	Order 6
Paδ 1.0052 μm	119 ±10	108 ±8	Order 7, on skyline
Paδ 1.0052 μm	102 ±12	89 ±8	Order 6, on skyline
He II 1.0126 μm	194 ±23	56 ±6	
[S II] 1.0289 μm	128 ±44	28 ±7	
[S II] 1.0323 μm	80 ±28	38 ±7	
[S II] 1.0339 μm	128 ±29	37 ±7	
He I 1.0830 μm Total	—	1391 ±44	Red asymmetric tail, $F > 2$
Narrow	152 ±5	1065 ±35	
Broad	805 ±61	325 ±26	
Paγ 1.0941 μm	96 ±7	162 ±10	On skyline
[S IX] 1.2523 μm	387 ±116	24 ±9	On skyline
[Fe II] 1.2567 μm Total	—	197 ±57	On skyline, $F = 2$
Narrow	125 ±19	102 ±39	
Broad	400 ±124	95 ±42	
Paβ 1.2822 μm Total	—	342 ±53	On skyline, $F > 2$
Narrow	59 ±18	186 ±40	
Broad	252 ±64	157 ±35	
[Fe II] 1.6435 μm Total	—	150 ±21	On skyline, $F > 2$
Narrow	114 ±16	90 ±15	
Broad	440 ±115	61 ±15	
Paα 1.8756 μm Total	—	952 ±36	Within telluric absorption, $F > 2$
Narrow	63 ±5	655 ±27	
Broad	309 ±30	298 ±24	
Brδ 1.9451 μm	83 ±11	33 ±2	Within telluric absorption
H_2 1.9576 μm	64 ±28	25 ±3	
[Si VI] 1.9630 μm Total	—	53 ±11	On skyline, $F \sim 1.5$
Narrow	142 ±54	19 ±7	
Broad	687 ±164	35 ±8	
H_2 2.0338 μm	117 ±29	11 ±2	
He I 2.0587 μm	111 ±8	35 ±2	
H_2 2.0735 μm	105 ±60	4 ±2	
H_2 2.1218 μm	71 ±12	28 ±2	
Brγ 2.1661 μm Total	—	79 ±10	$F > 2$
Narrow	60 ±19	45 ±7	
Broad	374 ±94	35 ±7	
H_2 2.2235 μm	160 ±39	12 ±2	
CO(6-3) 1.62 μm	553 ±63	—	Absorption feature

Same as Table 6.4. The depth of the absorption feature measures about 11% of the continuum, suggesting roughly 55% of the H-band continuum comes from GMK red giants.

Table 6.9: J1005 NIR Emission Line Parameters

Emission	FWHM (km s^{-1})	Flux (10^{-17} erg $cm^{-2}s^{-1}$)	Notes
[S III] 0.9531 μm	144 $\pm$4	2504 $\pm$220	Low transmission, red asymmetric tail
[C I] 0.9853 μm	215 $\pm$18	134 $\pm$15	
[S VIII] 0.9913 μm	299 $\pm$9	142 $\pm$14	On skyline
Paδ 1.0052 μm	77 $\pm$5	74 $\pm$8	Order 7
He II 1.0126 μm	173 $\pm$53	105 $\pm$30	Order 7
He II 1.0126 μm	202 $\pm$36	102 $\pm$22	Order 6
[S II] 1.0289 μm	185 $\pm$45	66 $\pm$15	
[S II] 1.0323 μm	145 $\pm$20	134 $\pm$19	On skyline
[S II] 1.0339 μm	109 $\pm$36	59 $\pm$13	
He I 1.0830 μm Total	—	2433 $\pm$194	On skyline, $F > 2$
Narrow	243 $\pm$5	1458 $\pm$96	
Broad	1337 $\pm$89	976 $\pm$117	
Paγ 1.0941 μm	130 $\pm$11	179 $\pm$19	
[S IX] 1.2523 μm	256 $\pm$38	160 $\pm$25	
[Fe II] 1.2567 μm	169 $\pm$17	251 $\pm$26	On skyline
Paβ 1.2822 μm	133 $\pm$9	348 $\pm$28	
[Fe II] 1.3208 μm	143 $\pm$6	92 $\pm$6	On skyline
[Si X] 1.4305 μm	162 $\pm$4	164 $\pm$8	Order 5, within telluric absorption
[Si X] 1.4305 μm	156 $\pm$18	168 $\pm$20	Order 4, within telluric absorption
[Fe II] 1.6435 μm	157 $\pm$17	188 $\pm$17	
H_2 1.9576 μm	114 $\pm$11	135 $\pm$11	Within telluric absorption
[Si VI] 1.9630 μm Total	—	491 $\pm$31	On skyline, within telluric absorption, $F > 2$
Narrow	246 $\pm$14	193 $\pm$16	
Broad	1376 $\pm$114	298 $\pm$27	
H_2 2.0338 μm	106 $\pm$35	43 $\pm$8	
He I 2.0587 μm	202 $\pm$56	47 $\pm$10	
H_2 2.1218 μm	121 $\pm$7	137 $\pm$7	
Brγ 2.1661 μm	208 $\pm$19	95 $\pm$8	On skyline
H_2 2.2235 μm	55 $\pm$35	28 $\pm$6	
[Ca VIII] 2.3214 μm	291 $\pm$129	48 $\pm$18	
H_2 2.4066 μm	104 $\pm$18	104 $\pm$12	
CO(6-3) 1.62 μm	778 $\pm$232	—	Absorption feature

Same as Table 6.4. The depth of the absorption feature measures about 7% of the continuum, suggesting roughly 35% of the H-band continuum comes from GMK red giants.

Table 6.10: J1009 NIR Emission Line Parameters

Emission	FWHM (km s^{-1})	Flux (10^{-17} erg cm^{-2}s^{-1})	Notes
[S III] 0.9531 μm	83 $\pm$1	507 $\pm$20	Order 7
[S III] 0.9531 μm	128 $\pm$2	552 $\pm$26	Order 6, low transmission
Paϵ 0.9549 μm	125 $\pm$7	47 $\pm$4	Order 7
[S VIII] 0.9913 μm	145 $\pm$40	17 $\pm$4	Order 7
Paδ 1.0052 μm	44 $\pm$17	14 $\pm$2	Order 7
Paδ 1.0052 μm	26 $\pm$21	23 $\pm$3	Order 6
He II 1.0126 μm	67 $\pm$22	39 $\pm$6	Order 7
He II 1.0126 μm	114 $\pm$13	44 $\pm$4	Order 6
[S II] 1.0339 μm	92 $\pm$37	9 $\pm$3	
He I 1.0830 μm	116 $\pm$3	189 $\pm$8	Red asymmetric tail, $F < 2$
Paγ 1.0941 μm	71 $\pm$30	35 $\pm$7	
He I 1.1629 μm	106 $\pm$45	22 $\pm$3	
[S IX] 1.2523 μm	269 $\pm$90	11 $\pm$3	On skyline
[Fe II] 1.2567 μm	71 $\pm$16	22 $\pm$2	On skyline
Paβ 1.2822 μm	83 $\pm$6	68 $\pm$2	
[Fe II] 1.6435 μm	83 $\pm$22	18 $\pm$2	
Paα 1.8756 μm	86 $\pm$2	197 $\pm$7	Within telluric absorption
Brδ 1.9451 μm	INDEF	6 $\pm$1	Within telluric absorption, width < telescope spectral resolution
H_2 1.9576 μm	76 $\pm$34	5 $\pm$1	On skyline
[Si VI] 1.9630 μm	99 $\pm$15	17 $\pm$1	Adjacent to skyline
H_2 2.0338 μm	48^{+26}_{-48}	5 $\pm$1	
He I 2.0587 μm	117 $\pm$70	4 $\pm$1	
H_2 2.1218 μm	128 $\pm$26	8 $\pm$1	On skyline
Brγ 2.1661 μm	63 $\pm$22	12 $\pm$1	
[Ca VIII] 2.3214 μm	323 $\pm$79	12 $\pm$6	
CO(6-3) 1.62 μm	237 $\pm$39	—	Absorption feature

Same as Table 6.4. The depth of the absorption feature measures about 11% of the continuum, suggesting roughly 55% of the *H*-band continuum comes from GMK red giants.

Table 6.11: J1442 NIR Emission Line Parameters

Emission	FWHM (km s^{-1})	Flux (10^{-17} erg cm^{-2}s^{-1})	Notes
[S III] 0.9531 μm	88 $\pm$2	435 $\pm$29	Order 7
[S III] 0.9531 μm	115 $\pm$2	315 $\pm$20	Order 6, low transmission
He I 1.0830 μm	115 $\pm$9	138 $\pm$12	In telluric absorption
Paγ 1.0941 μm	24 $\pm$2	36 $\pm$6	In telluric absorption
[Fe II] 1.2567 μm	134 $\pm$51	33 $\pm$8	
Paβ 1.2822 μm	86 $\pm$15	83 $\pm$9	
[Fe II] 1.6435 μm	137 $\pm$65	17 $\pm$5	
Paα 1.8756 μm	93 $\pm$4	203 $\pm$7	On skyline, in telluric absorption
He I 2.0587 μm	103 $\pm$60	8 $\pm$2	
Brγ 2.1661 μm	75 $\pm$26	21 $\pm$3	
H_2 2.2477 μm	115 $\pm$43	12 $\pm$2	
CO(6-3) 1.62 μm	446 $\pm$133	—	Absorption feature, on skyline

Same as Table 6.4. The depth of the absorption feature measures about 11% of the continuum, suggesting roughly 55% of the *H*-band continuum comes from GMK red giants.

6.5 NIR Line Fluxes

In this section, we list fluxes of the NIR emission lines detected at the 3σ level or greater for each target. Note that fluxes are omitted if the emission has insufficient signal-to-noise, fall in heavy telluric absorption, or are outside the wavelength coverage. All fluxes are in units of 10^{-17} erg s^{-1}.

6.6 Additional Details on Individual Objects

6.6.1 J012218.11+010025.76

J0122+0100 is a dual system that is likely undergoing a merger event. Optical and NIR spectroscopy identify three sources, two in the east component (NE and SE) and one in the west. The two east sources are separated about 1.9" (2.1 kpc). Optical line ratios place all three sources in the star-forming region of the BPT diagram. NIR line ratios of the southeast and west sources, likely the nuclei of the two galaxies, also lie within the scatter of star-forming galaxies in the NIR diagnostic diagrams of Osterbrock et al. (1992). Indeed, these sources show prominent H I recombination, He I, and H_2 emission lines. In Paα, spatially extended gas emission is seen in the East component. It extends northwards by about 3.65" (3.9 kpc) and has receding velocities. Due to the asymmetry of the emission, it is likely a result of the interaction between the two galaxies.

While we do not detect any CLs in any of the three sources in our observations, Satyapal et al. (2017) report a 4σ detection of [Si VI] in the southeast source based on LBT LUCI-1 spectroscopy. Close inspection of the acquisition image reveals three sub-

Table 6.12: NIR Line Fluxes

Line	J0122ne	J0122se	J0122w	J0333	J0750	J0851	J0852	J0929
[S III] 0.9069 μm	36 ±4	119 ±10	171 ±11	—	—	33 ±16	149 ±35	152 ±30
[S III] 0.9531 μm	74 ±8	361 ±18	577 ±19	—	—	57 ±18	387 ±23	550 ±40
Paϵ 0.9549 μm	—	27 ±3	51 ±3	—	—	—	—	—
Paδ 1.0052 μm	9 ±1	34 ±4	58 ±3	—	—	—	—	—
He I 1.0830 μm	—	—	—	—	—	—	135 ±20	237 ±42
Paγ 1.0941 μm	—	—	—	—	—	—	20 ±2	62 ±4
P II 1.1880 μm	—	—	12 ±2	—	—	—	36 ±7	—
Fe II 1.2567 μm	12 ±0.7	33 ±2	58 ±3	—	—	—	184 ±12	—
Paβ 1.2822 μm	—	—	—	—	—	—	—	43 ±3
Fe II 1.6435 μm	7 ±0.9	28 ±2	38 ±2	—	—	—	57 ±4	—
Paα 1.8756 μm	89 ±4	288 ±9	514 ±17	41 ±3	69 ±11	168 ±18[a]	87 ±3	427 ±44
Brδ 1.9451 μm	4 ±1	18 ±1	27 ±2	—	—	—	—	—
H_2 1.9576 μm	3 ±1	7 ±1	15 ±2	—	—	—	5 ±2	17 ±4
Si VI 1.9630 μm	—	—	—	—	—	—	69 ±9[a]	392 ±102
H_2 2.0338 μm	2 ±0.5	4 ±1	7 ±2	—	—	—	—	—
He I 2.0587 μm	4 ±1	18 ±2	21 ±4	—	—	—	—	—
H_2 2.1218 μm	4 ±1	9 ±1	17 ±1	—	—	—	11 ±2	—
Brγ 2.1661 μm	8 ±1	31 ±1	38 ±1	—	—	—	—	13 ±3
H_2 2.2235 μm	—	3 ±0.5	5 ±1	—	—	—	—	—

Line	J0122ne	J0122se	J0122w	J0333	J0750	J0851	J0852	J0929
[S III] 0.9069 μm	14 ±6	—	37 ±28	16 ±5	—	32 ±7	6 ±2	
[S III] 0.9531 μm	34 ±6	—	58 ±39	39 ±6	—	65 ±12	26 ±8	
Paϵ 0.9549 μm	—	—	—	—	—	—	—	
He I 1.0830 μm	32 ±7	—	78 ±40	12 ±2	—	46 ±6	22 ±7	
Paγ 1.0941 μm	6 ±1	—	15 ±9	3 ±1	—	—	—	
P II 1.1880 μm	—	—	—	—	—	—	—	
Fe II 1.2567 μm	—	—	—	4 ±1	—	—	—	
Paβ 1.2822 μm	—	—	89 ±50	—	—	8 ±3	8 ±3	
Fe II 1.6435 μm	—	—	—	3 ±1 (2 ±0.6)	—	—	—	
Paα 1.8756 μm	33 ±3	—	125 ±42[a]	19 ±2	72 ±20	46 ±3	43 ±5	
Brδ 1.9451 μm	—	345 ±19	—	—	—	—	—	
H_2 1.9576 μm	—	987 ±56	—	3 ±1	39 ±14	7 ±1	7 ±2	
Si VI 1.9630 μm	—	—	—	(2 ±0.3)	—	18 ±2	24 ±6	
H_2 2.0338 μm	—	398 ±19	—	—	—	—	—	
He I 2.0587 μm	—	393 ±19	—	—	—	—	—	
H_2 2.1218 μm	—	1049 ±29	—	3 ±0.6 (1 ±0.3)	—	—	4 ±1	
Brγ 2.1661 μm	—	714 ±25	—	2 ±0.8 (2 ±0.6)	—	—	—	
H_2 2.2235 μm	—	310 ±16	—	—	—	—	—	

[a] Includes both broad and narrow component fluxes

NOTE: All fluxes are in units of 10^{-17} erg s^{-1}. J1036 also has emission lines with the following fluxes: H_2 2.0735 μm (106 ±14) and H_2 2.2477 μm (182 ±15).

components in the eastern target. Due to the smaller width of the NIRES slit (0.55", compared to 1.0" of LUCI), we could have missed this third component since it is not aligned with the other two (∼0.4" offset).

Chandra and *XMM-Newton* X-ray observations are also reported for both the east and west sources (Satyapal et al., 2017; Pfeifle et al., 2019). The observed X-ray luminosities are above those expected by stellar processes, such as XRBs. Coupled with the high extinction found in these targets, these results point to an optically obscured dual AGN system.

6.6.2 J033331.86+010716.92

J0333+0107 was observed under heavy cloud cover and only K-band data have sufficient S/N for proper analysis. As such, this could severely effect the detections of any weak CLs. The high extinction, E(B-V) = 1.38, could also play a role in the lack of CL detections. Our slit position for this target is misaligned ∼15° from the semi-major axis. As such, the rotational velocities in Figure 4.6 could be underestimated.

6.6.3 J085153.64+392611.76

J0851+3926 is one of two galaxies for which we report a BH mass through virial mass estimators using broad Paα (see Section 4.4.2 and 4.6). Here, the broad Paα is detected while no clear indication of optical broad lines are seen in the SDSS spectra. We can use this broad emission (or lack thereof) to calculate estimates to extinction in the central regions. To do this, we fit the SDSS spectrum incorporating a broad component to Hα. A check of the F-test ($F = (\sigma_{single})^2/(\sigma_{double})^2$) results in $F = 1.41$, too low to justify adding the component. As such, we will consider these measurements as upper limits. Fits to the spectra give a line ratio of Paα/H$\alpha \geq 1.44$. Assuming an electron density of $n_e = 10^8$ cm^{-3} and temperature $T_e = 15{,}000$ K, we use the intrinsic line ratio Paα/H$\alpha = 0.10$ as derived in Dopita & Sutherland (2003). This results in an E(B-V) $\geq$ 1.40, higher than the extinction measured using the Hα/Hβ Balmer decrement. This extinction is comparable to that of other targets that do not show any CLs, suggesting that obscuration could be inhibiting CL detection in this target.

As discussed in Section 4.7, inspection of gas emission in J0851+3926 shows counter-rotation within the central kpc. This asymmetry is not seen in the slit perpendicular to this, which could indicate the presence of a bar along the semi-major axis (Bohn et al., 2020). Analysis of SDSS imaging seems to confirm this, but higher resolution imaging is required. Another scenario to create the observed counter-rotation is through tidal disruptions induced by a flyby of a companion galaxy (see SDSS postage stamp in Figure 4.6). However, the spectroscopic redshift of this companion could not be obtained and its photometric redshift does not match with J0851+3926. If the photometric redshifts are accurate, this would indicate the companion is a background galaxy. Surface brightness decompositions of J0851+3926 seems to confirm this, since no significant asymmetries in the disk appear and thus it is largely intact. Regardless of the scenario, it is likely through these processes that gas can be funneled to the central regions to allow BH growth without the need of major mergers or the build-up of the central bulge.

6.6.4 J092907.78+002637.29

The velocity profile of the gas in J092907.78+002637.29 is quite unique since it is significantly asymmetric. We see receding gas that roughly matches the NFW curve, though it is somewhat 'core-like'. We see zero net velocity in the gas emission on the approaching side. A number of factors could be the cause of this, but due to the low resolution of available imaging, we can only provide speculative scenarios. The simplest reasoning is that the rotating gas did not fall within the slit, however this is unlikely since the slit covers most of the semi-major axis. A more plausible scenario is that a dust plane is obscuring the rotating gas and that we are only observing gas moving perpendicular to us. This is consistent with the extinction seen in this target, E(B-V) = 1.28, one of the highest of targets with rotation curves.

Considering the asymmetry in the profile, the possibility of the outflow or a merger event altering the gas rotation cannot be dismissed. While we detect a fast outflow in J0929+0026, the associated gas emission is blueshifted and is inconsistent with the rotation curve. If we assume a bi-conical model (Bae & Woo, 2016), we would also expect the receding gas to be more heavily obscured by the galactic disk. Lastly, while surface brightness decompositions do not show a significant merger event occurring, higher resolution imaging will be needed to confirm if a minor merger is occurring.

6.6.5 J103631.88+022144.10

HST imaging reveals J1036+0221 is likely a merger system. Our NIR data show rotational H_2 (2.0338, 2.1218 μm), He I 2.0587 μm, and Brγ gas emission within the central

$\sim$2 kpc that peaks $\sim$ 200 km s^{-1}. We suspect that this rotation is due largely to tidal disruptions of the merger.

Our NIRSPEC spectra, in which only K-band is observed, do not show any CLs. However, Satyapal et al. (2017) obtained LBT LUCI-1 spectra, through which the coverage is extended to H-band. They detect [Si X] 1.4305 μm at the 4σ level. NIR line ratio diagnostics (see Section 4.4.3) places this galaxy within the scatter of other AGN, further suggesting the presence of an AGN in the nucleus. They also detect a strong X-ray source, which further indicates AGN activity in this merger.

6.6.6 J122809.19+581431.40

SDSS imaging shows evidence of two central sources in J1228+5814. This is confirmed with GALFIT where two exponential disks best fit the surface brightness profile. Indeed, two sources are also seen in the 2D spectrum. However, we only detect hidden broad Paα emission in the south source (see Section 4.4.2). Inspection of the north source reveals a featureless spectrum, except for a few stellar absorption features in H-band. This is, however, enough to confirm that there is no significant velocity offset between the two sources. It is possible that we are viewing this target in the advanced stages of a merger.

Along with J1326+1014, this target also has one of the highest extinction levels in this sample, E(B-V) = 2.50. This is largely due to the weak Hβ emission that indicates significant obscuration. For J1228+5814, this is consistent with the fact that no broad Hα emission is detected in the SDSS spectra. This high level of obscuration is likely inhibiting CL detection.

6.7 Rotation Curves Extraction

We obtained velocities at various radii by first fitting a Gaussian along the spatial axis of the rectified 2D spectrum to locate the center of the galaxy. The row with the highest pixel value was taken as the center and used as the zero-point from which we constructed velocity curves. If multiple rows in the central region had comparable pixel values, we took the pixel pair with the highest values as the center. Note that this method selects the photometric peak and not necessarily the kinematic center of the galaxy.

Spectra were extracted at 0.3" intervals (based on the telescope resolution) but since the typical seeing was worse than this, the effective extraction intervals are closer to 0.5". These intervals were increased if the S/N was sufficiently low (S/N $<$ 10). Each subsequent extraction sampled a new set of pixels out to the edge where a proper S/N of the emission line was no longer achievable. Each extraction was fit with EMCEE in a similar manner as described in Section 4.3.1.1. The peaks of each emission profile was compared to the zero-point to obtain line of sight velocities. We convert these velocities to rotational velocities using

$$v_{\mathrm{rot}} = \frac{v_{\mathrm{LoS}}}{\sin^{-1}(\theta_{\mathrm{inc}})} \tag{6.1}$$

where θ_{inc} is the inclination angle of the disk to the line of sight. For an infinitely thin disk, θ_{inc} can be calculated using the ratio of the semi-minor axis b and semi-major axis a through the equation $\theta_{\mathrm{inc}} = \cos^{-1}(b/a)$. To more accurately estimate the inclination angle, a thickness parameter $q = c/a$ can be introduced, where a is the radius of a circular disc and c is its thickness. When projected on a plane, the resulting shape is elliptical and $\theta_{\rm inc}$ can be described as

$$\theta_{\rm inc} = \sqrt{\cos^{-1}\left(\frac{(b/a)^2 - q^2}{1 - q^2}\right)} \tag{6.2}$$

We assume a value of $q = 0.1$ (Giovanelli et al., 1994) for all of our targets. To calculate the ellipticity $\epsilon = (1 - (b/a))$, we use the ISOPHOTE routine of the PHOTUTILS package (Bradley et al., 2020).

Seven galaxies show spatially extended emission for which we could measure the rotation curves as shown in Figure 4.6. We also do see some extended gas emission in J1036+0221 and J0122+0100(w), but do not include them in this analysis since they are likely involved in a merger event. The remaining four targets do not show spatially extended emission lines, most likely due to the high levels of extinction that they show.

6.8 J120443.76+050543.87

We include J1204+0505 here because it was observed in a parallel campaign and shares many similar characteristic with the bulgeless sample presented here. It is located at a redshift of 0.1097 and has a stellar mass of 10.1 $M_\odot$ (Chang et al., 2015). Surface brightness decompositions from Simard et al. (2011) show a B/T = 0.01, and supplementary fits only using an exponential disk result in a Sérsic index of 0.71. As such, it is unlikely that there is a significant bulge component. Although the BPT optical line ratios are not suggestive of AGN activity, J1204+0505 does fall within the scatter of our sample in the [S III]/Hα vs. [S II]/Hα diagram. It also meets the MIR color cut of S14 ($W1 - W2 = 0.84$).

J1204+0505 is a unique case since it is the only galaxy where we detect [Al IX] 2.044 μm emission and no other CL. Fitting the line with a single Gaussian, we detect it at a 3σ level (see Figure 6.16). To determine whether noise could have recreated this line profile, we use the F-test in a regression analysis model. Put simply, we sample a small region around the emission line and compare the residuals of when the line is fit and when it is not. We will call this value $F_{statistic}$ (or F_{stat}). Since this value is based on residual error, we need to treat it as a random variable with some probability. As such, we can use this to construct a probability density function (PDF), from which we can obtain a confidence level that the emission line is real, and not from random noise.

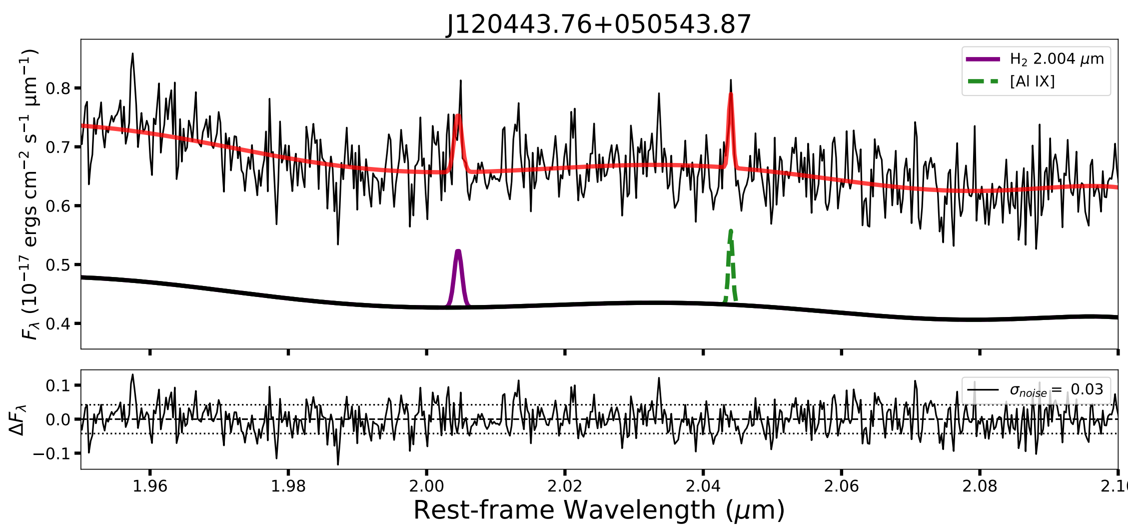

Figure 6.16: Zoom-in plot of [Al IX] 2.044 μm emission in J1204. The best-fit line from EMCEE is plotted in red. The fit to H_2 2.004 μm is also shown. The bottom panel shows the residuals of the fit with the 1σ error level shown as horizontal dotted lines.

We begin by using the following equation to calculate F_{stat}:

$$F_{stat} = \left(\frac{\frac{RSS_1 - RSS_2}{k_2 - k_1}}{\frac{RSS_2}{n - k_2}} \right) \quad (6.3)$$

where RSS_1 is the residual sum of squares of just a continuum fit (one degree of freedom), RSS_2 is the residual sum of squares of a continuum plus Gaussian fit (four degrees of freedom), and k is the degrees of freedom for each fit. Here, n is the sampling size, which in this case, is the number of wavelength channels in the selected region. From here, $(k_2 - k_1)$ and $(n - k_2)$ can be used to calculate the PDF for F_{stat}. We obtain a probability value of 0.97, that is, we detect the line at a 97% confidence. While this result is suggestive that the emission line is real, deeper follow-up observations will be needed to confirm this.